Analysis of Cosmic Muons Measured in CMS Drift Chambers

by
Raphael Mameghani

Diploma Thesis in Physics

presented to the
Faculty for Mathematics, Computer Science and Natural Sciences
of the RWTH Aachen University, Germany

in August 2004

performed in the

III. Phys. Inst. A

First evaluator: Prof. Dr. T. Hebbeker
Second evaluator: Prof. Dr. A. Böhm

Contents

Chapter 1

Introduction

"Why do you study physics?" Which student of that subject does not know this question asked by a friend or acquaintance not being involved in scientific research? A typical answer starts with the native curiosity of men and ends with the *Theory of Everything*, which unfortunatly still has to be developed even though there already are auspicious approaches. Usually the next question from that person is "And what is that all good for?" Typical replies from the scientist to-be are shrugged shoulders and a lack of understanding for such a question. But let us start from scratch:

Ever since the dawn of civilisation people recognised certain rules and patterns within their environment, such as night and day or the change of the seasons, and started to think of mystic explanations for these observations. Later in the ancient world first theories arose about the composition of matter: Demokrit's idea of atoms and Aristoteles' thesis of four elements. Both suggestions had in common that they tried to reduce a broad spectrum of matter properties to a compact set of constituents. But rightly, these persons are regarded as philosophers and not as physicists simply because they did not make predictions that could be compared to reality.

Physics from a modern point of view started when theories began to quantify expectations and were tested through experiments for their validity. With the publication of Newton's theory of motion and gravitation, his *Principia Mathematica*, physics entered a new age in which nature decided about success or failure of an explanation. As history shows, many long time accepted theories later were proven to be inaccurate, as experiments became able to test their predictions on new scales, which resulted in modifications of the models used or sometimes even in completely new ideas. The presumably greatest leaps that followed that way were Maxwell's theory about electromagnetic phenomena, Einstein's theories of relativity and quantum theory, developed by a number of now legendary scientists. The common aim of all these ideas is the reduction of the complex impression of the world to as few basic elements as possible, perhaps one day to a single fundamental principle. But as that aim could not be reached until now it is appropriate to divide the wide world of physics into some major fields, each with a different emphasis, of which one is particle physics.

Ratios of chemical reactions gave the first hints that matter consists of tiny lumps. Later on it was discovered by Thomson that these atoms are not elementary and scattering experiments with electrons by Lenard and with alpha particles by Geiger, Marsden and Rutherford turned out that atoms are composed of electrons carrying a unit of negative charge which surround a positively charged nucleus.

A new era with particle accelerators, allowing studies such as the structure of atomic nuclei, revealed that protons and neutrons build up the atomic core. Furthermore, physicists detected a large quantity of new, exotic particles being produced at high energies, first by cosmic rays and later also in accelerator experiments. But it became clear that this initial confusion is explainable by the existence of a few kinds of quarks being combined following certain rules. The quarks are regarded as elementary until today.

The present state of particle physics is desribed by the so called *Standard Model* containing not only these particles but also the forces that let them interact. This theory already made a lot of predictions which could be confirmed by experiments. But one of the main hypotheses is still left to be examined: the existence of the predicted *Higgs particle* could only be excluded for masses smaller than 114 GeV/c^2. To answer the question if it does exist after all, and to look for the presence of phenomena beyond the Standard Model, new, unevitably huge setups are required. Right now a new particle accelerator called *Large Hadron Collider*, abbreviated as LHC, and its two major detectors *Compact Muon Solenoid* (CMS) and *A Toroidal LHC Apparatus* (ATLAS) are under construction at the research centre CERN near Geneva.

One part of the first mentioned CMS detector is a complex system for the detection of particles called *muons*. This installation has been designed to be able to measure muons being produced at the collision of accelerated particles and to recognise the signature from the decay of possibly produced Higgs particles into four muons. The contribution of the III. Phys. Inst. of RWTH Aachen University mainly consists of the development, production and subsequent testing of drift chambers as a part of the muon system.

This diploma thesis concerns the analysis of data taken from drift chambers in a test setup with cosmic muons with a first emphasis on the quality control of the production and a second on the properties of just these cosmic particles as far as measurable. A major part of this work was the development of a software that transforms the recorded data into particle track descriptions from which the quality of a muon chamber can be deduced. As a side effect in succession it was tried to confirm already known characteristics of cosmic muons.

Now my trial to answer the question from above, what all this is good for, apart from satisfying the curiosity to see how the world can be described: I don't know. Maybe the technology and the knowledge gained by the challenge of finding the Higgs particle will turn out to be useful in some way we do not think of now, as it has already happened with earlier experiments. But I am not a prophet...

Chapter 2

The Standard Model of Particle Physics

The following sections are an attempt to summarise the present state of knowledge in particle physics. Of course this description is strongly shortened, not intending to cover all issues in such a detail that even a reader unexperienced in this field is guaranteed to understand every aspect. For more detailed introductions see [1], [2] or, with an emphasis on gauge theories, take a look at [3]. A brief compendium is also contained in [4].

2.1 Fermions

2.1.1 Quarks

For some time the broad spectrum of particles discovered within cosmic rays and with the help of experiments using particle accelerators had been a mystery. Physicists spoke of a *particle zoo* when they first thought those were all elementary components [5]. But Gell-Mann and Zweig explained this diversity with a common substructure of *quarks* and anti-quarks, and Greenberg added a kind of charge called *colour* to that concept to include Pauli's exclusion principle again, as quarks should be spin 1/2 particles, i.e. *fermions.*

There are two kinds of *hadrons*, thus particles made of quarks: *baryons*, consisting of three quarks with colours adding up to "white", and *mesons*, being a couple of quark and anti-quark. The variety of hadrons follows now due to the assumption of several quark *flavours* whose different combinations yield the observed particle spectrum.

Quarks

Family	Flavour	Spin	Charge [e]	Mass [MeV/c^2]
1	**u**p	1/2	+ 2/3	1.5 – 4.5
	down	1/2	– 1/3	5 – 8.5
2	**c**harm	1/2	+ 2/3	1000 – 1400
	strange	1/2	– 1/3	80 – 155
3	**t**op	1/2	+ 2/3	169200 – 179400
	bottom	1/2	– 1/3	4000 – 4500

Leptons

Family	Lepton	Spin	Charge [e]	Mass [MeV/c^2]
1	e	1/2	– 1	0.511
	ν_e	1/2	0	$< 0.225 \cdot 10^{-3}$
2	μ	1/2	– 1	105.7
	ν_μ	1/2	0	< 0.19
3	τ	1/2	– 1	1777
	ν_τ	1/2	0	< 18.2

Table 2.1: The three generations or families of quarks build up hadrons. The three lepton families just differ in their masses.

2.1.2 Leptons

Matter not only consists of hadrons but also of fermions called *leptons*, which do not have a colour charge and therefore appear as free particles. The electron as the only stable member of this group with an electromagnetic charge naturally is the most prominent one. Its partner, the electron neutrino, could not be detected for quite a while as it does not carry charge but was assumed to take away spin and momentum during the beta decay. With the *muon* and later on with the *tauon* heavier instable ”copies”[1] of the electron were found which decay[2] into an electron and neutrinos. For a long time neutrinos have been regarded as massless but recent experiments disproved this supposition.

2.2 Bosons

In modern physics four fundamental interactions are known. *Gravitation* as the weakest one is not part of the Standard Model. Nevertheless, it is the most apparent one since, as far as we know, there do not exist particles whose gravitational force is repulsive which would lead to a situation with these forces annihilating over larger distances. According to

---

[1] They really only differ in mass and therefore their gravitational interaction.

[2] The lifespan of a muon is still long enough to allow a cosmic one to penetrate the atmosphere of the earth, as shown later.

Einstein's theory of general relativity gravity is understood as the curvature of spacetime by the presence of mass. Since the corresponding potential is proportional to $1/r$, its range is infinite.

Electromagnetic interactions are magnitudes stronger than gravitational forces even though being irrelevant on a cosmic scale, as in macroscopic objects positive and negative charges usually exist in the same number so that their contributions cancel out. The electromagnetic force is the origin of molecular bonds and hence the reason for many macroscopic effects. Its potential is proportional to $1/r$, so reaching infinity, too.

Strong interaction prevents the protons and neutrons within a nucleus from falling apart and so it is responsible for their cohesion in spite of repulsive electromagnetic forces. Particles feeling this force are the quarks from the previous section as they carry colour charges. The strong force has a short range only. Thus larger nuclei decay since the electric repulsion gains in importance with larger radii of the atomic core.

Weak forces cause the radioactive beta decay. In spite of that name gravitational interactions are still negligibly small. A closer look at the weak force will follow later on.

The different ranges of the four interactions can be understood using the concept of quantum field theories, which describes forces by the exchange of excited field quanta that carry energy and momentum from one particle to another.[3] These discrete portions are identified with elementary particles. As a direct consequence of Heisenberg's uncertainty principle massive field quanta merely exist for very short time intervals Δt and hence only cover a limited distance s during their lifespan. As $\Delta E \cdot \Delta t \geq \hbar$, $\Delta E = mc^2$ and $\Delta t = s/c$, the maximum range of an exchanged particle is inversely proportional to its mass. So the unlimited reach of the electromagnetic force is due to the *photons* being massless. The same should apply for the *graviton*, the still hypothetical particle transmitting the gravitation. The strong interaction is carried by massless *gluons*. In this case the observation of a limited range in spite of massless exchange particles bases on the gluons as carriers of colour charges themselves. Hence they interact with each other via gluon exchange. The remaining weak force is transmitted by massive W and *Z bosons*.

All these exchanged *virtual*[4] particles are called *bosons* since they all have an integer spin of 1 with the graviton excluded which carries a spin of 2. So bosons are particles which do not obey Pauli's exclusion principle. Particle interactions are usually visualised by vertices in graphs plotting space versus time which are called Feynman diagrams, see figure 2.1 which illustrates the emission and absorption of bosons by fermions.

---

[3] A result of relativity as information can not be transmitted faster than light.

[4] Named that way as these field quanta do not appear directly

	Gravitation	Electromagnetism	Strong force	Weak force
Range	∞	∞	10^{-13}–10^{-14} cm	$\ll 10^{-14}$ cm
Example	astronomic attraction	forces between charges	cohesion of nucleons	beta decay of nuclei
Strength in natural units	$5.9 \cdot 10^{-39}$	$\frac{1}{137}$	~ 1	$1.02 \cdot 10^{-5}$
Affected particles	all	charged particles	quarks	quarks and leptons
Exchanged particles	gravitons	photons	gluons	vector bosons

Table 2.2: Four elementary forces describe all known particle interactions.

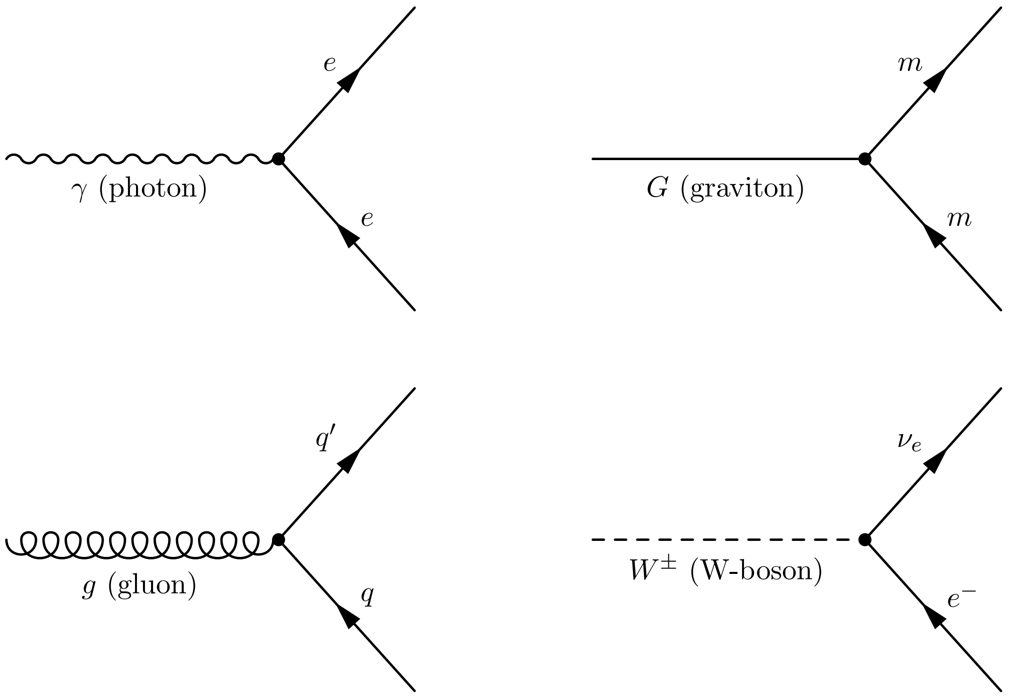

Figure 2.1: Feynman diagrams of elementary fermion boson vertices.

2.3 Gauge Theories

In this section gauge theories are introduced briefly. This approach obtains the fields whose exchanged particles transmit the elementary forces out of symmetries. Aspects like renormalisation, needed to relate calculated to measurable quantities, are not covered, but it has been proven that gauge theories can always be renormalised as long as the associated gauge bosons are massless.

2.3.1 The Gauge Principle

Most textbooks, [1] and [3] for instance, choose classical electrodynamics as the first example for the gauge principle. The basis are the Maxwell equations

$$\partial^\mu F_{\mu\nu} = 0 \qquad \text{and} \qquad \varepsilon^{\mu\nu\kappa\omega}\partial_\nu F_{\kappa\omega} = \frac{2}{\varepsilon_0 c} j^\mu \tag{2.1}$$

with the 4-current j and the electric and magnetic fields giving the components of the field strength tensor

$$F_{\mu\nu} = \partial_\mu \Phi_\nu - \partial_\nu \Phi_\mu \qquad \text{with} \qquad \Phi = (\phi, \vec{A}) \tag{2.2}$$

The electric field E and the magnetic field B can be deduced from the scalar potential ϕ and the vector potential A with the formulae

$$\vec{E} = -\nabla\phi - \partial_t \vec{A} \qquad \text{and} \qquad \vec{B} = \nabla \times \vec{A} \tag{2.3}$$

With a scalar function $\rho(t, \vec{x})$ and the the potentials transformed like

$$\phi'(t, \vec{x}) = \phi(t, \vec{x}) - \partial_t \rho(t, x) \tag{2.4}$$

$$\vec{A}'(t, \vec{x}) = \vec{A}(t, \vec{x}) + \nabla\rho(t, x) \tag{2.5}$$

all observable quantities remain unchanged [6]. Choosing a certain function $\rho(t, \vec{x})$ is called *gauging.*

In gauge theories the gauge freedom of certain variables is declared as the fundamental principle. This way the existence of the electromagnetic field and consequently its field quanta, the photons, is the result of the just described gauge freedom. The inner structure of the used transformation is always given by a symmetry group which is a U(1) symmetry for the electromagnetic field.

2.3.2 Global Symmetries

In general there are discrete symmetries such as reflection and continuous ones like translation but only the last case is considered here. In quantum mechanics a state is described by a wave function $\psi(x,t)$ solving the *Schroedinger equation*, but only its absolute square can be observed as a probability distribution. Apparently not only the amplitude $\psi(x,t)$ is a solution but also

$$\psi'(x,t) = e^{-i\lambda}\psi(x,t) \tag{2.6}$$

Or in other words: a global phase λ, independent of time and space, does not affect the observation. Of course this also applies for the relativistic *Dirac equation* for a spin 1/2 particle in the electromagnetic field A:

$$\left(i\gamma^\mu\left(\partial_\mu - i\frac{e}{\hbar c}A_\mu\right) - \frac{mc}{\hbar}\right)\psi_e(x,t) = 0 \tag{2.7}$$

$$\text{with} \qquad \gamma^\mu = (\beta, \beta\alpha^i), \quad i = 1,2,3$$

Special forms of α_i and β read

$$\alpha_i = \begin{pmatrix} 0 & \sigma_i \\ \sigma_i & 0 \end{pmatrix} \qquad \text{and} \qquad \beta = \begin{pmatrix} I & 0 \\ 0 & -I \end{pmatrix} \tag{2.8}$$

with the Pauli matrices σ_i and I being the 2×2 identity matrix. Again if $\psi_e(x,t)$ is a solution of equation 2.7 another one is given by the transformation

$$\psi'_e(x,t) = e^{+i\frac{e}{\hbar c}\lambda}\psi_e(x,t) \tag{2.9}$$

Frequently the Lagrange density $\mathcal{L}$ is used when symmetries are discussed. For example a scalar field $\phi(x)$ is described by

$$\mathcal{L} = \frac{1}{2}(\partial_\mu\phi)(\partial^\mu\phi) - \frac{1}{2}\frac{m^2c^2}{\hbar^2}\phi^2 = \frac{1}{2}(\partial_\mu\phi)(\partial^\mu\phi) - V(\phi) \tag{2.10}$$

It is connected to the Hamilton density $\mathcal{H}$ according to

$$\mathcal{H} = \pi\dot{\phi} - \mathcal{L} = \frac{1}{2}[(\partial_0\phi)^2 + (\nabla\phi)^2] + V(\phi) \tag{2.11}$$

$$\text{with} \qquad \dot{\phi} = \partial_0\phi \qquad \text{and} \qquad \pi = \frac{\partial\mathcal{L}}{\partial\dot{\phi}}$$

An advantage of the Lagrange density is that symmetries can be found easily with the *Noether theorem*

$$\partial_\mu\left(\frac{\partial\mathcal{L}}{\partial(\partial_\mu\phi)}\delta\phi\right) = 0 \tag{2.12}$$

saying that in case a field $\phi(x)$ is invariant under certain symmetry transformations a preserved 4-current exists. For example translation invariance leads to the conservation of momentum.

2.3.3 Local Symmetries

Now it is assumed that the phase λ is not a constant any more but depends on its position x in spacetime. This is a sensible approach because a certain point does not "know" the phase information of another one and information must not be exchanged faster than light [7]. In compliance with Einstein's principle of relativity a phase should be arbitrary in every reference system at any time. One can see that *local gauge invariance* of the Dirac equation under a transformation

$$\psi'_e(x) = e^{i\frac{e}{\hbar c}\lambda(x)}\psi_e(x) \tag{2.13}$$

can only occur if it is possible to compensate this local phase transformation of the wave function with a simultaneous transformation of the electromagnetic field A according to

$$A'_\mu = A_\mu + \partial_\mu \lambda(x) \tag{2.14}$$

In case there was no electromagnetic field one would get

$$\left(i\gamma^\mu \partial_\mu - \frac{mc}{\hbar}\right)\psi'_e(x) = \frac{e}{\hbar c}\Big(\partial_\mu \lambda(x)\Big)\gamma^\mu \psi'_e(x) \neq 0 \tag{2.15}$$

To keep the form of the Dirac equation it is common to introduce the covariant derivative

$$D_\mu = \partial_\mu - i\frac{e}{\hbar c}A_\mu \tag{2.16}$$

so that it is possible to write

$$\left(i\gamma^\mu D_\mu - \frac{mc}{\hbar}\right)\psi_e(x) = 0 \tag{2.17}$$

with D_k replacing the partial derivation of the free Dirac equation. Thus demanding local phase invariance yields the existence of the electromagnetic field. With the *gauge transformations* (2.13) and (2.14) electrodynamics can be described as the result of the invariance of the Lagrange density $\mathcal{L}$ under phase transformations. The associated constant, according to Noether's theorem (equation 2.12), is the electric charge e. The quantum of the gauge field, the *gauge boson*, is the photon as the particle exchanged at electromagnetic interactions. It is possible to show that all gauge fields must have massless field quanta.

2.3.4 Strong and Weak Interaction

The example of electromagnetic interaction has demonstrated that the existence of a symmetry directly leads to its gauge field quanta. To speak in terms of group theory: U(1) describes the underlying symmetry in electrodynamics.

Similar approaches give rise to the other gauge bosons from suitable gauge transformations if non Abelian groups are considered. The gauge bosons of the weak interaction, $W^\pm$ and W^3, are obtained from an SU(2) symmetry and the Pauli matrices as generators with the gauging

$$\vec{W}'_\mu = \vec{W}_\mu + \partial_\mu \vec{\lambda}(x) - \frac{2e}{\hbar c}\Big(\vec{\lambda}(x) \times \vec{W}_\mu\Big) \tag{2.18}$$

as three new vector fields have to be introduced. The W^3 boson has never been found experimentally so that the weak SU(2) gauge group has to be extended by the U(1) group of the weak hyper charge and its gauge field B. Observable are the fields Z^0 and A which are linear combinations of W^3 and B rotated by the Weinberg angle θ_W.

$$\begin{aligned} A^\mu &= B^\mu \cos\theta_W + W^{3\mu}\sin\theta_W && (2.19) \\ Z^{0\mu} &= -B^\mu \sin\theta_W + W^{3\mu}\cos\theta_W && (2.20) \end{aligned}$$

The quantity A is the already discussed electromagnetic field so that one can speak of a *unified* electroweak theory with an SU(2) × U(1) symmetry inherently containing the electromagnetic U(1) symmetry group. The fields A and Z^0 couple, with different strengths, to left and right handed fermions in contrast to the $W^\pm$ bosons which only couple to the left handed ones yielding parity violation.

An SU(3) symmetry generated by the Gell-Mann matrices and the gauging[5]

$$\vec{G}'_\mu = \vec{G}_\mu + \partial_\mu \vec{\phi}(x) - \frac{2e}{\hbar c}\left(\vec{\phi}(x) \times \vec{G}_\mu\right) \qquad (2.21)$$

results in eight gluons as gauge bosons. This is the strong interaction which is not discussed at this point.

So in general the Standard Model is an SU(3) × SU(2) × U(1) symmetry applied to the Dirac equation. Every generator of this global group delivers a gauge boson. So altogether there are the photon γ, three weak gauge bosons $W^\pm$ and Z^0 plus eight gluons of the strong interaction. Gravitation could not be described using a gauge field until today and consequently gravity is not part of the Standard Model.

2.4 Spontaneous Symmetry Breaking and the Higgs Mechanism

As mentioned before the idea of gauge invariance leads to massless bosons which obviously contradicts reality since $W^\pm$ and Z^0 masses of about 80 and 91 GeV/c^2 respectively have been measured. Another point is that the masses of the known elementary particles are merely parameters without a mechanism behind. A possible solution has been described by P. Higgs. He has postulated a background field, filling the entire space, that interacts with all massive particles yielding "effective" masses. Such a field should have a ground state of lower symmetry than the Lagrange density, a phenomenon called *spontaneous symmetry breaking*. This explanation requires degenerated ground states as perhaps already familiar from ferromagnetism for temperature drops below the Curie value, where spins have to decide for a direction to arrange along.

Analogous to the electromagnetic field with photons as exchanged particles there should be quanta of the Higgs field, the Higgs bosons. Their discovery would validate the theory and complete the Standard Model.

---

[5] With the vector product defined as $(\vec{B}\times\vec{C})_i = \sum_{j,k=1}^{8} f_{ijk} B_j C_k$ and the f_{ijk} as the structure constants of the SU(3).

2.4.1 The Mass Term and the Higgs Potential

So where in the Lagrangian has to be the term responsible for the effective mass? Starting from the relativistic energy momentum relation

$$E^2 = \vec{p}^2 c^2 + m^2 c^4 \tag{2.22}$$

and using the usual quantum operators yields the Klein Gordon equation

$$(\partial_\mu \partial^\mu + \frac{m^2 c^2}{\hbar^2})\phi = 0 \tag{2.23}$$

which describes particles without a spin. The respective Lagrange density reads

$$\mathcal{L} = \frac{1}{2}\Big((\partial^\mu \phi)(\partial_\mu \phi) - \frac{m^2 c^2}{\hbar^2}\phi^2\Big) \tag{2.24}$$

This yields the motion of a free particle with a mass m described by a scalar field ϕ.

Within field theory the idea of spontaneous symmetry breaking is realised by the introduction of a scalar field in the Lagrange density. The simplest case yields

$$\mathcal{L} = \frac{1}{2}(\partial^\mu \phi)(\partial_\mu \phi) - V(\phi) \tag{2.25}$$

with the Higgs potential

$$V(\phi) = -\mu^2 |\phi|^2 + \lambda^2 |\phi|^4 \tag{2.26}$$

whereas ϕ is the complex scalar Higgs field

$$\phi(x) = \frac{1}{\sqrt{2}}\Big(\phi_1(x) + i\phi_2(x)\Big) \tag{2.27}$$

The Higgs potential has to contain the $|\phi|^4$ term because of its required self interaction and the demand for $V(\phi)$ being real. The parameters of the potential are μ and λ with $\lambda^2 > 0$, so that $V(\phi)$ is bounded from below. If $\mu^2 > 0$ there is no unique minimum of $V(\phi)$ but a whole circle of minima in the complex ϕ plane as illustrated in figure 2.2. That means that there is an infinite number of degenerated ground states $\phi_0(\delta)$ with

$$\phi_0(\delta) = \frac{1}{\sqrt{2}} e^{i\delta} \sqrt{\phi_1^2 + \phi_2^2} = \frac{1}{\sqrt{2}} \frac{\mu}{\lambda} e^{i\delta} \tag{2.28}$$

Here δ is an arbitrary parameter that determines a single position on the minima circle. The symmetry present in the Lagrangian is broken spontaneously.

Expansion of the scalar Higgs field around the ground state, with $\delta = 0$ fixed, gives the Lagrange density

$$\mathcal{L} = \frac{1}{2}\Big((\partial_\mu \eta)(\partial^\mu \eta) - 2\mu^2 \eta^2\Big) + \frac{1}{2}\Big((\partial_\mu \xi)(\partial^\mu \xi)\Big) + \ldots \tag{2.29}$$

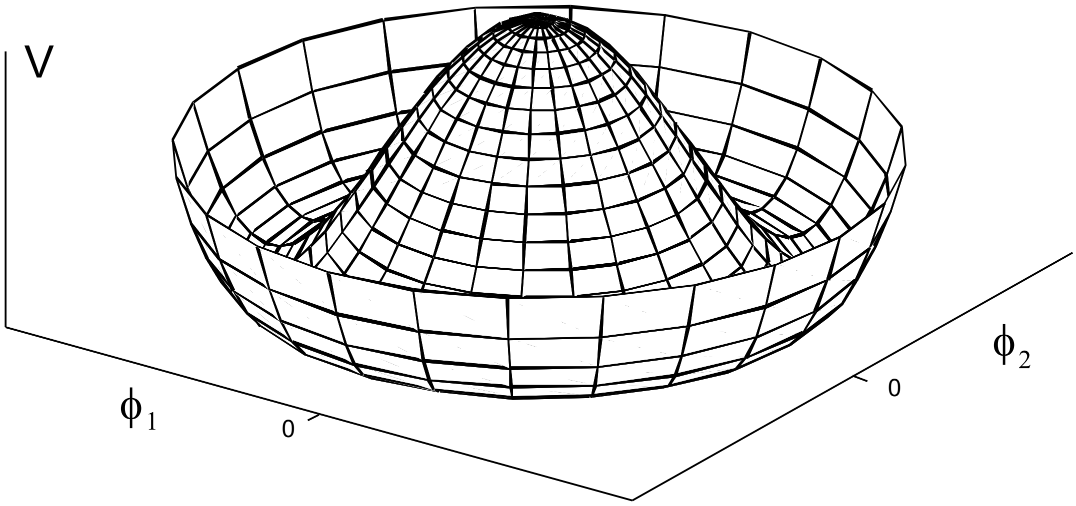

Figure 2.2: The Higgs potential describes the spontaneous symmetry breaking of the vacuum.

after the coordinate transformation $\phi_0(x) = \frac{1}{\sqrt{2}}\Big(\frac{\mu}{\lambda} + \eta(x) + i\xi(x)\Big)$.

Now a comparison with the Klein Gordon equation (2.23) yields a massive Higgs particle with $M_\eta = \sqrt{2}\mu\hbar/c$ and another one with $M_\xi = 0$ called Goldstone boson which has never been observed in any experiment. Demanding local instead of global symmetry breaking lets these massless degrees of freedom vanish, as they are needed for the gauge bosons. So unification of the concepts of both spontaneous symmetry breaking and local gauge invariance results in effective masses for the $W^\pm$ and Z bosons after the introduction of

$$\phi = \begin{pmatrix} \phi^+ \\ \phi^0 \end{pmatrix} \qquad \text{with} \qquad \begin{array}{rcl} \phi^+ & = & \frac{1}{\sqrt{2}}\big(\phi_1(x) + i\phi_2(x)\big) \\ \phi^0 & = & \frac{1}{\sqrt{2}}\big(\phi_3(x) + i\phi_4(x)\big) \end{array} \tag{2.30}$$

The accordant Lagrangian reads

$$\mathcal{L} = \frac{1}{2}\Big((\partial_\mu\eta)(\partial^\mu\eta) - 2\mu^2\eta^2\Big) + \frac{1}{2}\cdot\frac{g^2a^2}{4}\Big(|W_j^+|^2 + |W_j^-|^2\Big) + \frac{1}{2}\cdot\frac{g^2a^2}{4\cos^2\theta_W}|Z_j|^2 \tag{2.31}$$

using the abbreviation $a = \frac{\mu}{\lambda}$ and the herewith introduced coupling constant g. Obviously one receives $M_{W^\pm} = \frac{1}{2}ga\frac{\hbar}{c}$ and $M_Z = \frac{M_{W^\pm}}{\cos\theta_W}$. The mass of the Higgs boson $M_H = \sqrt{2}\mu\frac{\hbar}{c}$ is a free parameter of the model and can only be determined experimentally. But until today no attempt succeeded and so there is only a lower limit of 114 GeV/c^2 measured by the four LEP detectors [8].

It is possible to expand the Higgs mechanism and the Lagrange density to explain not only boson but also fermion masses if interactions with the Higgs field are introduced. In general the mass of a fermion is the bigger the larger the coupling. For example one gets the following additional term in the Lagrange density for the electron and its neutrino describing the Yukawa coupling:

$$\mathcal{L}_{el} = g_e(\bar{L}\phi e_R + \phi^\dagger \bar{e}_R L) \qquad \text{with} \qquad L = \begin{pmatrix} \nu_e \\ e^- \end{pmatrix}_L \tag{2.32}$$

From that approach it is possible to derive the dominating decay channels of the Higgs boson depending on its mass as shown in figure 2.3. For a Higgs mass of less than about 140 GeV/c^2 the decay into two bottom quarks is expected to dominate since these have the strongest coupling constant of the quarks within energetic reach. The high mass of the top quark lets the decay channel into a pair of them contribute from about 350 GeV/c^2. But well below the production of Ws and Zs is possible which deliver the main decay modes for Higgs masses above approximately 140 GeV/c^2 and 170 GeV/c^2 respectively.

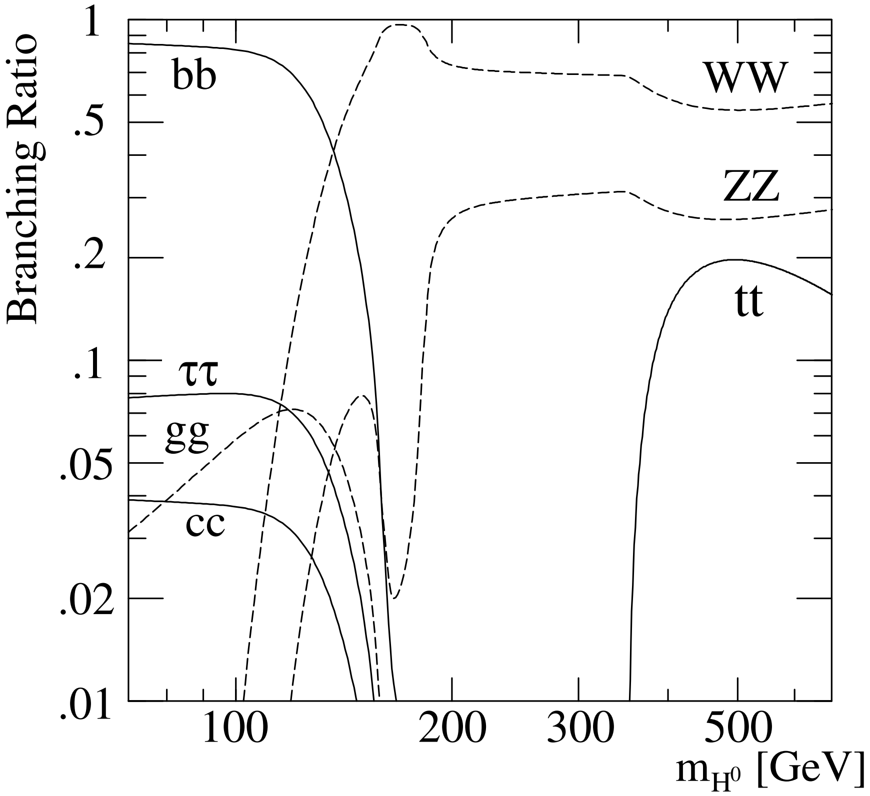

Figure 2.3: Branching ratios for the main decay modes of the Higgs boson [9].

2.4.2 A Clear Higgs Signature

Even though the decay of the Higgs boson H into two Z bosons is not the dominating channel, as observable in figure 2.3, it deserves special attention as further decay, see figure 2.4, may lead to a clear signature with four final leptons. Of particular interest is the signature with four final muons since these can be separated quite simply with massive absorbers from all other particles. Such a pattern gives optimal conditions for detection because of its best signal over background ratio and is hence called the *golden channel* [10]. That aspect influenced the design of the later described CMS detector which has an elaborate muon detection system therefore.

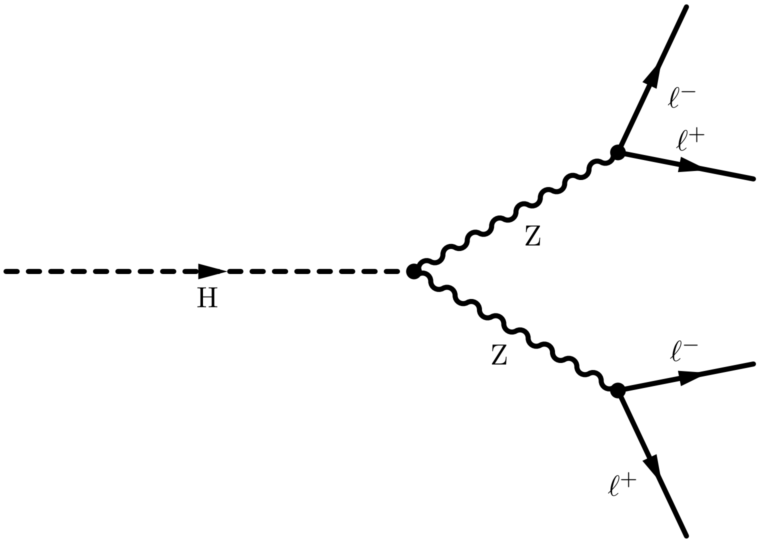

Figure 2.4: Feynman diagram of the Higgs boson decay via two Z bosons into four leptons.

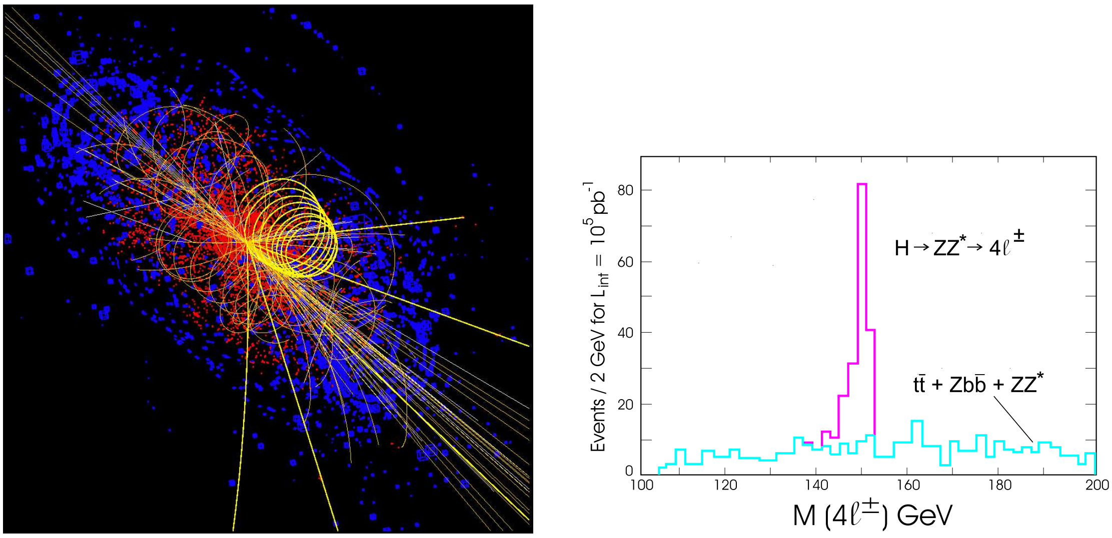

Figure 2.5: A simulated Higgs particle decays into four muons in the CMS detector [11]. A signal as shown on the right is expected for a decay into four leptons at a Higgs mass of 130 GeV/c^2 $< M_H <$ 170 GeV/c^2 and an integrated luminosity of 10^5 pb^{-5} [12].

Particle	Spin	Superpartner	Spin
Fermions		**Sfermions**	
quark	1/2	squark	0
lepton	1/2	slepton	0
neutrino	1/2	sneutrino	0
Bosons		**Bosinos**	
gauge boson	1	gaugino	1/2
photon	1	photino	1/2
gluon	1	gluino	1/2
higgs	0	higgsino	1/2

Table 2.3: The Standard Model particles and their postulated supersymmetric partners. By convention one adds the prefix "s" to fermion names to refer their superpartners and the suffix "on" is replaced by "ino" for the SUSY partners of the bosons.

2.4.3 Higgs Mass Corrections and Supersymmetry

Even though the Standard Model has been tested with outstanding precision in available energy ranges, theoretical arguments make a good point that an extrapolation to arbitrarily high energies must fail. A limit of validity is given by the Planck mass of $M_P = \sqrt{\hbar c/G} = 1.2 \cdot 10^{19}$ GeV/c^2 where a quantum theory of gravitation is required [4]. *Supersymmetry* (SUSY) may be an explanation for many still problematical issues. Of course the SU(3) × SU(2) × U(1) symmetry has to be contained anyway. For a first introduction see for instance [13].

Supersymmetry introduces a new partner $\tilde{f}$, $\tilde{b}$ for every Standard Model fermion f or boson b whose spin differs by 1/2. This means that each fermion gets a supersymmetric boson called *sfermion* on its side and each boson a supersymmetric fermion named *bosino*. Since such particles have not been discovered until today this new symmetry, if existent, must be broken in such a way that SUSY particles have masses out of direct[6] reach at the present.

Still a problem of the Standard Model is the mass divergence of the Higgs boson due to the mass corrections shown in figure 2.6. Supersymmetry would add new particles[7] that contribute their loops to the Higgs mass with opposite signs so that the sum does not diverge any more as illustrated by figure 2.7.

The Higgs mechanism itself would receive a slightly more complicated form since the single field quantum has to be replaced by five Higgs bosons as required by the MSSM[8] whose SUSY partners would be mixed. There are hints, see [4], that the masses of super-

---

[6] Experiments measuring $g - 2$ may show indirect hints at lower energies since SUSY particles would contribute virtually.

[7] Generally these partners are called *sparticles*.

[8] Minimal supersymmetric extension of the Standard Model.

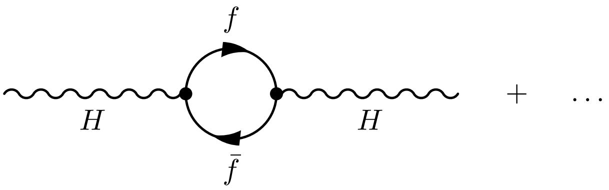

Figure 2.6: The Higgs mass correction by loops of Standard Model particles f diverges, as ΔM_H is proportional to the cutoff.

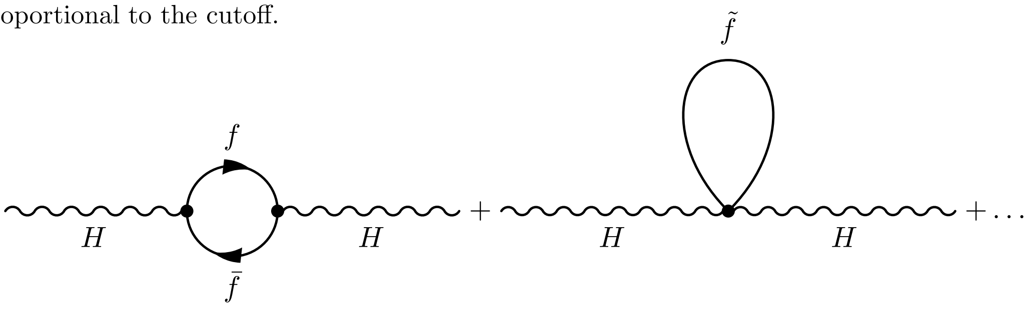

Figure 2.7: Supersymmetric partners $\tilde{f}$ would contribute to the Higgs mass corrections and, since fermions and bosons give different signs, the mass divergence could be compensated.

symmetric particles should be within energetic reach for the upcoming operation of the LHC yielding another interesting field for research and future physics at high energies.

Chapter 3

The LHC and the CMS Detector

Particle accelerators are today's tool for the production of heavy particles. The *Large Hadron Collider* (LHC) is a proton storage ring still under construction which will be able to reach collision energies large enough to decide about the Higgs hypothesis and other theories, as descibed in the previous chapter. At one of the LHC collision points the *Compact Muon Solenoid* (CMS) detector will be positioned to identify and measure the reaction products.

3.1 Particle Accelerators

Already from De Broglie's hypothesis $\lambda = h/p$ for the wave-particle duality of the electron it is noticeable that high energetic probe particles are needed for wavelengths short enough to allow for the examinaton of subatomic structures. For the production of new particles the use of two colliding particle beams gives the maximum energy available in the centre of mass system.

The construction of particle accelerators with energies outperforming existing ones is essential to discover new physics. Generally there are either linear or ring accelerator machines, the latter with the advantage of re-using the same accelerator elements for one particle bunch again and again at the price of power losses due to synchrotron radiation according to

$$P_S \propto \frac{E^4}{m^4 \rho^2} \tag{3.1}$$

for particles with mass m and ρ being the radius of curvature. This is a strong limitation for the use of ring accelerators. Ways to reduce this loss are either larger ring diameters or, even more effective due to the strong mass dependence, the use of heavier particles such as protons[1]. A summary of accelerator physics can be found in [14].

---

[1] Electrons are often preferred anyway as they are the only stable charged particles without a substruc-

Figure 3.1: An aereal view of the LEP tunnel which is re-used for the LHC accelerator [15].

3.2 The Large Hadron Collider

The Large Hadron Collider at CERN will be a so called storage ring for protons circulating both clockwise and counterclockwise in a common vacuum tube. Both proton beams have individual beam pipes which is a more elaborate concept than using a combination of protons and anti-protons in a single one. Nevertheless, this approach had been favoured to avoid the limitation of the luminosity $\mathcal{L}$, a size for the number of particle interactions at the collision points per time, as the rate of the anti-proton production would give too big constraints.

The design re-uses the existing 27 km long tunnel of the formerly installed LEP[2] accelerator. The high energies require helium cooled superconductive bending magnets of more than 8 T, each over a length of 14 m, to keep the protons inside their pipes. Figure 3.2 gives an impression of the complex dipole design.

Acceleration will take place in eight straight sections. In these zones both proton beams gain energy at areas where the beam pipe is replaced by cavities where electromagnetic radiation of high frequency powers the proton bunches. At four locations the beams are

---

ture which allows "clean" collisions. The price are large ring diameters.

[2] Large Electron Positron Collider

brought to collision. The kinetic energy of the protons, in the centre of mass system with $\sqrt{S}$ of up to 14 TeV, is used for the production of new particles. The reachable luminosity $\mathcal{L}$ amounts to $10^{34}\text{cm}^{-2}\text{s}^{-1}$, about two orders of magnitude larger than the Tevatron accelerator accomplishes at present [16]. There will be bunches of 7.5 cm to 13 cm length circulating with a time distance of 25 ns containing about 10^{11} protons each.

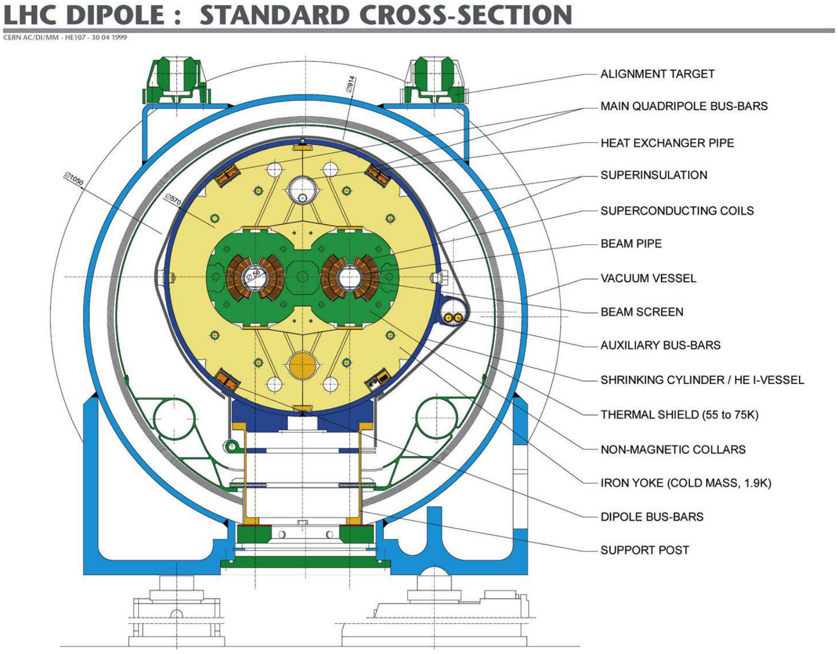

Figure 3.2: Cross section through the LHC tube with its two beam pipes and the cooling system for the superconductiong coils [15].

Due to the substructure of the protons and the high energies a huge number of particles is produced in every single collision demanding elaborated detectors around the beam crossings for event reconstructon. Essential, besides other aspects, are fine granularities of the detector components and fast responses. The detectors at the four interaction points are ATLAS and CMS, two complementary universal detectors, LHCb for precision measurements of CP violation im B physics and later ALICE for a close look on the quark gluon plasmas, when instead of protons lead nuclei will be filled in the accelerator ring.

3.3 The Compact Muon Solenoid Detector

The *Compact Muon Solenoid* detecor (CMS) has been conceived, like ATLAS, as a universal detector [17]. Its design is optimised for proton-proton collisions at high luminosities. Since the decision was to build a compact device the consequence was the need for a strong magnetic field. That is why the CMS detector got an about 14 m long superconducting solenoid of roughly 3 m diameter that generates a magnetic field of 4 T which is strong enough to assure a good momentum resolution for high energetic muons. Muon momenta

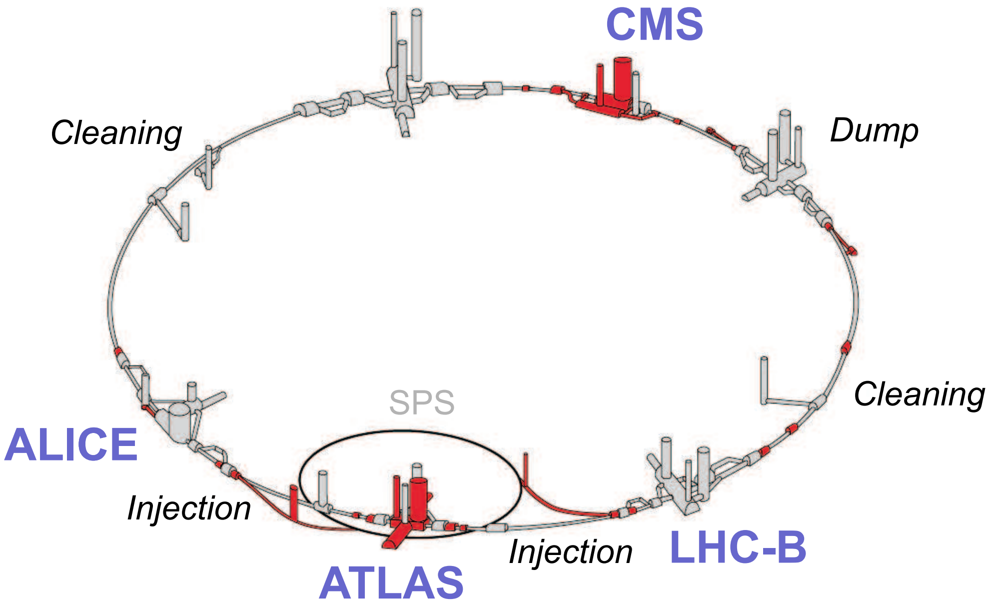

Figure 3.3: A schematic drawing of the LHC. The necessary new infrastructure for upgrading the LEP tunnel for LHC is marked in red colour [15].

are measurable from deflections in the flux return yoke, as long as the spatial resolution of the used detector elements is adequate.

The CMS detector has a cylinder symmetry, as visible in figure 3.4, with a typical onion layer arrangement of its subdetectors. Along the beam direction there are five movable wheel elements allowing access to the inner structures for maintenance reasons. From inside out the detector is arranged in the following way: the *inner tracker* with its silicon pixel and microstrip detector directly surrounding the collision zone is optimised in terms of radiation length, spatial resolution and occupancy. It is essential point to respect the very high radiation level near the beam pipe with its influence on aging and the following damage of the silicon components.

The next layers contain the *electromagnetic* and *hadronic calorimeters* (ECAL & HCAL). The former shall detect, thus the name, electromagnetic particles and measure their energies with massive $PbWO_4$ crystals and the latter is designed to determine directions and energies of incoming hadronic particles using scintillator layers embedded into copper absorbers. The calorimetric system with its energy measurements provides an important contribution for the event reconstruction. Especially involved photons are detected there. In any case it is needed for the collision enery accounting and hence it should cover, in ideal case, the collision area hermetically. That is why two very forward calorimeters, immediately surrounding the beam pipe outside the solenoid, are installed, too.

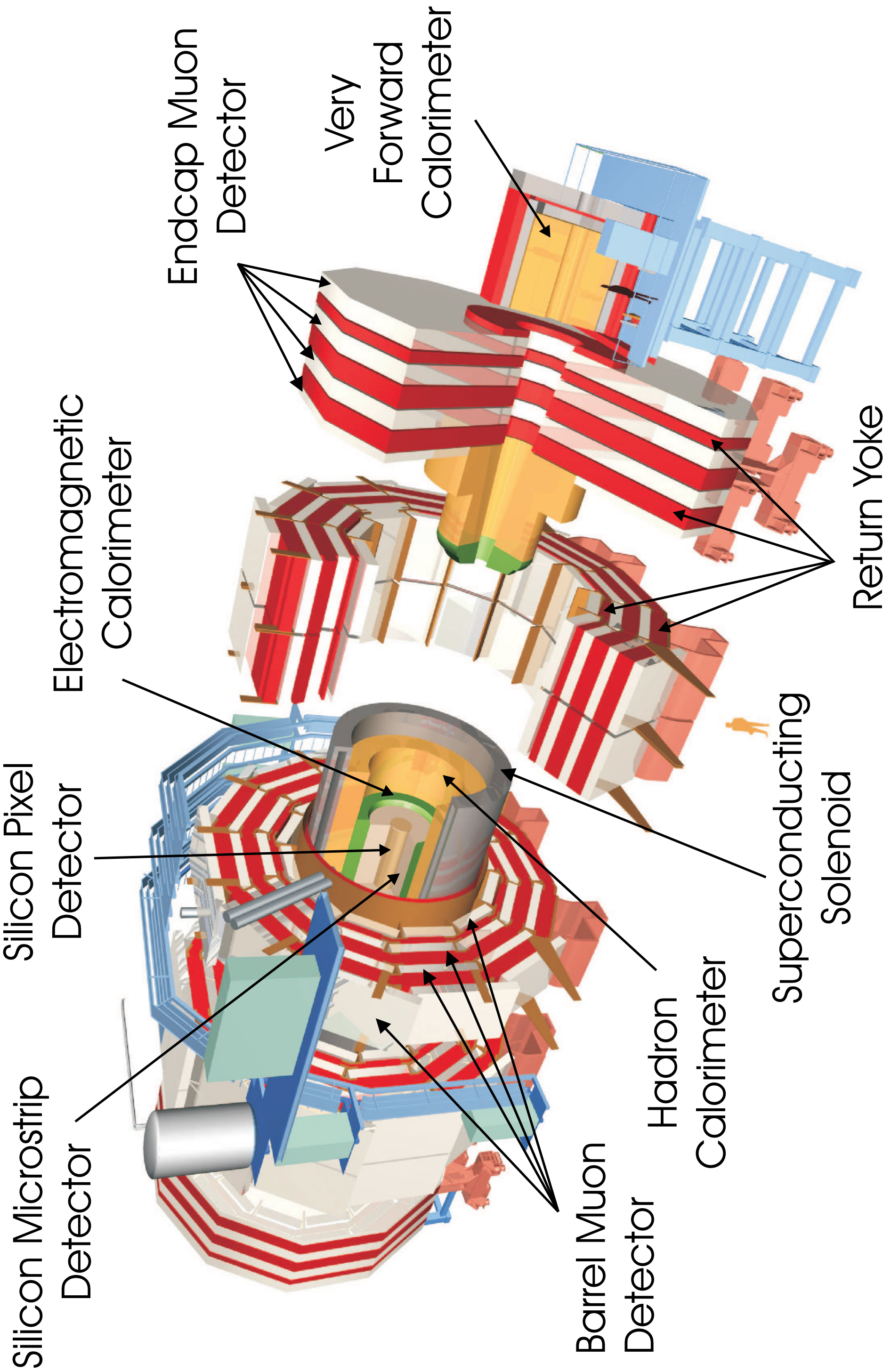

Figure 3.4: Exploded drawing of the CMS detector [12].

The outer region of the detector holds the *muon system* which is embedded into the iron return yokes of the solenoid. The muon system, details will follow in the subsequent section, recognises particle tracks and allows momentum calculation from the bending within the return yoke with its enclosed high magnetic field.

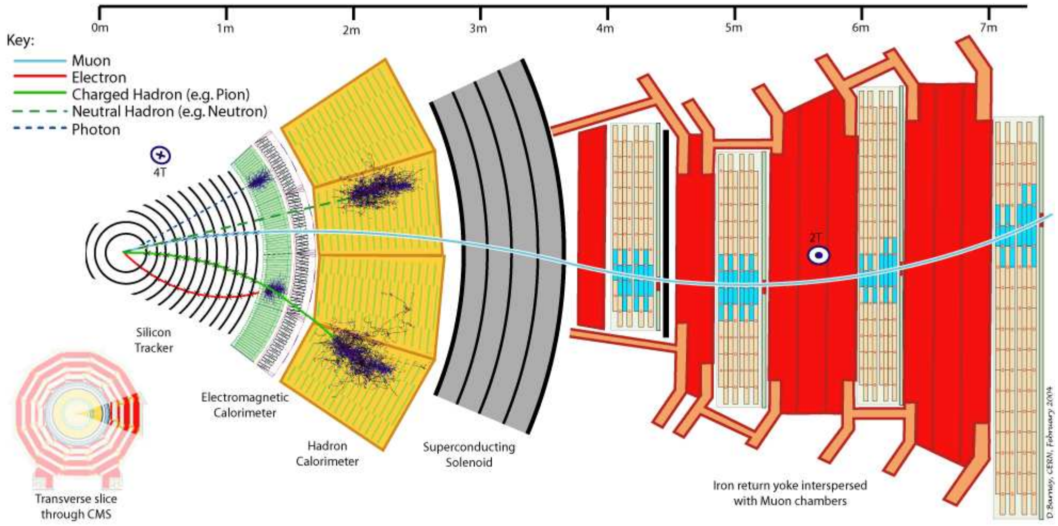

Figure 3.5: Transverse slice through CMS. The onion layer structure allows distinct signatures for different kinds of particles [12].

Figure 3.5 illustrates the particle separation of the CMS detector in principle: electrons give traces inside the inner tracker and are likely to be stopped within the ECAL. Photons are recognised by ECAL showers only. Corresponding patterns are valid for hadrons: the charged ones yield tracker and HCAL responses and the neutral long-lived ones are not seen before the HCAL. Muons are undisturbed when passing all these layers hence being the only charged particles traversing the detector completely. This is the reason why the Higgs decay into four muons is such a promising channel.

3.4 The Muon System

The CMS muon system exploits three technologies [18]: drift tubes in the *barrel* region, cathode strip chambers in the *endcap* region and resistive plate chambers in both the barrel and the endcap. The division into barrel and muon area has been made because of the different intensities of the local magnetic field. The field is of relatively low strength inside the detector elements of the barrel region because of the presence of the return yoke allowing a drift chamber tracking detector there. In the endcap cathode strip chambers are needed due to the high magnetic field penetration.

3.4.1 Drift Tube Chambers

The barrel region of the muon system is realised with *drift tube chambers* (DTs). This decision was based on the comparatively low expected rate and on the small enough strength of the local magnetic field. The basic elements in such chambers are drift cells of about 400 ns maximum drift time which operate in the following way.

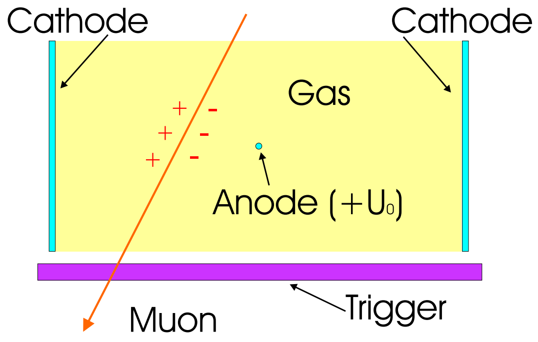

Figure 3.6: Drift tubes measure the time the electrons need to reach the anode wire. A more detailed illustration will follow in figure 5.1

A charged particle traversing gaseous detector material ionises the gas molecules, or, in case of a noble gas, the atoms, along its trace. Influenced by an electric field between cathode and anode the ionisation electrons drift with a typical velocity of some 10 μm/ns towards a thin anode wire. Close to that wire the electric field strength increases rapidly due to the $1/r$ dependece, thus accelerating the electrons so strongly that further gas molecules are ionised and an avalanche starts. This way the original charge is amplified by a factor of 10^4 to 10^6.

As long as the applied field is not so strong that the photons emitted during gas gain are not too numerous, a configuration used for Geiger counters (see [19]), the number of electrons collected by the anode wire is proportional to the number of charges produced by the primary ionisation. The CMS drift chambers do not measure signal heights but drift times alone. The drift time is the time elapsed since the moment of a particle transit, given by a trigger, and the signal measurement of the tube. With a known drift velocity the drift distance is obtained. An arrangement of several drift tubes enables particle track reconstructions afterwards.

The barrel muon chambers are placed in four stations yielding concentric cylinder jackets around the beam line, see figure 3.4. In total there are 250 drift cambers of different size but equivalent layout. This is the chamber type which is produced and tested at Aachen. The actual chamber geometry will be discussed in chapter 5.1.

3.4.2 Cathode Strip Chambers

Both CMS endcap regions have four muon stations of *cathode strip chambers* (CSCs). They operate reliably under the influence of magnetic fields at high background rates as expected for CMS. CSCs are multiwire proportional chambers in which one cathode plane is segmented into strips running perpendicularly across the wires. Penetrating particles ionise the chamber gas and within the applied electric field an avalanche amplification happens. A charge avalanche generated on one of the wires induces a well known charge distribution on the cathode plane. For CSCs in general it could be shown that via interpolation of the picked up charges at the strips a track reconstruction with 50 μm intrinsic precision is possible [20]. Required for CMS are 75 μm and 150 μm respective [18]. In the other direction the resolution is given by the wire distance of about 3 mm since expected particle tracks are almost parallel to the electric flux lines. But the grouping of the read out channels reduces the radial coordinate precision to a few centimeters.

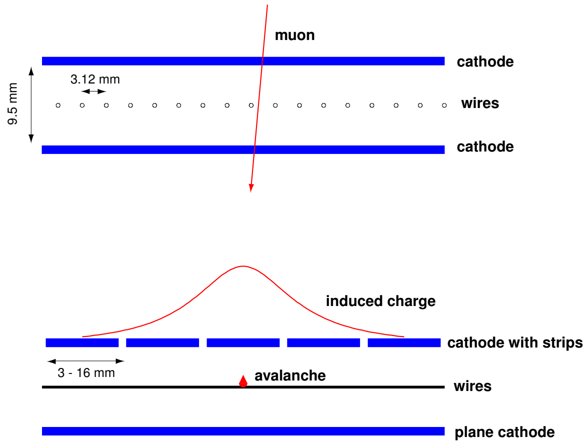

Figure 3.7: View across the wires (at the top) and across the cathode strips (at the bottom). Small spaces between the wires allow a fast chamber reaction whereas the track coordinate in wire direction can be measured via interpolation of the carge distribution [18].

Using six planes of such a kind in each chamber makes the endcap detectors adequately robust respective the high background because secondary particles are unlikely to traverse more than one layer.

All cathode strip chambers are of trapezoidal shape and are arranged to fit into the endcap disk structures around the beam line. These rings are separated by the iron disks of the magnetic flux return yoke (see figure 3.4). The disks overlap in such a way that there are no blind regions down to 10° inclination to the proton beam.

3.4.3 Resistive Plate Chambers

Resistive Plate Chambers (RPCs) are included in the muon systems, of both the barrel and the endcap, thanks to their small height and consequently fast responses, comparable to those of scintillators. That is why they are a good choice for space-time particle tracking as needed for the muon trigger.

The RPCs are chambers with parallel plates made of bakelite with a bulk resistivity of $10^{10} - 10^{11}$ Ω cm whose spacing is filled with gas. The outer surfaces of the resistive plates are coated with a thin graphite film as conductor forming high voltage and ground electrodes. The signal is read out on the basis of aluminium strips insulated from the graphite by a thin PET layer.

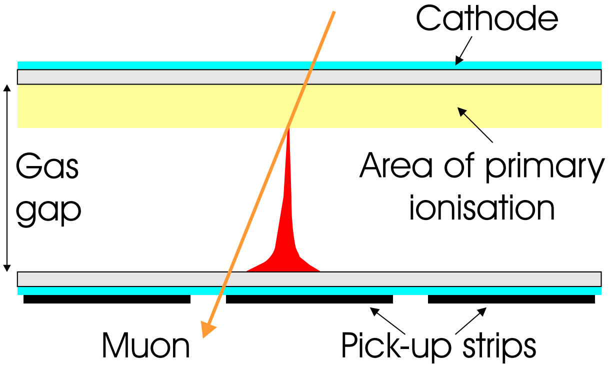

Figure 3.8: Operating mode of a resistive plate chamber in principle.

A traversing particle liberates electrons from the gas inside a RPC which drift towards the anode, starting an avalanche. Finally the bakelite plate is reached and penetrated slowly in the following until the electrons arrive at the graphite coating. Thus a charge is induced on the aluminium strip below and a signal can be read out within a few nanoseconds. The time resolution basically depends on the drift distance in the gaseous material while the choice of the resistive plate parameters has a major influence on the compatibility with the expected particle rates. The construction and operation parameters for CMS RPCs yield a precision of ≤ 3 ns [18].

Chapter 4

Cosmic Muons

Since the CMS drift tube chambers are tested for functionality with cosmic muons and certain studies on these particles are possible as a side effect during this procedure this chapter gives a brief outline on cosmic radiation.

4.1 Cosmic Radiation

Cosmic radiation is defined as the high energetic radiation from the universe that is bombarding the earth. The main component are ionised atomic nuclei with a rate around 1000 impacts $\mathrm{cm}^{-2}\mathrm{s}^{-1}$. The knowledge of cosmic radiation has its origin in V. Hess' balloon flights in 1912 and has been expanded within the decades since than by various experiments [21]. The measured energies of cosmic particles have been observed to range 15 orders of magnitude and since the fluxes differ enormously diverse experimental approaches are necessary and combined for the complete picture [4].

4.1.1 Sources of Cosmic Radiation

Because of the wide range of particle energies several different sources of cosmic radiation seem to exist. In general there are the possibilities of a universal origin or an origin confined to our galaxy. The mechanisms most likely are listed in the following.

Supernova Explosions

It is postulated that supernova explosions are the main source of cosmic radiaton. From observations it is known that on average the rate of such events is one in 30 years per galaxy.

Each time a total energy of 10^{44} J is set free which is enough to maintain the observed quasi-stationary flux even in case only 10 % of the supernova energies are transferred to cosmic rays [4].

Betatron and Fermi Mechanisms

In this case cosmic ray particles are considered to be accelerated by electromagnetic fields. In a single process an increase or decrease of energy can happen but in statistical models with a large number of interactions an overall energy gain is the result [4]. The two fundamental processes are

- *betatron acceleration* where particles gain energy in homogenous magnetic fields that increase with time and
- *Fermi mechanisms* in which the acceleration happens due to interactions with moving magnetic field inhomogeneities like shockwaves in magnetic plasmas [4].

Pulsars

Rotating neutron stars, which are remainders of supernovae from today's point of view, induce strong fields which accelerate nearby charged particles to high energies. Pulsars have an initial rotation energy of about 10^{46} J and so especially the young ones can provide the required power. Acceleration is possible either by the strong magnetic surface fields or by generated intense low frequency electromagnetic radiation [21].

Extragalactic Origin

It is sensible to assume that the milky way is not the only galaxy producing cosmic radiation. In particular *quasars* and *active galactic nuclei* (AGN) like *radio galaxies* are considered as powerful sources. In the standard theoretical model of AGN the energy is produced by matter falling onto a supermassive black hole in the centre of a galaxy. As the material falls into the black hole, the angular momentum produces an accretion disk. Friction causes the approaching matter to turn into plasma, and just this charged moving material produces a strong magnetic field which is responsible for extremely high energetic particles.

4.1.2 The Cosmic Ray Spectrum

The cosmic ray spectrum, see figure 4.1, contains the flux reaching the atmosphere as a function of the nucleus energy E. For values smaller than 10^{15} eV there is a decrease proportional to $E^{-2.7}$. From that point, which is called *knee*, until about 10^{19} eV, the *ankle*, the decrease goes according to E^{-3}.

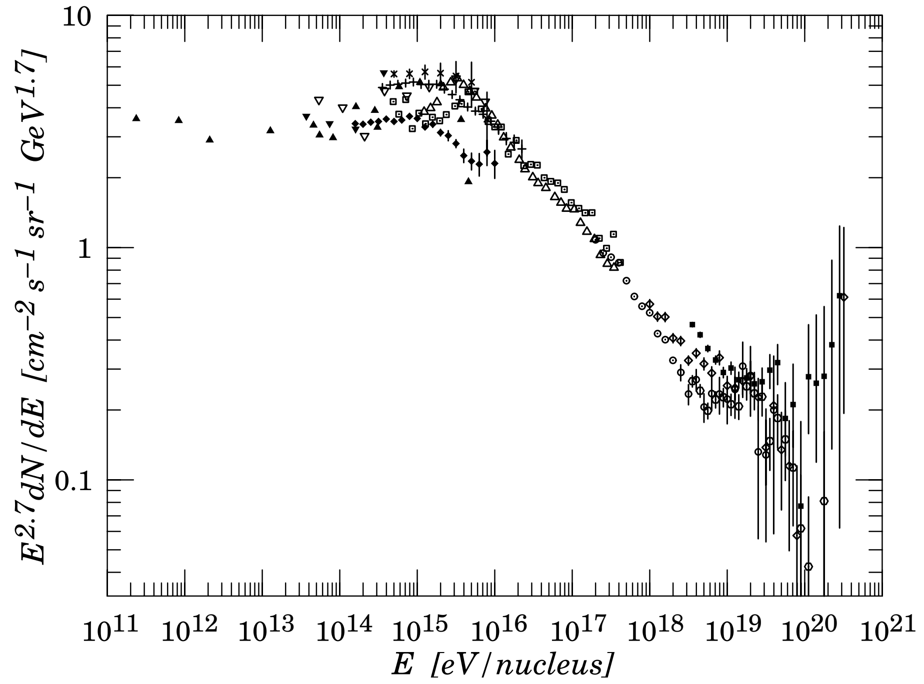

Figure 4.1: Overall energy spectrum of cosmic rays. Outstanding are the changes of the dependency at 10^{15} and 10^{19} eV [14].

If the cosmic ray spectrum below 10^{19} eV is from sources within our galaxy the observed knee is likely to occur since at this point some accelerator mechanisms reach the maximum energy they can provide. At the ankle it seems that the intensity of cosmic rays from outside our galaxy overtake the local sources. If this is really the case there should be a cutoff around $5 \cdot 10^{19}$ eV as a consequence of interactions with the cosmic microwave background [14]. So the few events with assigned energies above 10^{20} eV are of special interest and present experiments are designed to examine this area thoroughly in spite of the very low rate in this region.

4.2 The Primary Spectrum

The classical cosmic radiation consists of 98% atomic nuclei and 2% electrons. The nuclei again are mainly (87%) protons with some (12%) α particles and the remainder (1%) are heavy elements. The composition of the heavy nuclei agrees to a large extent with solar values, see figure 4.2, which is a strong hint for their stellar production. The obvious differences can be explained with spallation processes [4]. Above some TeV the constitution of the primary cosmic radiation is unknown and merely the energy spectrum (figure 4.1) could be observed.

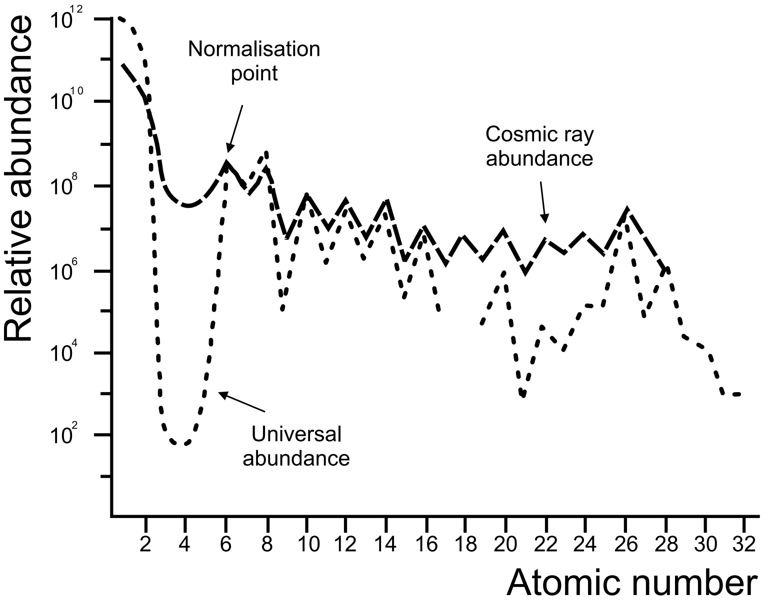

Figure 4.2: Comparison of the chemical composition of cosmic rays with the universal composition. Both graphs are normalised to carbon [22].

Cosmic electrons deliver synchrotron radiation in the radio wave band and are likely to have one of the following two principial sources: they may either have the same origin as protons and heavy nuclei or they could be produced in secondary processes with the interstellar material according to $\pi^{\pm} \rightarrow \mu^{\pm}\nu_{\mu} \rightarrow e^{\pm}\nu_e\nu_{\mu}\nu_{\mu}$. As the positron ratio of the electron component is around 10% the second process should be the minor one.

4.3 Secondary Products and Air Showers

On the one hand incident cosmic particles interact with electrons of the atmospheric molecules which leads to an energy loss according to the *Bethe-Bloch formula* [14]

$$-\frac{dE}{dx} = Kz^2\frac{Z}{A}\frac{1}{\beta^2}\left(\frac{1}{2}\ln\frac{2m_ec^2\beta^2\gamma^2T_{\max}}{I^2} - \beta^2 - \frac{\delta}{2}\right) \tag{4.1}$$

with

K : $4\pi N_A r_e^2 m_e c^2 = 0.307$ MeV cm^2 mol^{-1}
N_A : Avogadro's number
ze : charge of incident particle
Z : atomic number of absorber
A : atomic mass of absorber in g mol^{-1}
I : mean excitation energy in eV

and x in g/cm^2. $T_{\max}$ is the maximum energy which can be transferred to a free electron. Relativistic particles which cross the complete atmosphere impart about 2.2 GeV that way.

On the other hand "cosmic" particles which are detected at the surface of the earth are in principle secondary products only. This is because the original protons undergo strong interactions mainly with the nuclei of nitrogen and oxygen. For energies higher than some GeV the same processes happen as in particle accelerators[1]: during multiple scattering inside a nucleus predominantly *pions*[2] are produced but also particles with strangeness (K, Λ, etc.) or anti-nucleons. These secondary high energetic particles cause, apart from the primary one, new hadronic interactions until the energies drop below the threshold of about 1 GeV for the production of pions. A chain reaction of such a kind is called a *hadronic shower* [4].

The secondary particles can not only interact with air molecules but they can also decay. For instance the neutral pions decay with a lifetime of $1.78 \cdot 10^{-16}$ s into photons according to

$$\pi^0 \rightarrow 2\gamma \tag{4.2}$$

and the charged pions with a lifetime of $2.55 \cdot 10^{-8}$ s into muons:

$$\pi^+ \quad \rightarrow \quad \mu^+ \nu_\mu \tag{4.3}$$

$$\pi^- \quad \rightarrow \quad \mu^- \bar{\nu}_\mu \tag{4.4}$$

The decay of the other mesons follows analogous. Their contribution to the production of muons is energy dependent. Although the muon lifetime is as short as $2.2 \cdot 10^{-6}$ s most of them reach the sea level because of the relativistic time dilatation [21]

$$\tau = \frac{E}{m_0}\tau_0 = \gamma\tau_0 \tag{4.5}$$

This mechanism gives the *muonic component* of a shower.

But in spite of the dilatation some muons do decay before reaching the surface according to

$$\mu^+ \quad \rightarrow \quad e^+ + \nu_e + \bar{\nu}_\mu \tag{4.6}$$

$$\mu^- \quad \rightarrow \quad e^- + \bar{\nu}_e + \nu_\mu \tag{4.7}$$

producing electrons. Even more electrons occur from *electromagnetic showers* initiated by the high energetic photons from (4.2). These photons produce e^+e^- pairs and these via bremsstrahlung new photons and so on. The atmosphere has, for perpendicular particle incidence, a height of about 20 radiation lengths.

So the cascade of a complete atmospheric shower consists of three components: electron-photon, hadronic and muonic (figure 4.3). The spatial development of these three branches is given schematically in figure 4.4. The different composition of secondary cosmic particles as a function of the height[3] is due to their unequal physical origins.

---

[1] Indeed a lot of new particles have been discovered from reactions with cosmic rays in the early 1950s.

[2] Pions or π mesons are understood as a pair of up and down (anti)quarks.

[3] The sea level corresponds to about 1000 g cm^2.

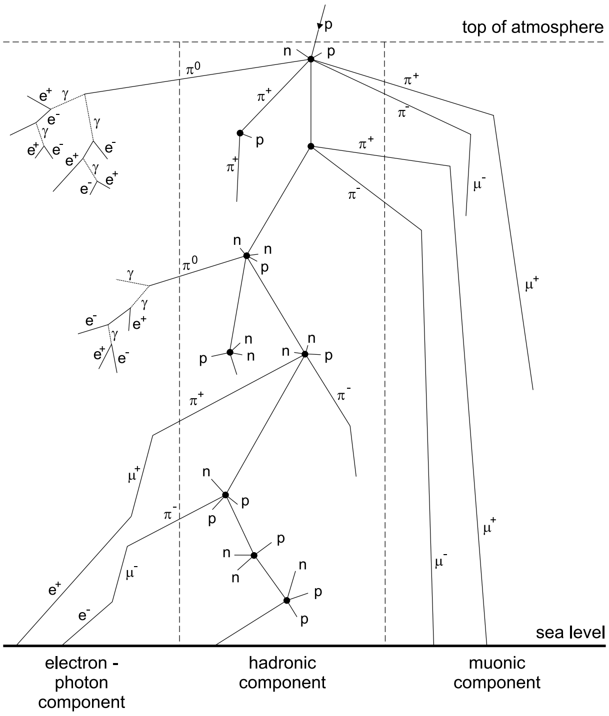

Figure 4.3: Illustration of an atmospheric shower based upon a sketch in [21]. Pions from the hadronic core cause the electon-photon and the muon component.

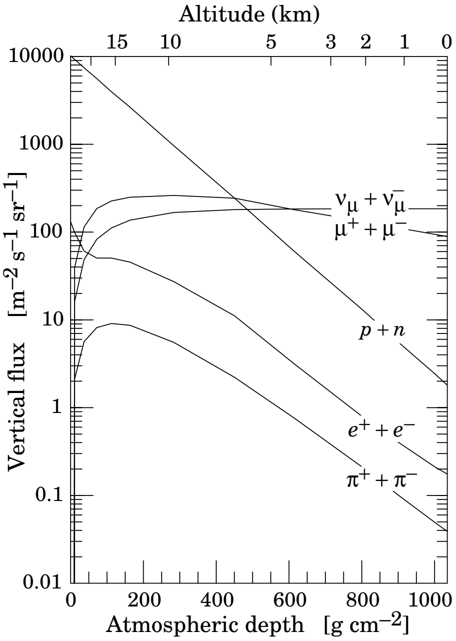

Figure 4.4: Cosmic ray fluxes with $E > 1$ GeV as a function of the atmospheric depth. The characteristics are estimated from the original nucleon flux [14].

4.4 Muons

The cosmic muons are secondary particles from cosmic showers. Figure 4.4 shows that they constitute the most frequent component of charged particles at sea level. Typically muons are produced high in the atmosphere and lose about 2 GeV according to the Bethe-Bloch equation (4.1) before arriving at the surface.

4.4.1 Energy Distribution

The energy distribution of cosmic muons is shown in figure 4.5. The spectrum reflects the production mechanism [14] and gives a mean value of $\approx$ 4 GeV at sea level. Below 1 GeV the spectrum is almost flat. The intervall from $10 - 100$ GeV is due to the original pion spectrum [21] and the steepening at even higher energies happens since pions with $E_\pi > M_\pi c^2 \approx 115$ GeV are likely to interact with the atmosphere before they decay.

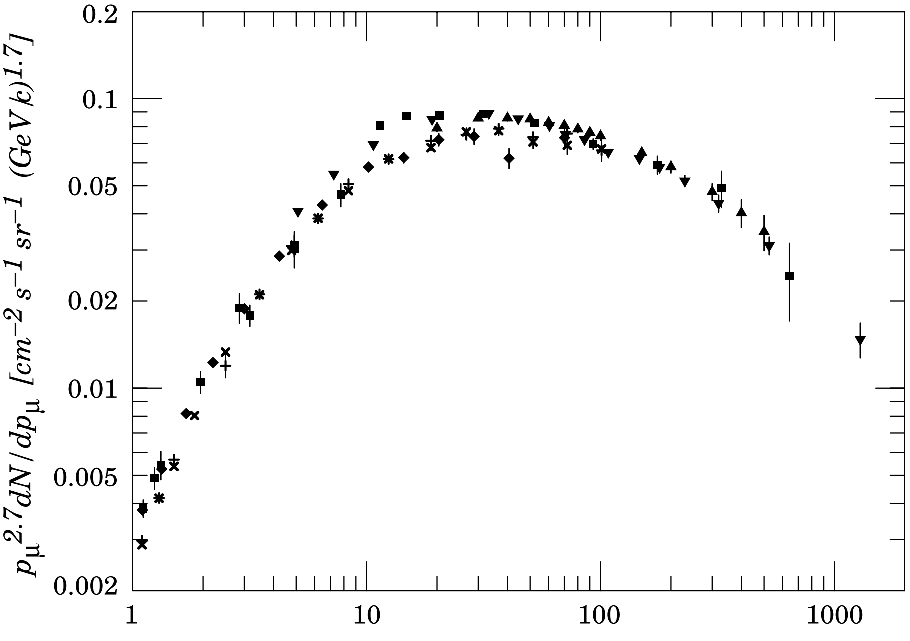

Figure 4.5: Momentum spectrum of muons with vertical incidence [14].

4.4.2 Angular Distribution

The production of muons by meson decays yields the dependence of the muon flux on the inclination angle [21]. The first contribution is the change of the atmospheric depth with the zenith angle and the shift of the muons towards the low energy cutoff. The second mechanism is that unstable particles are more likely to interact with the atmosphere than to decay at vertical incidence compared to the declined case. So for pions and other mesons there is a competition between interaction and decay.

The angular distribution of muons at ground level as a function of the zenith angle α is [21]

$$\frac{I(\alpha)}{I(0)} = \cos^n \alpha \tag{4.8}$$

whereas the energy dependent exponent n has the value 2 for muons with $E_\mu \approx 3$ GeV. For this case the distribution is sketched in figure 4.6.

4.4.3 Lateral Muon Distribution in Air Showers

The energy and angular distributions only included the uncorrelated muon fluxes. But of course a cosmic shower also has a lateral distribution. Shower particles depart more and more while they travel through the atmosphere. Since they all move with the speed of light they form a slightly curved disc with a diameter of about 1 km and a thickness of approximately 1 m near the shower axis which increases to around 100 m further outside.

Here, since this diploma thesis concerns with muon chambers, only the muonic component is of interest. In [23] the following estimations for the lateral distributions can be found: the total number of muons at sea level with energies above 1 GeV is

$$N_\mu(> 1\text{ GeV}) \approx 0.95 \cdot 10^5 \left(N_e/10^6\right)^{3/4} \tag{4.9}$$

where N_e is the number of all charged particles in the air shower. An approximation of the number of muons per square metre ρ_μ as a function only of the total number of muons and the lateral distance r (in metres) from the shower axis is

$$\rho_\mu = \frac{1.25 N_\mu}{2\pi\Gamma(1.25)} \left(\frac{1}{320}\right)^{1.25} r^{-0.75} \left(1 + \frac{r}{320}\right)^{-2.5} \tag{4.10}$$

with the gamma function Γ. Figure 4.7 plots the muon density distribution for the case of $N_\mu = 10^4$ muons.

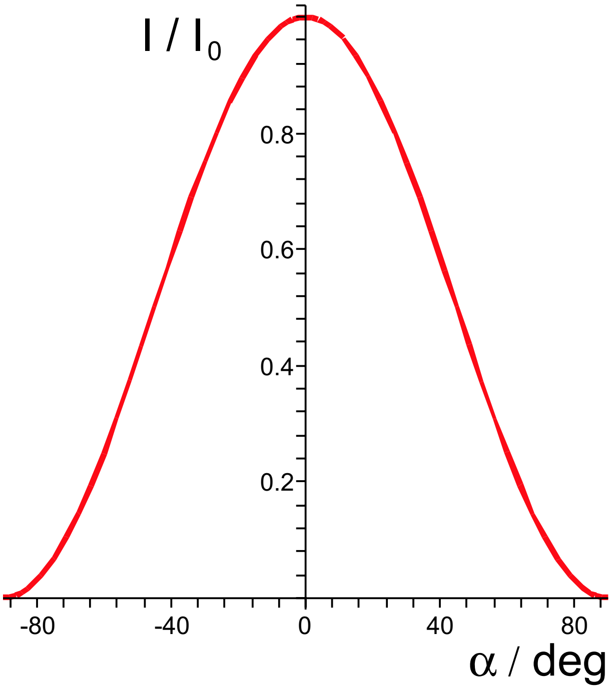

Figure 4.6: Angular distribution of muons with $E_\mu \approx 3$ GeV at ground level.

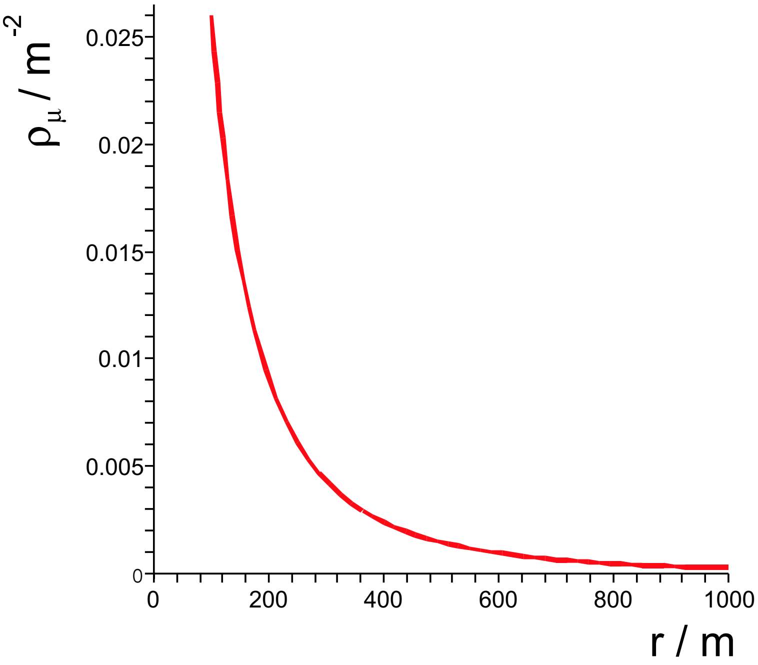

Figure 4.7: Muons per square metre as a function of the lateral distance r from the axis in a cosmic shower with 10^4 muons.

Chapter 5

CMS Drift Chambers and the Test Stand

All in all 70 of the 250 CMS drift tube chambers are produced at Aachen University. Before these are transported to CERN the fulfilment of certain quality criteria must be assured. The final test on location is to take data from cosmic muons with a test stand and a data aquisition for that purpose.

5.1 Drift Chamber Layout

CMS drift tubes have a more advanced design than described in chapter 3.4.1. The realised drift cell is 42 mm wide, 11.5 mm high and, depending on the station, 2–4 m long with the anode wire at +3.6 kV in the centre, see figure 5.1. On the left and right of every cell are 1 mm wide aluminium beams to separate the cells and to hold the cathodes which recieve a voltage of about −1.2 kV. The cathodes are realised as aluminium strips which are laterally glued onto the I-beams, insulated by thin mylar foils. The beams also protect the other anodes in case of wire breakage, partially decouple contiguous cells from electromagnetic debris and provide mechanical stability to the chamber.

The top and bottom sides of the cells are bounded by grounded 1.5 mm strong aluminium plates with positively biased (+1.8 kV) field forming strips at their centre which "squeeze" the electric field, yielding an improved linearity of the distance-time relationship and a better resolution of the cell. Detailed studies on the high voltage are described in [24]. The used chamber gas is an Ar/CO_2 mixture at a ratio of 85/15.

CMS drift tube chamber modules contain twelve layers of driftcells, each with a total height of 13 mm. Groups of four compose a so called *superlayer*, altogether sealed gas tight, providing all the connections for read out, high voltage and the gas provision. The single drift tubes have a horizontal periodicity of 42 mm and the individual layers within

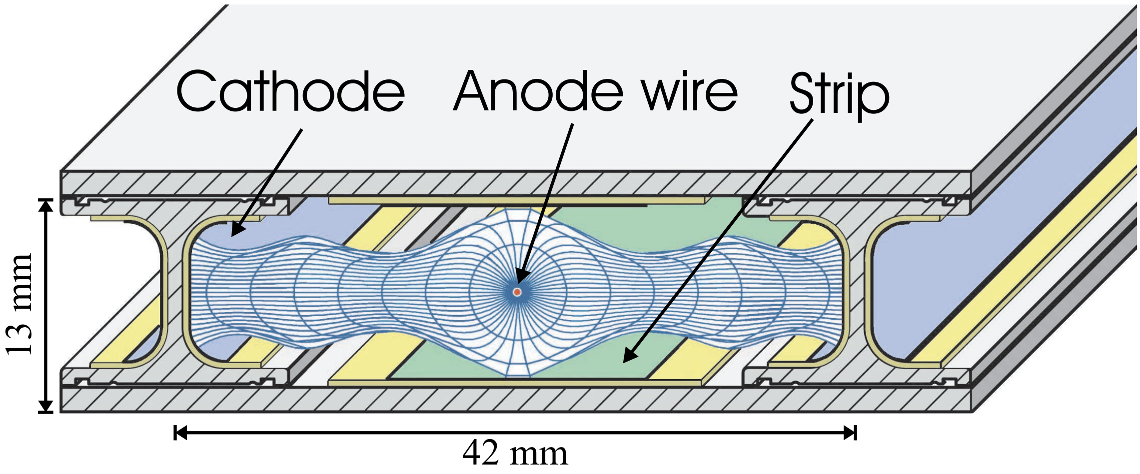

Figure 5.1: Cross section of a CMS drift cell with electric field lines and lines of equal drift time plotted [25].

a superlayer are staggered by half a tube. The upper and lower superlayers, called Φ-SLs, are oriented in the same direction while the one in the middle, named Θ-SL, is rotated by 90° to cross the outer ones perpendicular. Between the two lower superlayers a honeycomb plate is mounted as a spacer. The total size of such a chamber depends on the position it is planned to be integrated at the CMS detector. The so called MB1 chambers, which are produced in Aachen and whose test is subject of this diploma thesis, have an extent of 200 cm × 255 cm × 30 cm. For details about the building of MB1 chambers read [10], [26], [27] and [28].

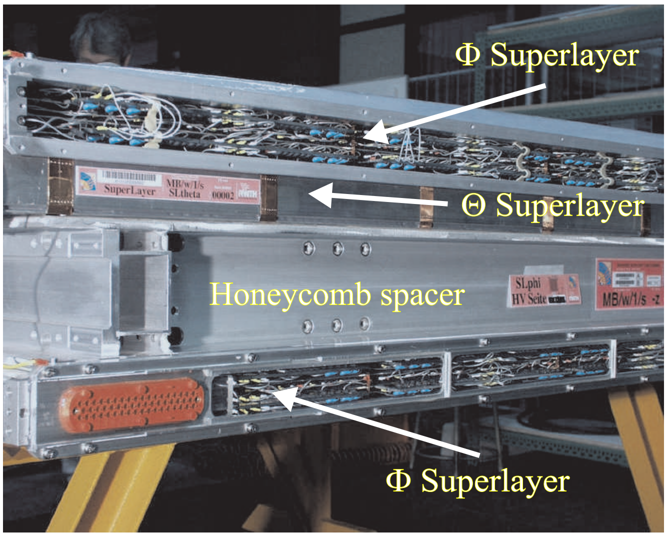

Figure 5.2: A view from the side on a MB1 muon chamber produced at Aachen.

5.2 Test Stand and Data Aquisition

There are several kinds of tests a muon chamber has to pass before being installed to CMS [29], like for example a measurement of the anode wire positions and tensions [10], a high voltage test [24] and a gas tightness check [27]. The final step is to screen a complete superlayer and finally a whole chamber in a test stand by taking drift time data from cosmic muons and to write them into a database afterwards. One can use the stored information for track reconstructions and hence to calculate quality parameters like the efficiency per cell, the track resolution and others.

The photograph in figure 5.3 shows the test stand at Aachen. The main components are hold by the pink base frame: a layer of plastic szintillators as trigger on top of several vertical iron beams and another trigger layer just above the floor. In case the installed electronic system detects coincident signals in both layers it is assumed that a muon has crossed the test stand and thus it must have penetrated the superlayers and chambers which have been inserted horizontally to the base frame, too.

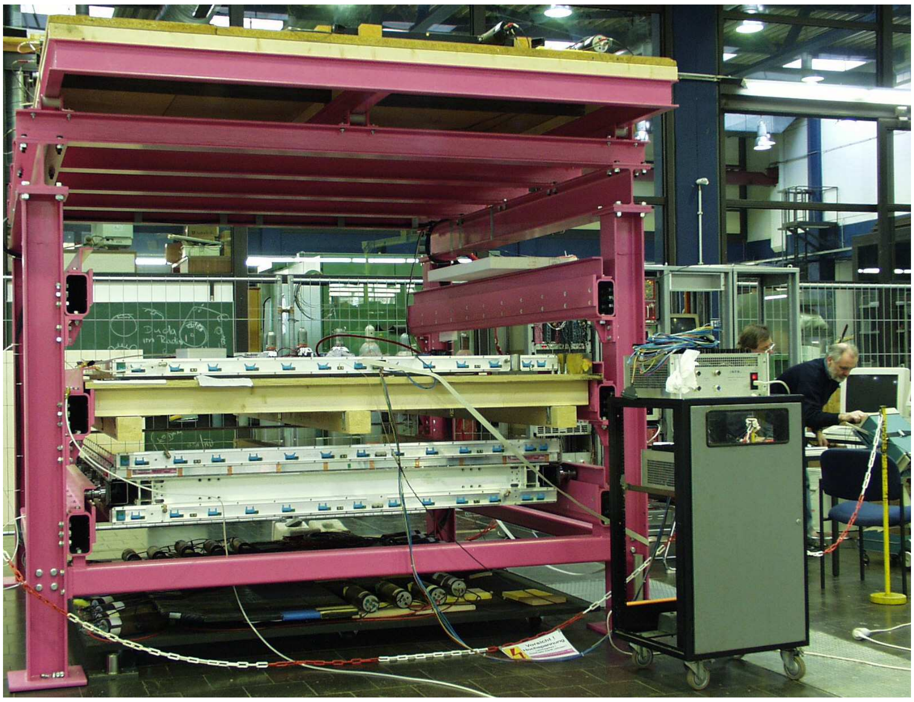

Figure 5.3: A photograph of the cosmic muon test stand. The picture shows a complete chamber at the bottom level and a single superlayer at the position above.

The pre-amplifiers of the superlayer read out the drift tube signals and form a standard pulse using discriminators. These digital LVDS pulses are converted to ECL and transmitted to LeCroy TDCs[1] (model 2277) [31], a solution just for the data taking at Aachen since the TDCs later used in the CMS experiment have native support to process

---

[1] Time-to-digital converters.

LVDS signals [24]. The LeCroy TDCs have ring buffers which are read out after the about 10^4 ns delayed trigger signal [30] has caused a common stop. The information from the TDCs is carried forward via a CAMAC crate to a HP-CPU inside a VME crate which saves the data for further analysis. Afterwards the stop signal is cancelled and the system reset, awaiting a new trigger coincidence. As described in [32] it is convenient to convert a recorded data file with many events inside to a so called *tree* saved inside a `.root` file, a format which can easily be accessed within the software framework ROOT [33]. In case all three superlayers of a chamber are read out each one gets its own data file. So in the following only the case of superlayer tests is described.

5.3 Accessing the Saved Data

Now with access to the database of the data aquisition (DAQ) it is possible, with ROOT installed, to run the CINT/ROOT C/C++ interpreter and then start the built in object browser [33]. Simple analyses such as inspecting the occupancy, i.e. the number of hits per cell integrated over all taken events, can already be done right from the start, and with some programming more complex analysis would be possible. But since such an interpreted program is a lot slower than a compiled one, as each command has to be translated into machine language again and again during data procession, the decision was clear to follow the latter approach and use a compiler as a single data file can contain up to some million events.

Not to presume too much familiarity with programming and the C++ language in particular during the further elaborations most explicit code is placed inside appendix A. Anyway, the first step is to declare a data structure like

```
struct raw_event {
  Int_t event_number;
  Int_t hits_in_event;
  Int_t hits_in_cell[MAX_CELLS];
  Int_t cell_number[4097];
  Int_t tdc_datum[4097];
};
```

containing all the information stored for a triggered event. Since the ring buffers of the TDCs can keep up to 16 hits within the total time window of 65,536 TDC ticks, with the ticks being 1 ns apart, one gets 4,096 hits with the existing 256 TDC channels in the worst case scenario. The implemented array dimensions only exceed this value by one for compatibility with the conversion software.

Each event in a file is assigned a unique event number. That is useful for future examinations with a whole chamber read out, because data of the same event, just from different superlayers, are stored into separate files as already explained. The C++ structure element holding the number of hits within an event and the array containing the number of hits per cell are redundant in principle, as this knowledge can be deduced from the two remaining arrays storing for every hit the number of the affected cell and the measured drift time in TDC ticks.

The cell numbering scheme used is the following (see figure 5.4): the upper left cell, seen from the front end electronics side, is cell 1, the cell two layers below at the same horizontal position is cell 2. Then cells number 3 and 4 are the next ones to the right in the two layers with half a cell width offset, et cetera, ending with cell 196 for Φ superlayers and cell 228 respectively for Θ superlayers. The single drift tube layers themselves are numbered 1 to 4 from top to bottom.

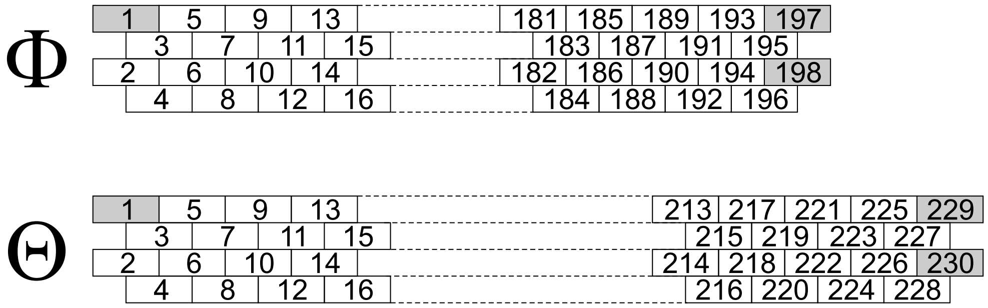

Figure 5.4: Cell numbering schemes for Φ and Θ superlayers. The shaded cells are either not connected or do not have an anode wire

5.4 Data Interpretation

For an Ar(85%) CO_2(15%) gas mixture simulations of the electron transport in dependence on the electric field yield a drift velocity remaining about constant within the interval from 10^3 to 10^4 Vcm^{-1}, see figure 5.5. Thus a good approximation of the r-t relation is already given by

$$r(t) = v_{\mathrm{drift}}\,|t - T_0| \tag{5.1}$$

with T_0 as the moment the trigger fired and with the drift velocity v_{drift} typically about 55 μm/ns [27]. Anyhow, small variations of the drift velocity are inevitable, especially close to the anode wire due to the high field strength nearby. This circumstance directly reflects in the recorded data.

The diagram in figure 5.6 is called a *drift time spectrum.* In this case it is filled with the recorded drift times integrated over all the cells of a superlayer for more statistics. The closest hits to the anode wire give entries on the right with $t \approx 10,260$ ns while the hits next to the aluminium cathodes give entries at $t \approx 9,870$ ns. This "reversed" order appears due to the common stop of the TDC ring buffers. Assuming a uniform distribution of muons over the cell width one expects a box shape as all the drift times should have the

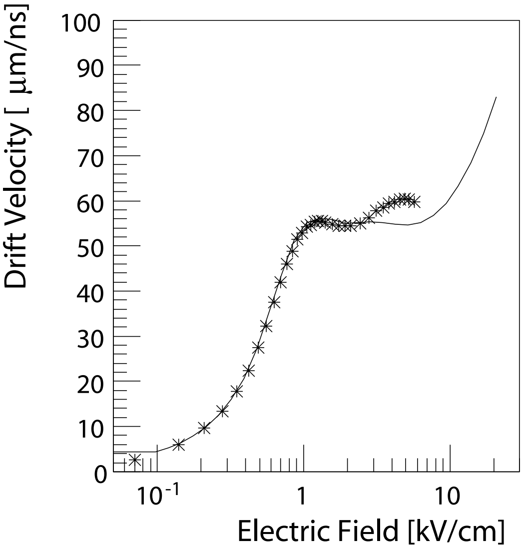

Figure 5.5: Dependence of simulated (solid line) and measured (stars) drift velocity on the electric field [18].

same frequency. The visible structure instead is due to variations of the drift velocity with the peak corresponding to the area of high field strength around the wire. Furthermore, the tail on the left, at $t < 9850$ ns, is caused by afterpulses which appear if photons are emitted during gas amplification which kick out new charges from the cathode. The jitter structure atop the spectrum is TDC intrinsic and not understood.

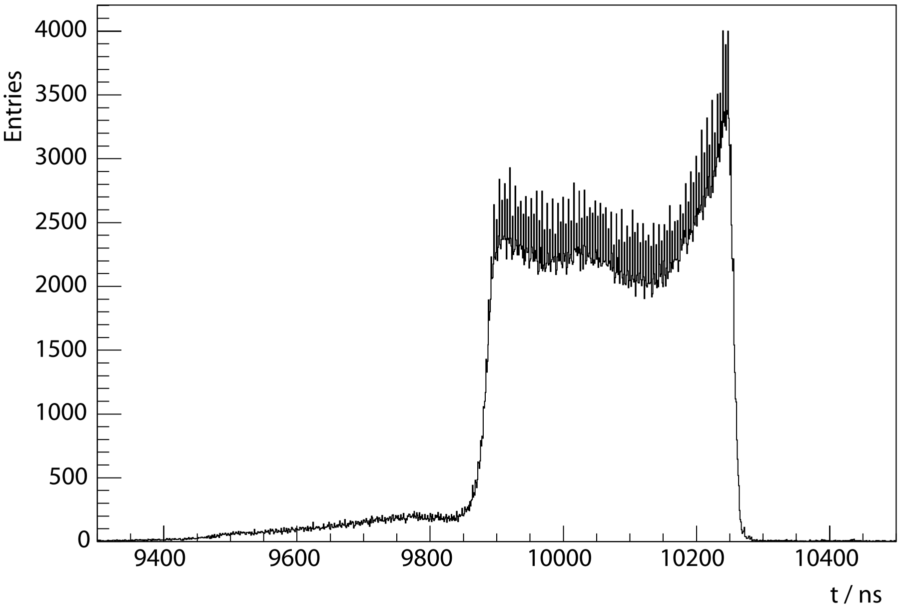

Figure 5.6: A global TDC drift time spectrum. The distressing spikes atop are due to non-understood TDC ijitter.

Chapter 6

The Track Reconstruction Software

For further analysis it is necessary to calculate the tracks of the traversing muons from the recorded drift time data. This chapter introduces a method performing this task.

6.1 A Track Reconstruction Algorithm

There already exist algorithms to reconstruct particle tracks from drift times. For instance an approach alternative to the one described in the following can be found in [28]. Moreover a previous track reconstruction software [34] for MB1 superlayer tests with cosmic muons at Aachen is available. Unfortunately it only works with the ROOT C++ interpreter which turned out to be too slow and unstable in practice. The algorithm presented in the following differs from both approaches and allows in principle a more complex modelling of the drift lines and isochrones, i.e. zones of equal drift times.

6.1.1 Requirement

A typical event display is seen in figure 6.1. Here circles represent the measured drift distances since the drift direction is initially unknown. The cells with a recorded hit are marked in green colour. Visible to the eye is that the red arrow shows the hypothetical muon track since it agrees best with all measured drift distances. So obviously an algorithm is required which performs the track reconstruction, yielding an automated event analysis later on.

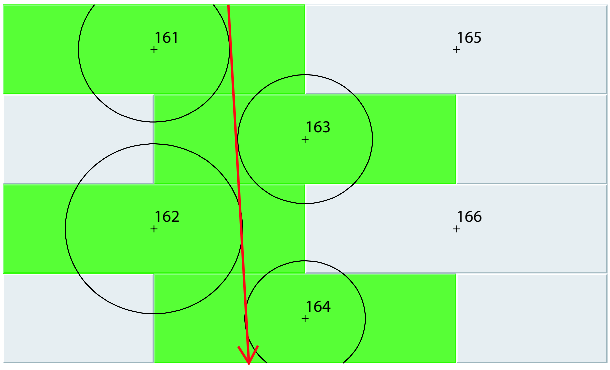

Figure 6.1: In this event display rectangles represent the drift cells with the wire positions marked at their centres. The hit cells are green coloured with circles indicating the measured drift distances. To find the muon track (red arrow) is the task of the track finding algorithm.

6.1.2 Track Parametrisation and Isochrones Modelling

Cosmic muons are energetic enough to neglect multiple scattering within a superlayer during the track finding. Hence straight lines describe muon traces and, since single superlayers allow for two dimensional reconstructions only, two parameters, the horizontal coordinate x of the transition point inside the upper aluminium plate and the angle α of the track inclination as defined in figure 6.2, provide the desired information. In the following it is convention that an angle as sketched in figure 6.2 has a positive sign.

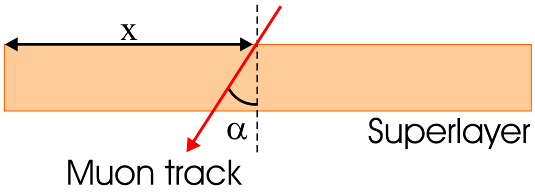

Figure 6.2: A muon track is described by a straight line or arrow with a horizontal offset x from the upper left corner of the superlayer and the inclination angle α.

A second look on figure 5.1 makes clear that the r-t relation from equation (5.1) may be too simple since especially for inclined muons at large drift distances the assumed isotropy is not given any more. So an angular dependence should be taken into account. In theory it is possible to use $r(t, \alpha)$ from simulations as presented in [24], but for simplicity the following model is realised (see figure 6.3): up to a fixed range, in the following 25% of the cell height, the isochrones are given by cylinder jackets around the anode wire and behind a purely horizontal drift is assumed.

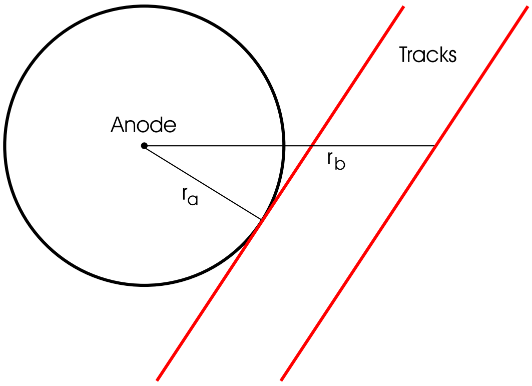

Figure 6.3: The used drift model yields a distance r_a for a track close to the anode wire and r_b for a parallel track outside the cylinder jacket zone.

6.1.3 The χ^2 Method

The recontruction algorithm has to find a track that keeps the inevitable gaps – the detector is not perfect – between the muon transition line and the isochrones as small as possible. For that purpose it is common to use the χ^2 method [35]. The aim it to find the track parameters x and α minimising the χ^2 function given by

$$\chi^2 = \sum_{i=1}^{n} \left(\frac{\Delta_i(x, \alpha)}{\sigma_i} \right)^2 \tag{6.1}$$

for n measured drift distances with an assumed constant error of $\sigma_i = \sigma = 250\ \mu\text{m}$ which is set as maximum by the technical design report of the CMS muon system [18]. Δ_i is the size of the gap between the track, thus the x and α dependence, and the isochrone of hit number i. Obviously a single minimum of (6.1) only exists for at least three hit cells, but ambiguities can still occur in some cases focused on later. To get comparable values of χ^2 for different numbers of hits n it is usual to divide the χ^2s by the number of the remaining degrees of freedom $n_{\text{dof}} = n - 2$ since two of them are already consumed by the track parameters.

With the drift model as described in the previous section and some analytical geometry the remaining task of the track finding algorithm is now to find a track candidate, parametrised by x and α, yielding the smallest possible χ^2.

6.1.4 The Reconstruction Algorithm

A brute force approach to find the optimal x-α combination would be to sample the x-α plane fine-grainedly enough and keep the point with the best χ^2. This has been done exemplarily for the event displayed in figure 6.1 and the result is shown in figure 6.4. For a better visibility the negative base-10 logarithm of χ^2 is plotted as a function of the track parameters. Unfortunately this method is quite slow.

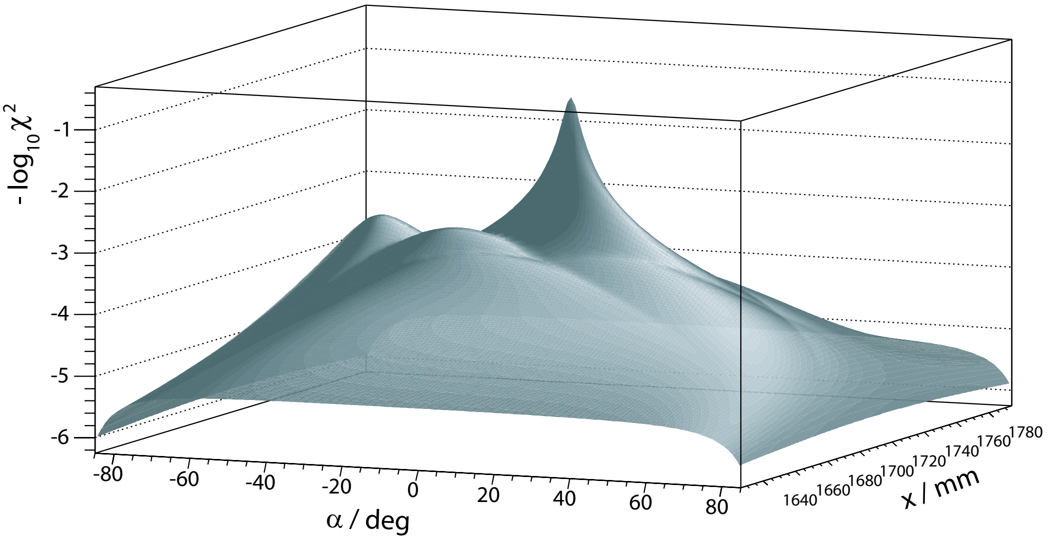

Figure 6.4: An example of the χ^2/n_{dof} dependence on the track parameters x and α. Plotted is the negative base-10 logarithm so in this picture the algorithm has to find the highest peak and must not return one of the lower extrema.

Another possibility is to define a starting point, for example a vertical track through the mean horizontal position of the hit cells, and follow the negative gradient of $\chi^2(x, \alpha)$ which of course leads to an extreme value, but maybe just a local one. The idea of the algorithm finally chosen is based upon the gradient method together with a decreasing random jitter, inspired by the Boltzmann method in [36].

The initial x position is given by the average position of the hit cells whose drift times are used and a starting angle of 0° is suggested. In addition an interval which shall be searched for a better track is set to $x_{\mathrm{step}} = 40,000\ \mu$m, thus about the cell width, and $\alpha_{\mathrm{step}} = 90°$. The following procedure is illustrated by the flow chart in figure 6.5: A random point within $x \pm x_{\mathrm{step}}$ and $\alpha \pm \alpha_{\mathrm{step}}$ is taken and its χ^2 compared to that of the present track choice. If a better χ^2 was found x and α are set to these new values, receiving a new track candidate. Now the step sizes are reduced by a certain factor and, unless the x step width reaches less than 1 μm, a new and better candidate at another random point is tried to be found. In the end the best track discovered that way is kept. Figure 6.5 shows a flow chart of the track finding algorithm. This method resolves the initial left right ambiguities of the individual cells automatically.

The final implementation is slightly more complicated than just described since within every loop of the procedure not only one track candidate within the parameter step widths is tested but all combinations of the signs (+,0,-) of x_{step} and α_{step} are tried for the best candidate. Without that modification of the algorithm it appeared that sometimes the global extremum could not be found. Please see appendix A for the C++ source code of the extended method.

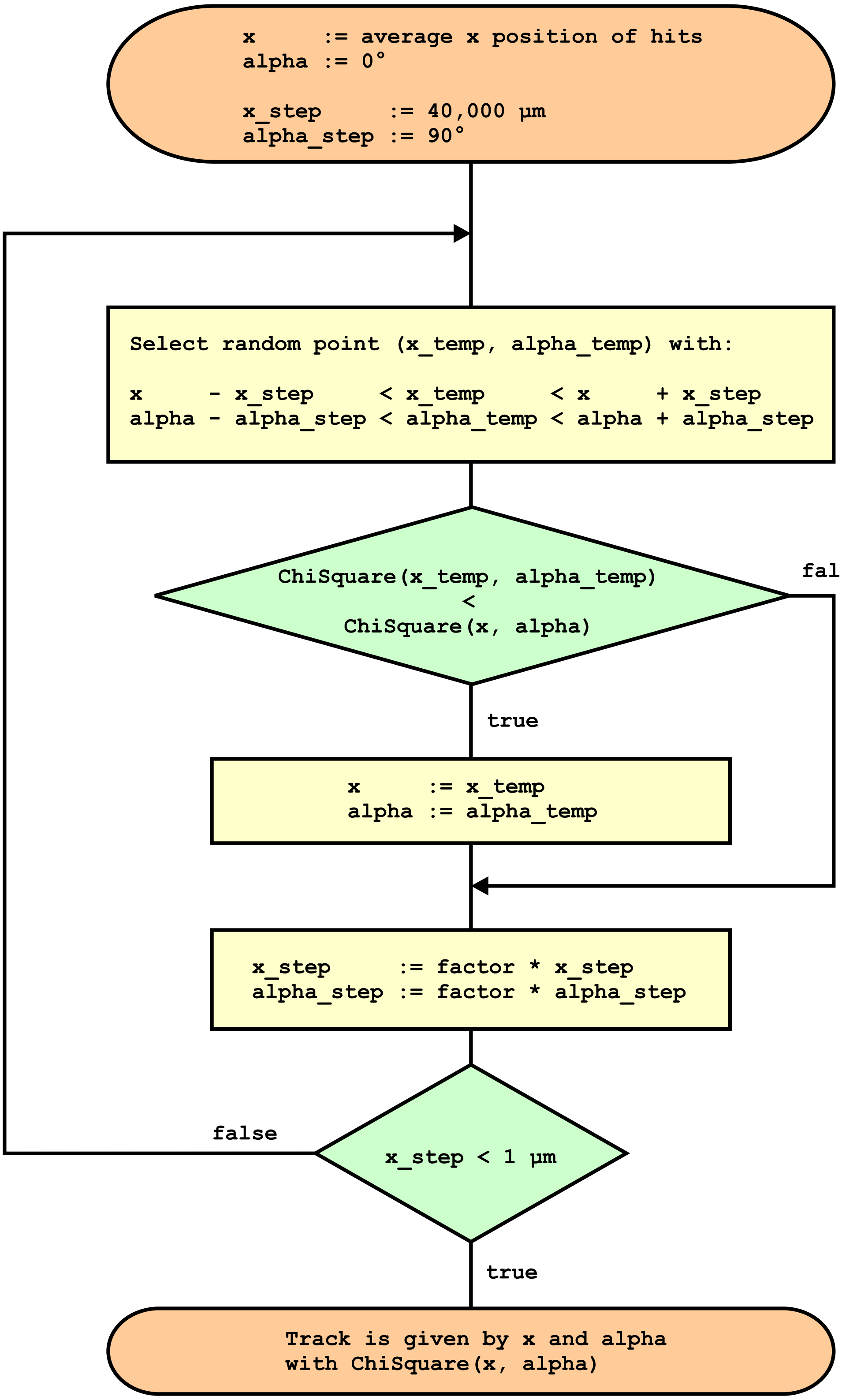

Figure 6.5: The flow chart of the track finding algorithm.

6.1.5 Quality of the Calculated Fits

Since the track finding contains a random element it can not be guaranteed that the best track is found in every case, but to test the reliability single events were fitted multiple times and the reproducibility in practice could be affirmed. A typical result is given by figure 6.6: the fit procedure always arrives with high precision at the same result. The used damping factor of 0.85 means that 65 iterations[1] had been necessary until the stop criterion was reached. Systematic analysis shows, see figure 6.7, that a higher damping factor does not improve the track quality any more. The product of the RMSs with the number of iterations reaches a minimum for a factor of 0.82. A damping of such a kind can be seen as the best compromise between accuracy and speed.

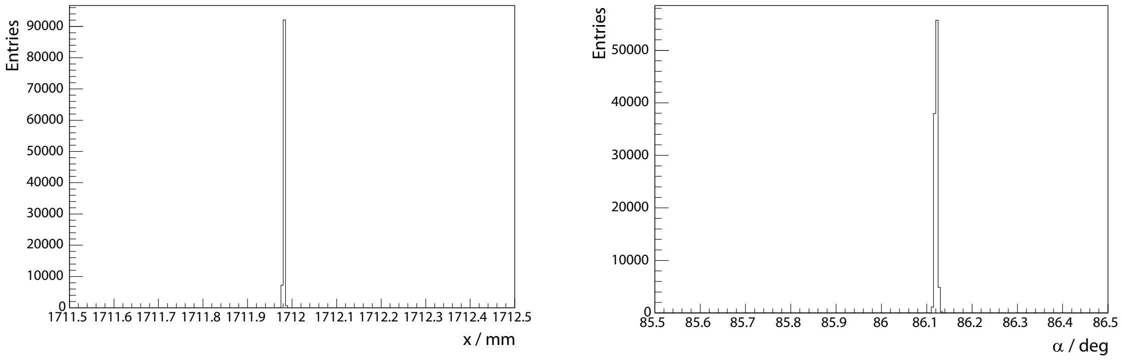

Figure 6.6: Here the event from figure 6.1 was fitted 100,000 times with a damping factor of 0.85. A RMS of 0.44 μm for x and 0.0025° for α was calculated.

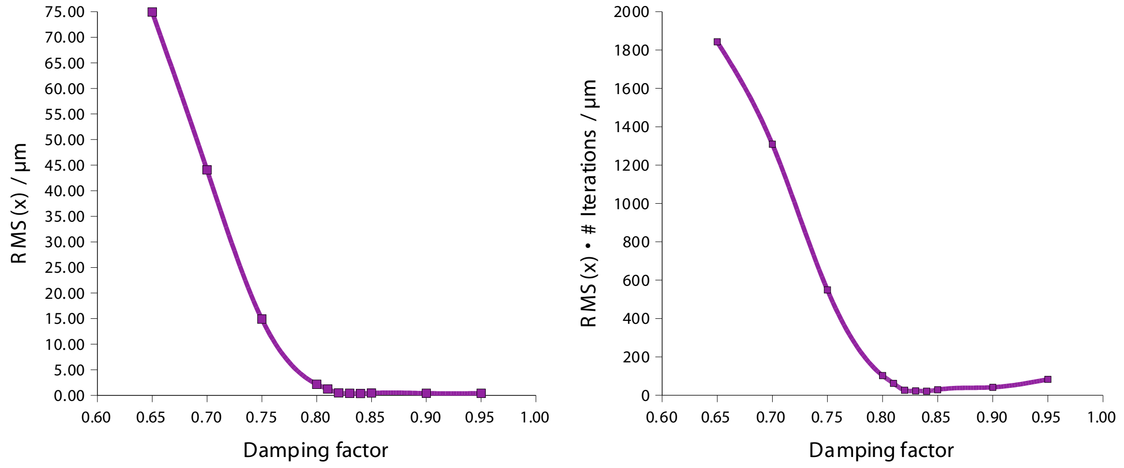

Figure 6.7: It does not make sense to choose a damping factor larger than 0.82 since the track quality is not improved any more. Only the number of iterations, i.e. the computing time, increases. The RMSs of α yield the same conclusion and are hence omitted.

---

[1] The number of iterations, for the parameters suggested here, is $n = \frac{\ln(1\ \mu m/40{,}000\ \mu m)}{\ln \text{factor}}$

6.2 Advanced Track Fitting

Not all measured drift times are necessarily part of a muon track. The recorded data may contain noise hits in other cells or even in the same ones already traversed by the muon. Sometimes even several muons from an atmospheric shower may pass the superlayer at the same moment.

6.2.1 Noise

From time to time, $30-40$ Hz are typical, a drift cell produces a *noise hit.* The reason may be a random charge avalanche inside the drift tube or noise within the used electronics. Since the whole drift time window covers more than 65 μs and only less than 400 ns correspond to distances within the geometrical cell limits, it is very likely that a noise hit is already sorted out by demanding drift distances shorter than half the cell width within some tolerance.

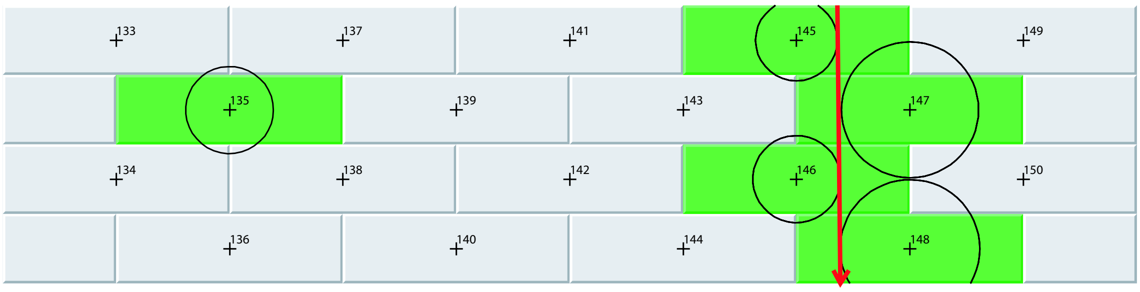

Figure 6.8: This event contains a noise hit in cell 135 which has to be disregarded.

Events, like that in figure 6.8, with a noise hit whose drift length lies inside the cell, are treated as follows: groups of one or two hits inside the acceptable time window can not yield a track and are regarded as noise in case the distance to a group of three or more hit cells, probably due to a muon, is larger than two cell numbers. This method works unless a cell with a noise hit directly touches a track.

6.2.2 Multiple Hits

Noise hits may also be measured in cells that already contain a drift distance from the muon yielding two or even more hits for the same anode wire. This does not happen as rarely as one might think at first! The already introduced drift time spectrum, figure 5.6, contains a trail of so called *afterpulse hits* which are caused by photons produced during gas amplification. These may knock out further electrons, most likely from the cathode or the field forming strips[2], which then start a new charge avalanche.

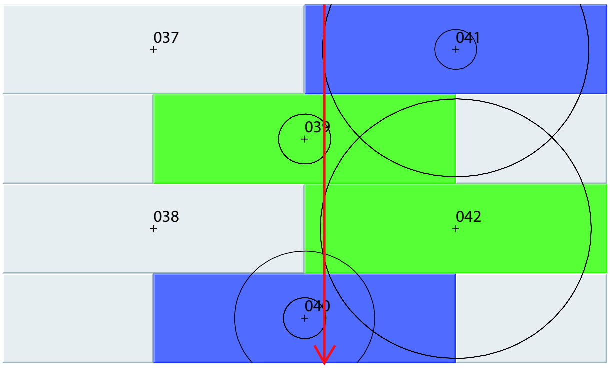

Figure 6.9: The blue coloured cells detected two hits.

Even though the innermost hit is very likely the one to take, one should test all of the candidates as sometimes it turns out, have a look at the event display in figure 6.9, that in certain cases this is not true. So all permutations[3] are tested and the combination with the track giving the best χ^2 is finally taken.

6.2.3 Events with Several Tracks

As muons are produced in cosmic showers in large numbers a single event need not necessarily contain only one traversing muon but also several of them since it is quite likely that from time to time some of them traverse the superlayer simultaneously. Now the challenge is to separate them.

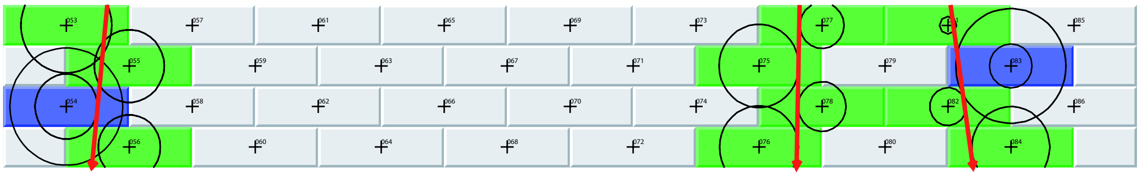

Figure 6.10: This event contains three clusters of hit cells. A muon track can be reconstructed for each of them.

The implemented practice is somewhat simple but suffices to distinguish muons which are about one cell width apart: all hit cells are divided into clusters. Again at least two non-hit cells of consecutive cell numbers are taken as boundary. So a group may contain single inefficient cells within. Of course a more advanced procedure could be implemented but this is not done here since for the separation of touching tracks a lot of cell combinations would have to be tried which would consume too much computation

---

[2] The drift lines from the field forming strips to the anode wire are so short that knocked out electrons from there follow too soon after the original hit to be recognised by the used electronics .

[3] unless the number of them is not too large. The maximum chosen here is 64.

time. Such a potential is not needed here anyway since the superlayers shall only be tested and there are plenty of simpler events in the data file that can be taken to provide enough statistics. The unresolved double tracks do not disturb the analysis later on as the assigned tracks are of poor quality and hence sorted out.

For details about the actual C++ implementation refer to the source code in appendix A. As a short summary: all events are divided into sub-events that correspond to cell clusters and sub-events contain several sub-event candidates in case one or more cells contain multiple hits with each hit permutation being such a candidate. For each cluster only the best candidate is chosen.

Chapter 7

First Analyses and Optimisations

With the track reconstruction algorithm it is possible not only to examine single events but complete data files. Sufficient statistics provided, one can learn more about the superlayer properties which again can be used to improve the quality of the reconstructed fits.

7.1 The χ^2 Cut

Not all tracks are of the same quality and the decision whether to take a track for analysis later on or leave it is made upon its χ^2. Certainly the introduced noise filters and the track separation are applied before the reconstruction. Doing so and taking all fits yields a χ^2 distribution as shown in figure 7.1 and setting the χ^2/dof cut to 10 in future keeps about 60% − 70% of the events in practice. Most of the remainder does not give a sensible track as noise hits or multiple tracks can not be resolved. Division of the χ^2 distribution according to the track inclination shows mainly a statistical difference. The number of muons decreases with larger angles due the original cosmic distribution and effects of the trigger geometry. All following examinations use a cut of 30° on the absolute value of the track inclination angle α.

7.2 Track Parameter Distributions

Now with such a χ^2 cut and enough statistics some analyses can already be performed. It is possible to count the number of tracks as a function of their horizontal position or just their inclination (figure 7.2). The distributions are in general as expected: less tracks at the superlayer borders since at these x positions inclined muon tracks pass the trigger either on top or at the bottom of the test stand only. The reasons for more muons with about perpendicular tracks have already been discussed. Further on x-α correlation plots reveal the trigger geometry (figure 7.3): lines fom the upper left to the lower right are

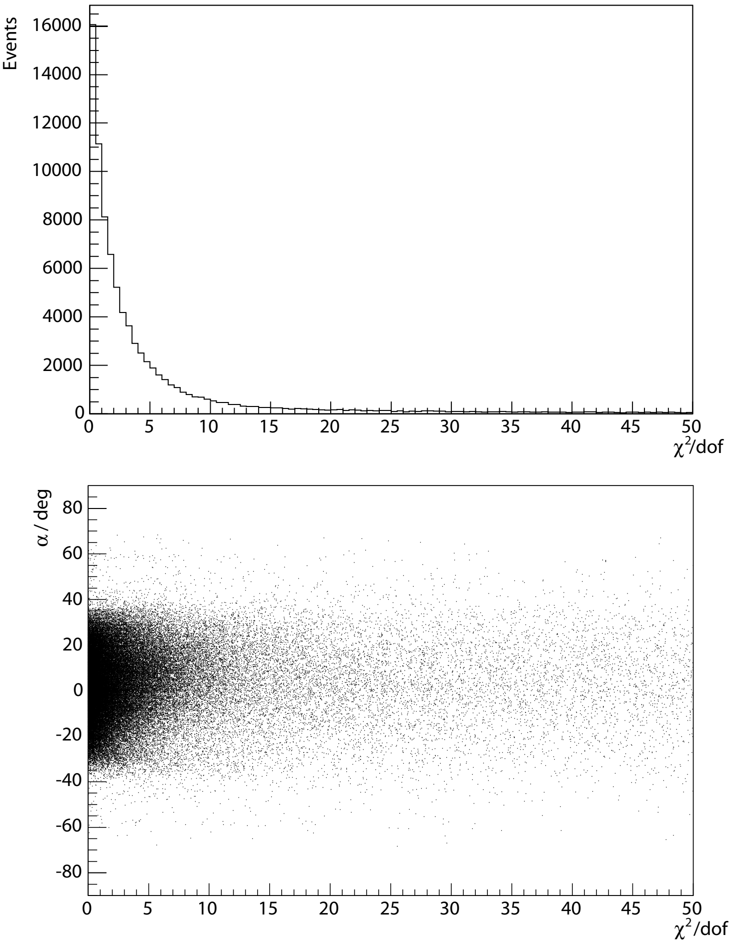

Figure 7.1: After fitting a large number of tracks one gets a χ^2 distribution as shown on top. Here only events with three or four hits have been taken. Additional subdivision by track angles (bottom) shows that an inclination independent χ^2 cut causes no problems.

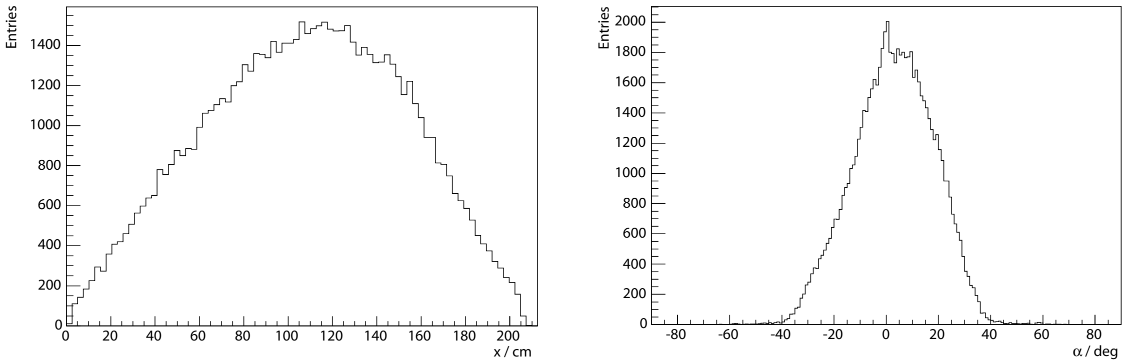

Figure 7.2: Track parameter frequencies, sorted by either the horizontal position or the track angle.

gaps, borders or just inefficiencies of the roof triggers and structures from the upper right to the lower left are caused by the floor triggers. That way it is possible to discover and examine trigger malfunctions offline.

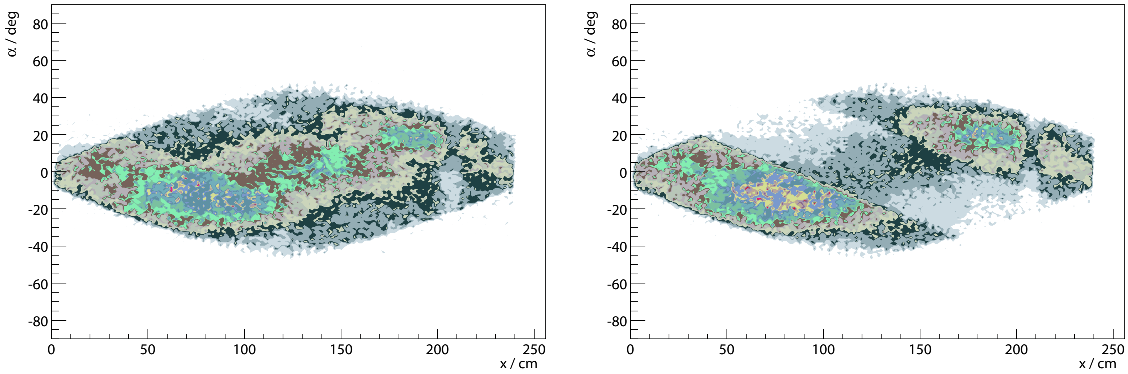

Figure 7.3: Contour plots of the x-α correlation make trigger structures visible. The picture on the right shows a gap as a roof trigger had been defective.

7.3 Track Residuals

A powerful quantity to control the excellence of the fits is named *track residual*. It can be calculated for every hit that takes part in the reconstruction and is defined as the signed distance between the best fit track and the isochrone of the hit. Here by definition the residual is positive for tracks outside the isochrone and negative for tracks closer to the anode wire than the drift distance. It is expected that both cases appear with the same frequency and so residual distributions should peak at zero.

Figure 7.4 contains such histograms integrated over all cells for each layer. Since the drift distances of the outer layers influence the track fit more than the inner ones, due to their longer lever arms during reconstruction, the gaps between isochrones and tracks are smaller in these regions. A narrower residual distribution is the consequence.

It is possible to calculate the resolution of the drift tubes from the histogram widths. But since the results of the track fits can be improved further, manifesting in smaller RMSs of the histograms, the real discussion of the resolution follows later on.

If track residuals are taken individually for each cell it can happen to obtain distributions for some cells that do not peak at zero. In such cases there is the suspicion of incorrect r-t relations. Figure 7.5 shows that behaviour for a group of eight cells. Systematic studies did lead to the result that a chip of a TDC, responsible for just these eight channels, did not operate properly. A closer look upon the affected TDC spectra showed strong jitter and shifted T_0 edges. And as for some time no replacement of that hardware component had been possible an offline correction was desired.

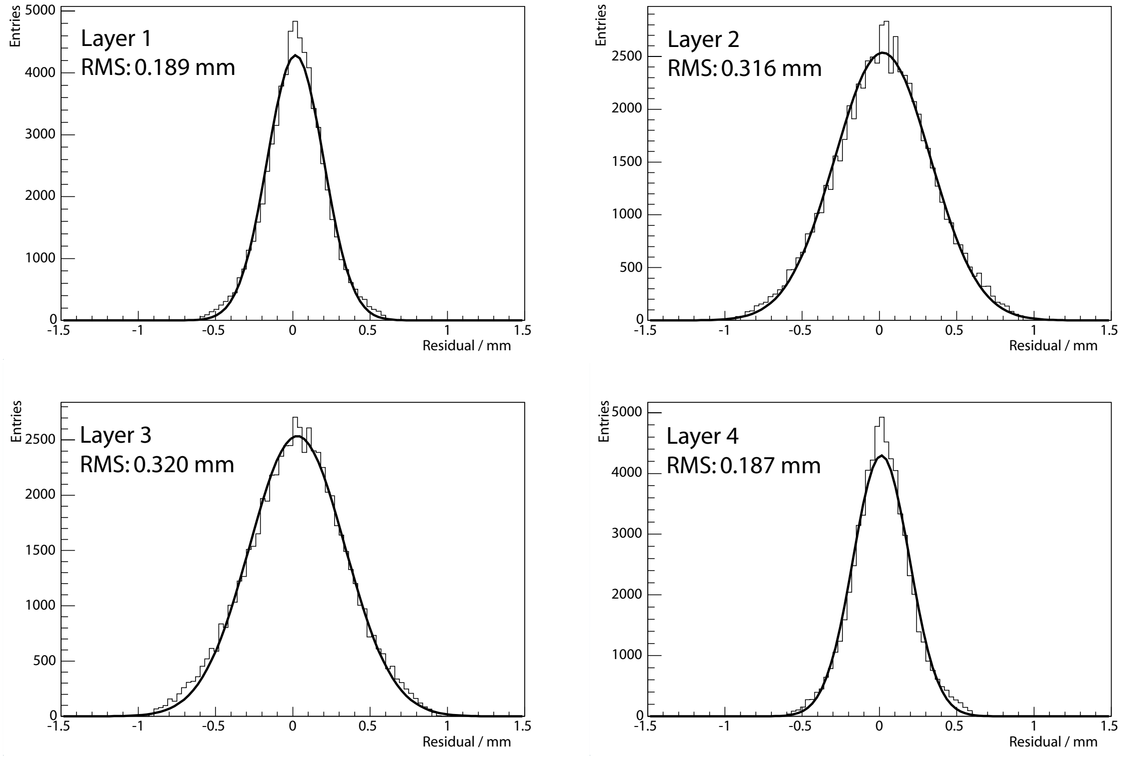

Figure 7.4: The distributions of the track residuals of SL 10 sorted by layers with Gauss fits applied.

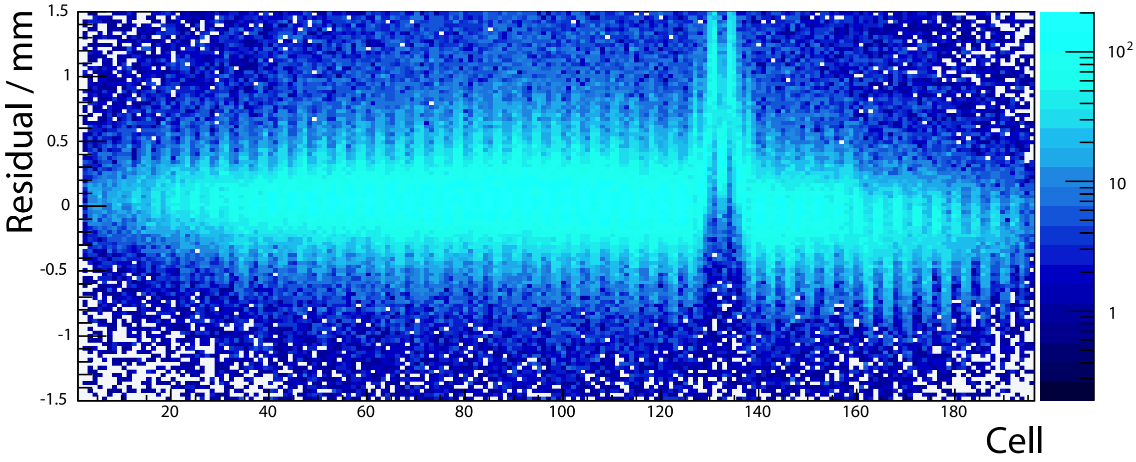

Figure 7.5: This diagram shows, in vertical direction, the residual distributions for each cell from data taken for SL 10. The regular pattern occurs because of the different RMSs depending on the layer of the cell (figure 7.4). Noticeable are the shifted peaks for cells 129 to 136.

7.4 T_0 and Drift Velocity Optimisation

7.4.1 Global Determination

Until this point it has been assumed that the time T_0, the moment the muon passed the triggers, is known. That is not completely true and the previous value around 10,260 ns from the TDC spectrum in figure 5.6 was just an estimated guess[1]. A more methodical approach is to try different values for T_0 and also for the drift velocity v_{drift}, since the gas might behave slightly differently than expected from figure 5.5. As a measure of quality for such a combination the ratio of hits with $\chi^2/\text{dof} < 1$ may be taken. Figure 7.6 is the result of such variations. The larger the bars the more events could be fitted with the demanded high quality. One can see from that diagram that for drift velocities close to the nominal value it is possible to adjust T_0 only and consider the drift velocity as constant. So here for a nominal v_{drift} of 55 μm/ns the best value for T_0 is at 10,258 ns. But in this case it seems that the drift velocity is more likely around 53 – 54 μm/ns with a T_0 of 10,264 ns and 10,261 ns respectively.

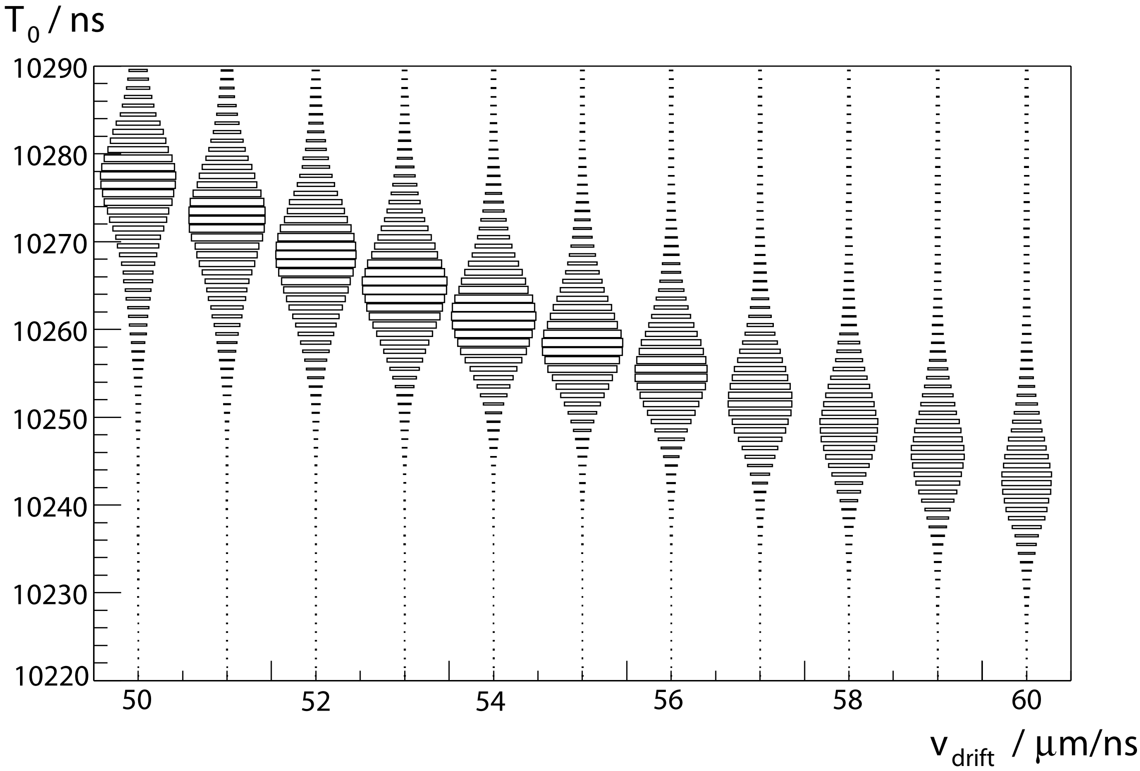

Figure 7.6: The number of entries with a $\chi^2 < 1$ as a function of the drift velocity v_{drift} and T_0.

---

[1] By "coincidence" it turns out that the guess was quite good!

7.4.2 Regarding Individual Cells

Already from the examination of the track residuals per cell some TDC channels with shifted T_0s could be observed. A close look on the edges of the corresponding TDC spectra confirmed this suspicion. But even cells that do not attract attention at once may show small time deviations due to different signal propagation and processing times, non-uniform tube illumination because of position depending trigger efficiencies and other reasons. Measuring and correcting these shifts should improve the track quality.

An ideal TDC spectrum without uncertaincies would have a sharp T_0 edge. In reality an estimated 20 ns blurr appears. In theory it is possible to correct this uncertaincy via simulations, but in practice it is a good approach to define a typical point of the edges and to find an offset for all these points to the value of T_0 that gives the best tracks [28].

A good candidate for the definition of such point of the edge would be the position with the biggest slope and to find this point one takes the derivatives of the spectra and looks for an extremum or, even better, applies a Gauss fit. This procedure usually succeeds, see [37], but due to a jitter pattern of 4 ns periodicity of the used TDCs at Aachen another approach, a linear fit, turned out to work better.

Application of Gauss Fits

From the outset it has been tried to reduce the impact of the unwanted jitter by smoothing the examined TDC spectra with a built-in function[2] of the ROOT framework. From such a processed spectrum the derivative is calculated and the negative derivative is fitted with a Gauss function within the interval where the edge of the original spectrum ranges from 10% to 90% of the peak value with the estimated noise level[3] subtracted previously.

In most cases the fit works and a sensible maximum of the Gauss function is returned, inspect figure 7.7 with a T_0 fit of the global TDC spectrum for instance. But sometimes, especially for spectra of single cells, it turns out that the peak of the derivative is not in the middle of the selected interval as the jitter deforms the flank of the TDC spectrum too much. In even worse cases the original spectrum has several peaks because of the TDC problems and a Gauss fit fails therefore, see figure 7.8.

Fitting histograms that way for each drift cell of a superlayer returns a diagram like that in figure 7.9. The error bars are the sigmas of the Gauss fits. Obviously the fit is successful in most cases, but about 10% of the trials fail. As a sign of this the error bars become larger and the mean values are exceptionally shifted. But at least the group from cell 129 to 136 with their shiftet T_0s can be identified.

---

[2] The smoothing is based upon an algorithm described in [38].

[3] The background level can be set to the average height of the TDC spectrum before the T_0 edge (higher TDC values) with some safety margin.

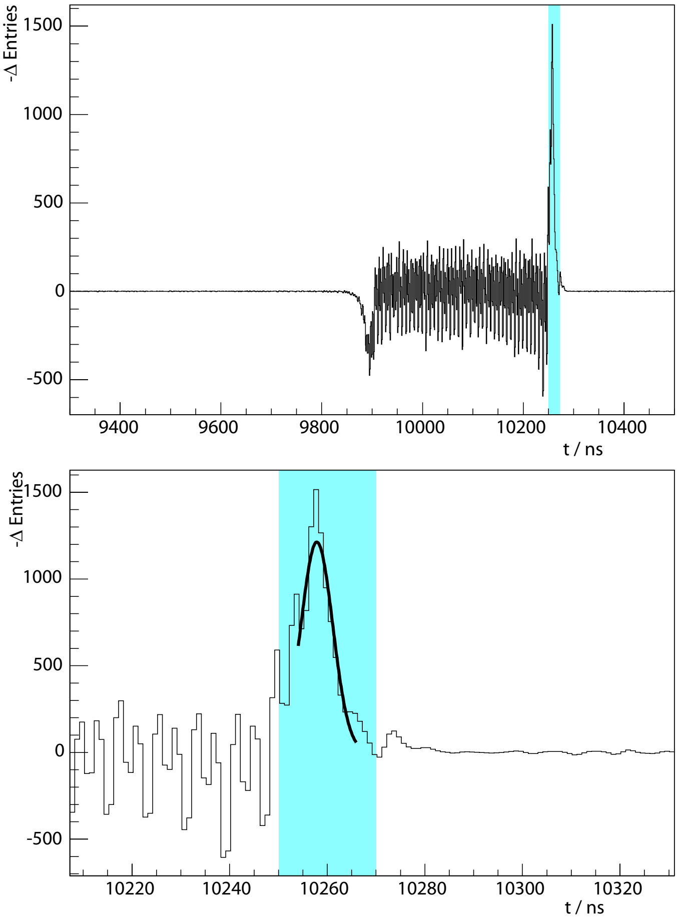

Figure 7.7: Upper diagram: the negative derivative of the global TDC spectrum. The maximum on the right at about 10,260 ns can be used for the T_0 determination in principle. Lower diagram: for the peak of the derivative a Gauss fit is possible.

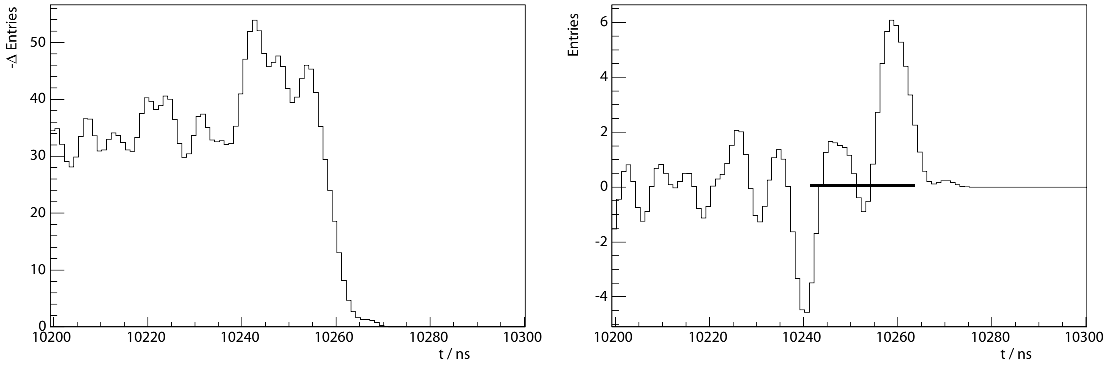

Figure 7.8: Left diagram: the T_0 edge of a cell with so much jitter that the global maximum is not part of the flank. Right diagram: the Gauss fit by ROOT of the negative derivative does not work.

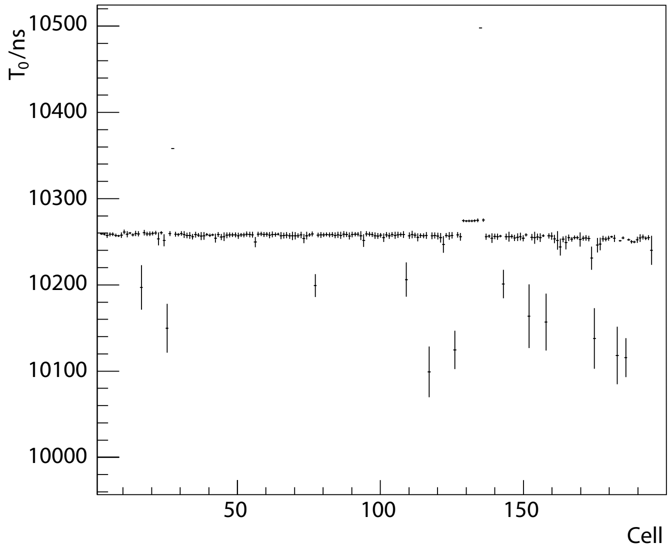

Figure 7.9: The T_0s for a complete superlayer with Gauss fits used for their determination. Even though some attempts have failed the known group of eight cells with shifted spectra can be detected.

Linear Fits

Since the deformation of the TDC spectrum edges by the jitter influences their shapes too much for Gauss fits an alternative method had to be considered. The final choice for a simple linear fit of the flank of the smoothed original TDC spectrum was made with the fitting interval given by the time bins where the number of entries reaches 20% and 80% of the maximum value with the estimated background level subtracted as before. The point where the linear fit reaches the 50% mark is regarded as the demanded time. This way even fits for heavily distorted cells, like that in figure 7.10, return at least sensible T_0 values. But the accuracy in these cases remains untested.

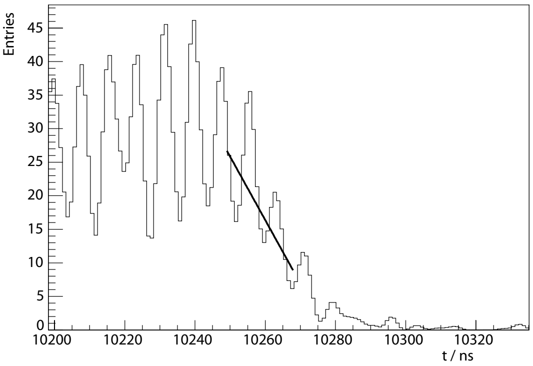

Figure 7.10: Even distorted cells with TDC edges like this one return an acceptable value for T_0 if a linear fit was performed.

To show the superiority of the the linear method compared to the original one figure

7.11 contains the T_0s measured with the linear fit for SL 7 from data taken without using the eight distorted TDC channels.[4] Anyway, the result is typical, see figure 7.11: almost for every cell, enough statistics provided, a reasonable value is received. The error bars indicate the intervals used for fitting and since these cover about 60% of the flank height they approximately correspond to the sigmas of the Gauss fits. To be on the save side the T_0 for a single cell is not taken if its uncertaincy and its error bar respectively is too large. Instead it is replaced then by the global value in this case.

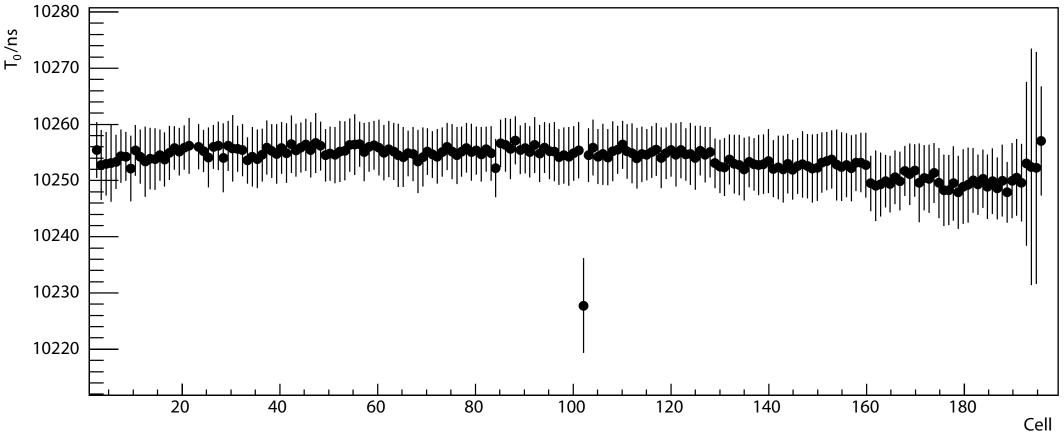

Figure 7.11: With a linear fit for almost every cell a sensible value for T_0 can be computed.

Figure 7.12 shows the correlation between T_0s for which both the linear and the Gauss fit methods worked. With the definition of the covariance [35]

$$cov_{x,y} = \langle(x-\mu_x)\rangle \cdot \langle(y-\mu_y)\rangle = \int\int(x-\mu_x)(y-\mu_y)f(x,y)dxdy \tag{7.1}$$

whereas $f(x,y)$ is the probability distribution and μ_x and μ_x are the mean values of the single distributions of x and y respectively. The correlation coefficient ρ is given by

$$\rho \equiv \rho_{x,y} = \frac{cov(x,y)}{\sigma_x \cdot \sigma_y} \tag{7.2}$$

with σ_x and σ_y being the standard deviations. ρ is a nondimensional size within the interval $-1 \leq \rho \leq 1$. If x and y are not correlated, ρ is zero. The extreme cases $\rho = \pm 1$ stand for linear dependences between the random variables.

The correlation coefficient for T_0s successfully computed with linear and Gauss fits is 0.96, hence in case both methods work they give the same results in practice, see figure 7.12.

Another test is to compare the calculated T_0 deviations ΔT_0 of the individual cells respective the global mean value with such deviations of test pulses. Test pulses are generated signals that simulate the drift tubes which are induced at the front end electronics.

---

[4] Here superlayer 7 is taken since only for this one test pulses, allowing for comparison with the calculated T_0s, have been measured at the time of the examinations in this section [30].

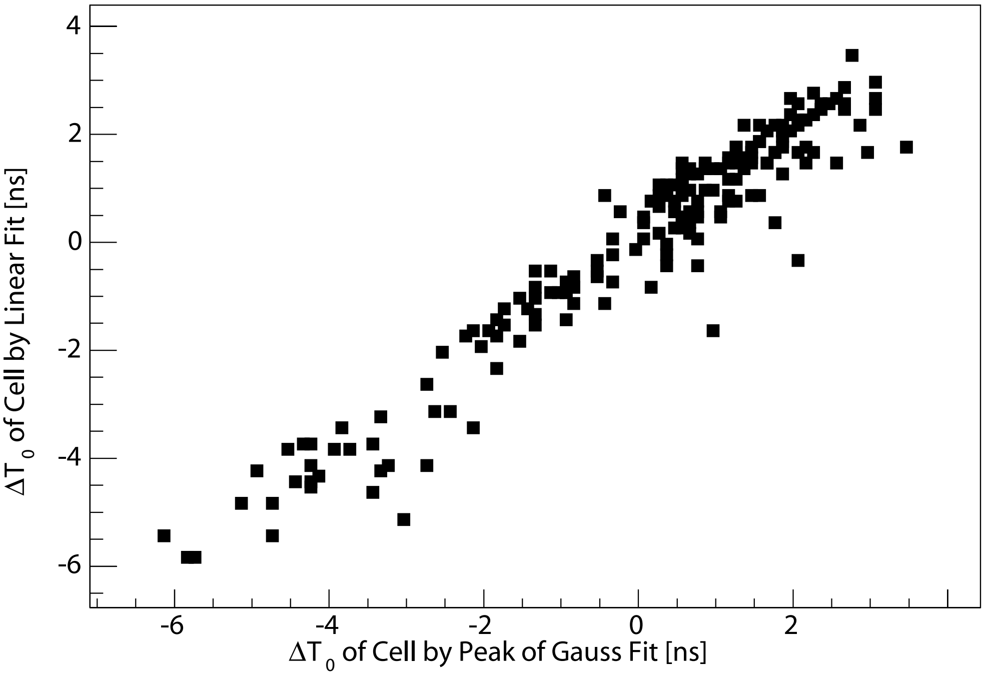

Figure 7.12: Here the correlation coefficient is 0.96 between successful linear and Gauss fits. ΔT_0 is the difference between the T_0 of the individual cell and the global mean value.

Since the times of the test pulses are well known it is possible to determine differences in the conversion and detection speed of all the read out channels [30]. Figure 7.13 shows a low correlation of $\rho = 0.61$ between the test pulse differences and the T_0 differences. This is acceptable as the drift tubes with their propagation times and different distributions of triggered muons are expected to give additional offsets. But a study whether the test-pulse information surpasses the TDC T_0s is still unavailable since the automatic test pulse acquisition has started just recently.

7.4.3 The Ideal T_0 Offset

The T_0 points obtained with the fits for each channel are of arbitrary absolute value in principle. Their relative shifts are the information used in the following. Analogous to the determination of a best global T_0 it is possible to introduce a common offset for all the cells which has to be chosen in a way that the χ^2s become of optimum quality. Plot 7.14 shows the ratio of good fits, i.e. fits that survived the prior $\chi^2/\mathrm{dof} < 10$ cut, as a function of such an offset for different drift velocities. So to replace the previous choice of a compatible global T_0 for a fixed drift velocity the suitable offset must be taken now. A linear approximation based on assumed drift velocities of 53 – 56 μm/ns gives as a rule of thumb

$$t_{\text{offset}} = 197.5 \text{ ns} - 3.5 \frac{\text{ns}^2}{\mu\text{m}} \cdot v_{\text{drift}} \tag{7.3}$$

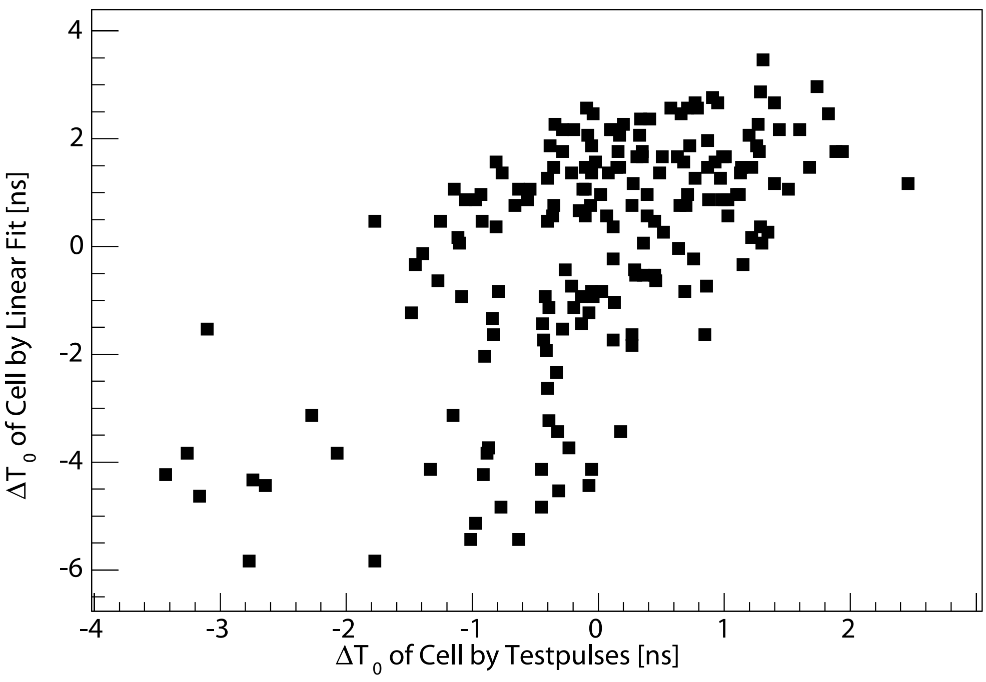

Figure 7.13: Merely 0.61 is the correlation between TDC T_0 differences and those of test pulses.

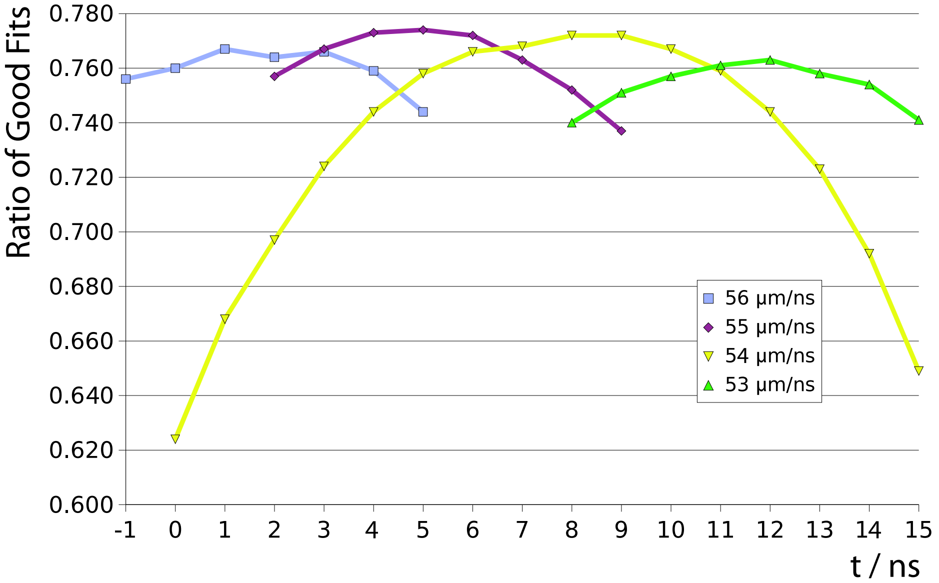

Figure 7.14: The ratio of good fits ($\chi^2/\text{dof} < 10$) as a function of the chosen time offset for some assumed drift velocities.

Layer	RMSs of the track residuals	
	before T_0 correction	after T_0 correction
1	189 μm	185 μm
2	316 μm	300 μm
3	320 μm	303 μm
4	187 μm	182 μm

Table 7.1: Width of the track residual distributions of SL 10, containing 8 channels with strongly shifted T_0s, before and after the T_0 correction (χ^2/dof < 10, $|\alpha| < 30°$).

7.4.4 Improvement of the Track Residuals

The application of the detected T_0s should increase the track quality and reduce the distances between a muon track and the isochrones of the hit cells. A lower RMS of the residual distributions for each layer is expected. Computation shows, see table 7.1, that this really happens, especially for layers 2 and 3 where the effect is a reduction of about five percent.

7.5 Calibration via the TDC Spectrum

The assumption of a constant drift velocity shall be abandoned at this point. In particular close to the anode wire the electric field strength increases so much that a correction should be applied by extracting an *r*-*t* relation from the global TDC spectrum to be used for calibration.

7.5.1 The Calibration Method

The procedure described here assumes a uniform illumination with triggered cosmic muons of the drift tubes, thus

$$C := \frac{dn}{dr} = const. \tag{7.4}$$

Except the border area next to the cathodes, where slightly inclined muons may leave the cell in spite of an angle cut trough the aluminium beams and hence not produce enough charge carriers for a signal detection, this should not cause a problem. The *r*-*t* relation is determined by integrating the global drift time spectrum $\frac{dn}{dt}$ using the global T_0:

$$\int_{T_0}^{t} \frac{dn}{dt'} dt' = \int_{T_0}^{t} C \frac{dr}{dt'} dt' = C \cdot r(t) \tag{7.5}$$

So by integrating – respective summing – the distribution of the number of hits as a function of the drift time the *r*-*t* relation is received after normalisation. As the used

TDC spectrum must contain hits from cosmic muons only, without noise or afterpulse hits, the calibration procedure is applied to a spectrum with hits from successful fits with the usual cuts ($\chi^2/\text{dof} < 10$, $|\alpha| < 30°$) using a constant drift velocity and a common T_0 for all cells. The typical results are shown in figure 7.15. Close to the anode wire at $r = 0$ the drift velocity peaks because of the high field strength. Apart from that the drift velocity is about constant[5] along the horizontal position r with a small rise towards the cathodes. It is easy to recognise the typical structure of the TDC spectrum in the v_{drift}-r relation.

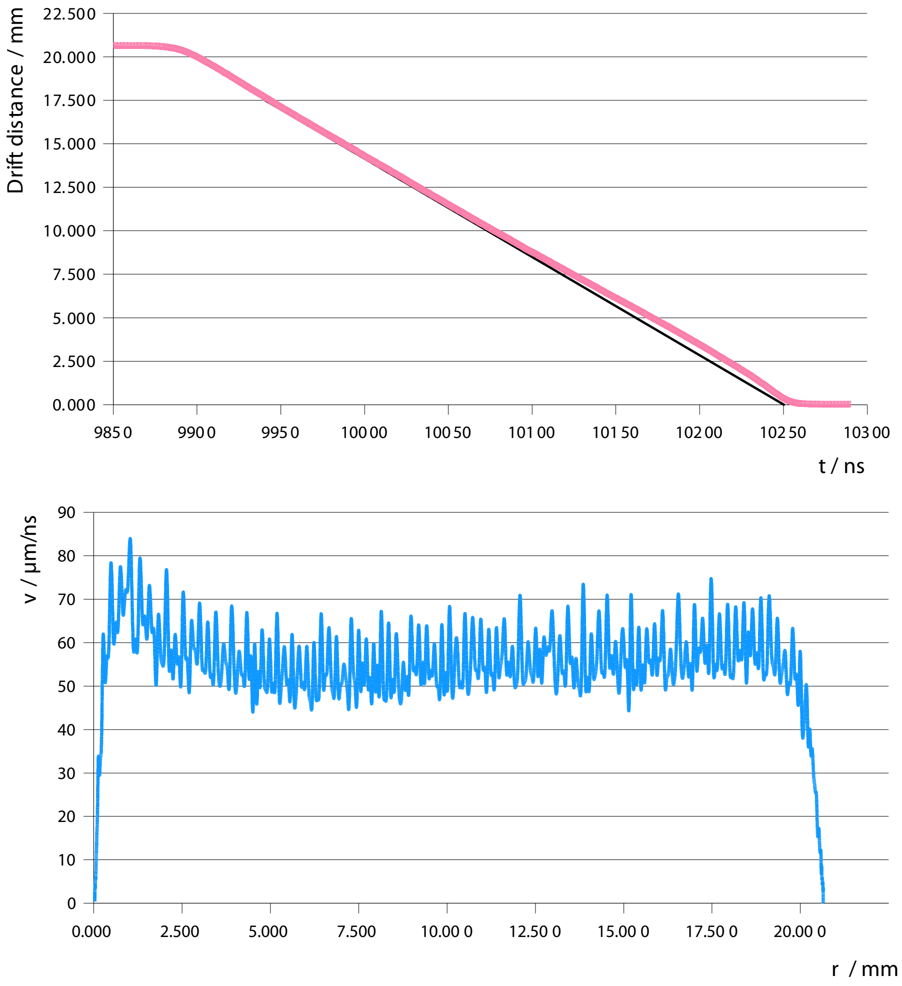

Figure 7.15: Top: The r-t relation is mostly linear but flattening for large drift distances and with a bulge at times for muons close to the anode wire. Bottom: The v_{drift}-r relation shows the increase of the field strength around the anode wire.

---

[5] The jitter is mostly due to the already known TDC problem.

7.5.2 Application of the Obtained Relation

In the following the r-t relation as calculated on the basis of the global TDC spectrum is used for every cell. The already measured T_0 variations are respected by shifting the calibration function accordingly for each cell. This procedure replaces[6] the previous method from section 7.4.3. A first result is given by the histograms in figure 7.16 which display the frequency of the measured drift distances before and after the calibration procedure. In general the contour gets more box shaped as expected since a uniform muon distribution has been demanded. Especially the peak for short drift distances becomes obviously minor.

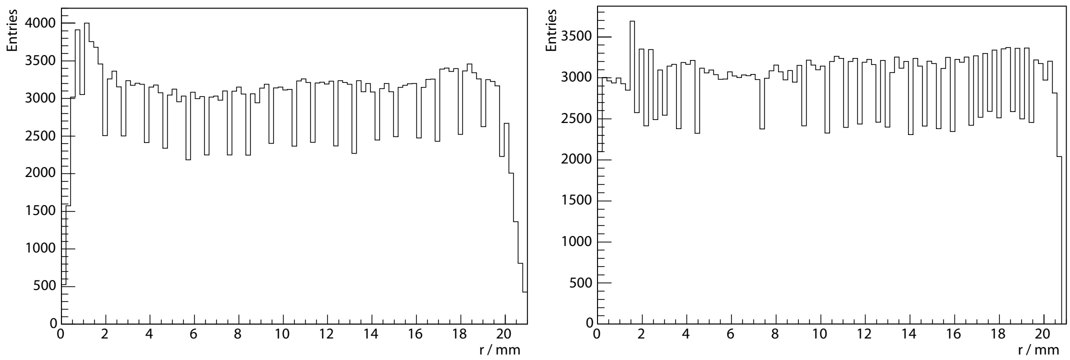

Figure 7.16: Left: the frequency of the measured drift times before the calibration is equivalent to the TDC spectrum. Right: after the calibration the distribution becomes more box shaped. Both distributions inherit the original TDC jitter.

Another check is to inspect the mean values of the residual distributions as a function of the points where the muon tracks traversed the horizontal plane inside the cells at the height of the wire. It is visible from figure 7.17 that after the calibration in particular near the anode wire the track residuals peak closer to zero which means that better fits are possible. The slope of the residuals for drift distances close to the I-beams is due to inclined tracks which appear to be slightly outside the geometrical cell limits at the hight of the wire. The widths of the residual distributions do not experience a significant change, see table 7.2.

The residual distributions within the cells also show a small edge at the transition region around 3 – 4 mm where the cylindric isochrones start flattening. The still occuring discrepancy between the mean values and zero could be reduced in principle by using this measurement and implementing an iterative correction [28]. But this remains a suggestion for a future improvement.

---

[6] The track fitting program still contains the option to use a constant drift velocity in case the calibration as described does not work, e.g. at non-uniform illuminations.

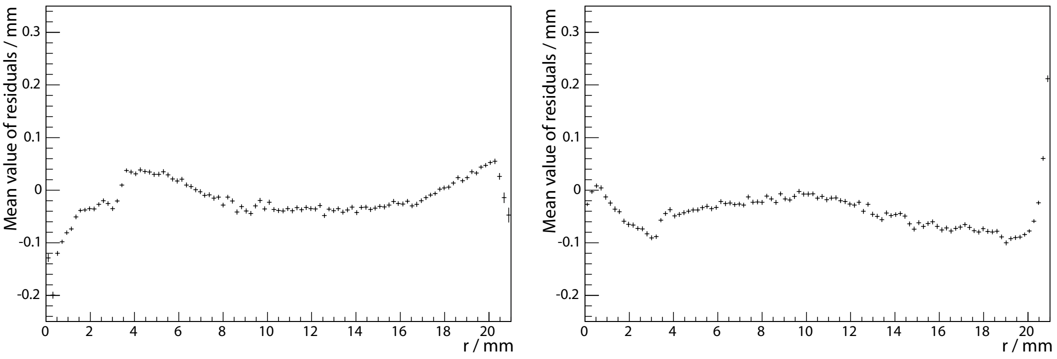

Figure 7.17: Left: the mean value of the residual distributions as a function of the horizontal distance within the cells. Right: after the calibration the residuals peak closer to zero in general.

Layer	RMSs of the track residuals	
	before calibration	after calibration
1	185 μm	184 μm
2	300 μm	298 μm
3	303 μm	302 μm
4	182 μm	181 μm

Table 7.2: Width of the track residual distributions of SL 10 before and after the calibration.

7.6 Wire Positions

Part of the quality control is the measurement of the wire positions during superlayer assembly. This is done optically with a CCD camera (see figure 7.18) mounted on a coordinatograph [10]. The wire positions are measured for each cell both at the high voltage and front end electronics sides of an open layer after the wire integration and before the closing aluminium plate is glued on top. The absolute positions are received by comparisons with external reference points on the assembly table. The measured points are recorded and become part of the quality database.

In general, wires that do not fulfil the requirement to be placed at the nominal position with a precision of 100 μm are replaced during assembly, but since the calibration of the wire position meter is a very delicate procedure it would be preferable to have an independent verification.

So the idea is to apply the measured wire positions instead of the nominal ones during track reconstruction. In case the position determination can be trusted this should lead to better tracks, especially if the deviations are quite large, and so again to narrower residual distributions. For simplification it is assumed that both ends of the wire receive the same shift, i.e. no angular tilt is assumed, and hence the average value of both measured points of a wire is taken.

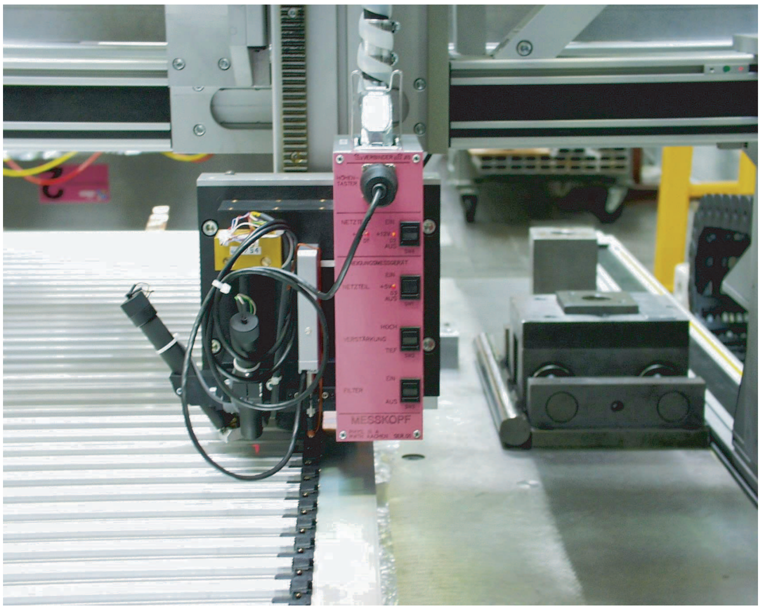

Figure 7.18: A picture of the measuring head of the coordinatograph that contains the CCD camera. It can be moved with high position to the anode wires inside the open drift tubes layer to determine their positions [10].

Superlayer 66 is an example where wire displacements above the aimed 100 μm have been measured for the bottom layer and shifts close to 100 μm for layer 2. Hence it is a suitable object to test the effect of wire position consideration. Fitting tracks with the T_0 correction, the calibration and once with and once without respecting the wire positions shows no significant difference for some layers which are regarded as "healthy". Small but still noticeable differences occur for layers with shifted wires, see table 7.3. The correction yields RMSs for the residuals of the "bad" layers of about the same value as computed for the normal ones, a first hint that the measured wire positions are worth to be respected in such cases to get the maximum track resolution.

Layer	RMSs of the track residuals		average wire distance from nominal value
	without wirepositions	with wirepositions	
1	186 μm	186 μm	41 μm
2	317 μm	312 μm	88 μm
3	311 μm	312 μm	-27 μm
4	190 μm	187 μm	142 μm

Table 7.3: Widths of the track residual distributions with a precision of about 1 μm for SL 66 before and after wire position corrections. Applied are the usual cuts ($\chi^2/\mathrm{dof} < 10$, $|\alpha| < 30°$). The right column shows the mean value of the wire deviations from the nominal positions as measured accurate to some 10 μm with the CCD camera.

Chapter 8

Determination of Detector Quality Parameters

The following parameters are used to rate the quality of a produced superlayer and most of them are required to be calculated for the quality control of the CMS muon group.

8.1 Noise Rate

Noise hits occur from time to time apart from the normal hits from cosmic muons. This noise may be caused by random currents in the anode wires exceeding the discriminator thresholds or simply by the read out electronics. As already explained the track reconstruction tries to filter out these noise hits. But it is possible that a noise hit masks a real hit as the discriminators only detect the first rise of the signal above the threshold. Following maxima are not recognised, see the sketch in figure 8.1. Only after the input current drops below the critical amplitude following anode wire pulse are considered. Pulse lengths t_{pulse} are typically 230 ns [28].

This way a noise hit may hide a real hit within its "shadow". The visible result is either a time shift of the muon pulse which inevitably causes a loss of track resolution or a reduction of the cell efficiency in case the masking noise hit occured before T_0. The maximum approved noise rate of 1 kHz per cell yields a masking probability p_{mask} of 0.02% according to, see [28]:

$$p_{\text{mask}} = 1 - \exp(-R t_{\text{pulse}}) \tag{8.1}$$

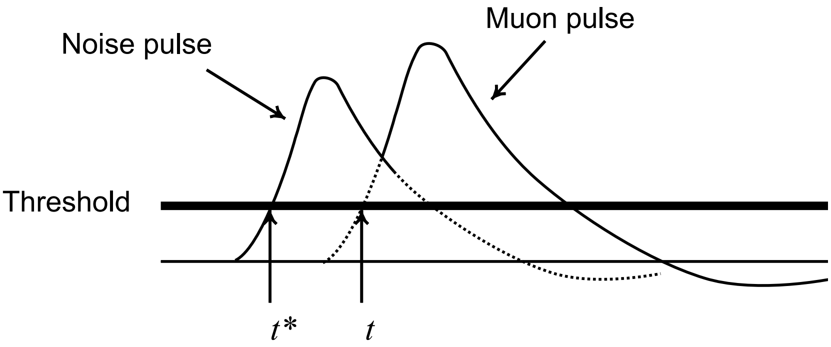

Figure 8.1: A noise hit masks a muon pulse. As the noise signal does not fall below the threshold amplitude before the arising muon pulse the latter is not registered. Its time t seems to be shifted to $t^* < t$ [28].

8.1.1 Noise Measurement

Actually the measured noise is a matter of definition. For instance afterpulses may be counted or not, potential electronic cross talk from one channel that contains a real muon hit to another cell may be treated as noise and similar issues. But here for simplicity all hits before T_0, with some safety margin, within the complete recorded drift time window of 65,536 ns are regarded as caused by noise. The actual rate is given by the number of hits within this interval divided by its time length. Of course the number of events that have been used to fill the TDC spectrum has to be respected for the correct normalisation. Typical results are noise rates around $30 - 40$ Hz per cell (figure 8.2) which corresponds to $0.03 - 0.04$ Hz/cm^2 for the layer surface.

Since the ring buffers of the used TDCs can only store up to 16 hits per cell the highest possible noise rate is about some hundred kHz, depending on the chosen interval length. But buffer overflows already appear for lower noise rates, as figure 8.3 shows. The symptom is a pretended decrease of the noise hits towards early times, i.e. large TDC values. This happens as the oldest drift times are the first ones that are thrown away. So the measured noise rates have to be considered as a lower limit, especially for rates up from some 10 kHz.

8.2 Afterpulse Probability

Afterpulses are additional hits in cells with muon tracks or noise hits due to emitted photons during gas gain which could knock out electrons from a drift cell wall. Thus the following new charge carriers should reach the anode wire within the maximum drift time. With that understanding a sensible afterpulse signature is a second hit following a first one lying within the TDC window. The time difference must correspond to a drift distance

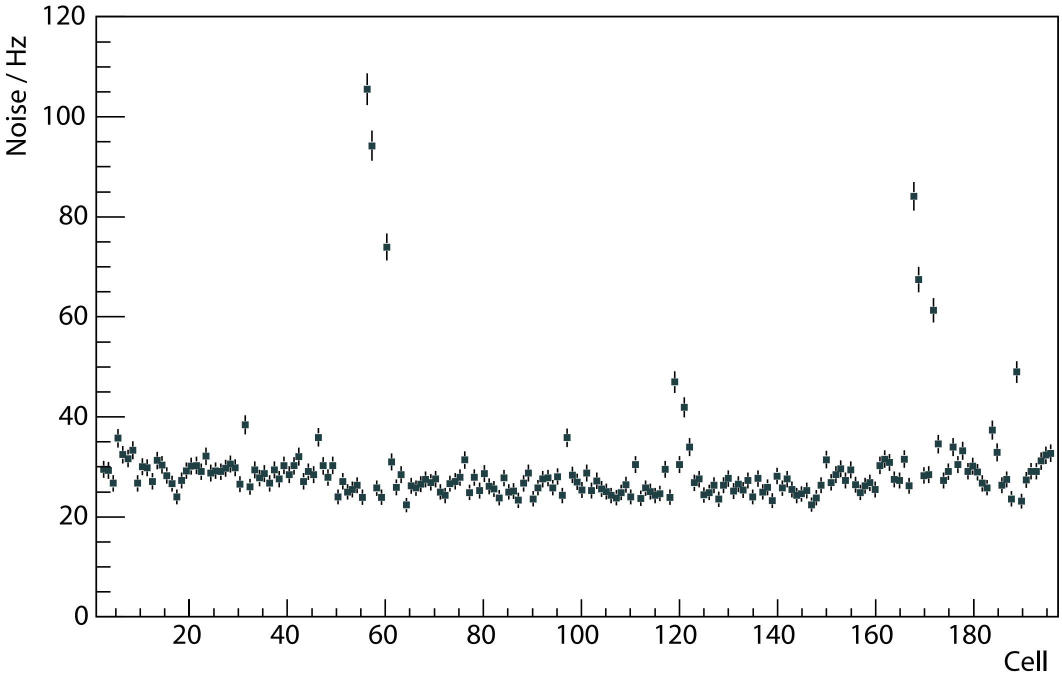

Figure 8.2: The noise per cell for superlayer 66. The error bars represent the statistical uncertaincy given by the normalised square root of the number of counted hits.

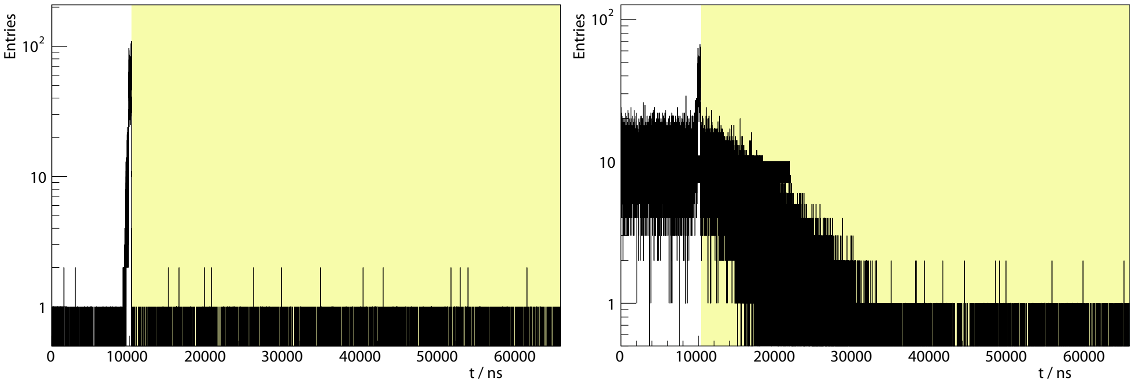

Figure 8.3: Shaded is the region of the complete TDC spectrum where all hits are regarded as noise. The usual drift time region appears as a peak around 10,000 ns. The left spectrum shows a cell with a normal noise rate, the right one has a noise rate of some 10 kHz which lets the spectrum drop as the TDC ring buffers can not store more than 16 hits.

within the cell boundaries and hence not be longer than the maximum possible drift time.

Afterpulses are unwanted since they may mask real hits, like noise hits, and since they yield more permutations to be considered during track reconstruction. In the worst case afterpulses cause afterpulses themselves.

The afterpulse probability is defined as the quotient of the number of such afterpulse hits divided by the total number of sensible drift times [39]. This way some normal noise hits may seem like afterpulses in case they follow soon after a real hit, but for usual noise frequencies of $30 - 40$ Hz per cell this effect is negligible. Typical frequencies for the measured probabilities are given in table 8.1. Of course parameters like the drift gas composition affect the result but are not subject of this thesis and hence not examined systematically here.

Afterpulse probability	Number of cells
0.07	2
0.08	33
0.09	84
0.10	53
0.11	18
0.12	4
0.13	1

Table 8.1: Frequency of afterpulse probabilities for SL 66. Here the average is about 0.09.

8.3 Efficiencies

From time to time a muon may happen to cross a drift tube without being recognised (figure 8.4). For example not enough charge to exceed the discriminator threshold may be produced during the gas ionisation and amplification process. This is especially likely to occur for muons leaving the drift gas volume through one of the aluminium beams yielding a shorter trace within the cell or for tracks perpendicular to the drift cell in all projections[1] as the track length in gas gets minimal.

8.3.1 Used Definitions

There are several ways to define whether a cell has been blind for a track or not. For instance it is possible to demand that the track residual of this cell does not exceed a certain distance. But here the definition is more tolerant as a crossed cell only needs to see any hit within the drift time window to be regarded as sensitive. A cell not yielding a

---

[1] A track may seem to traverse a superlayer with no inclination but in reality it has a slope in the projection that can not be seen by a single superlayer.

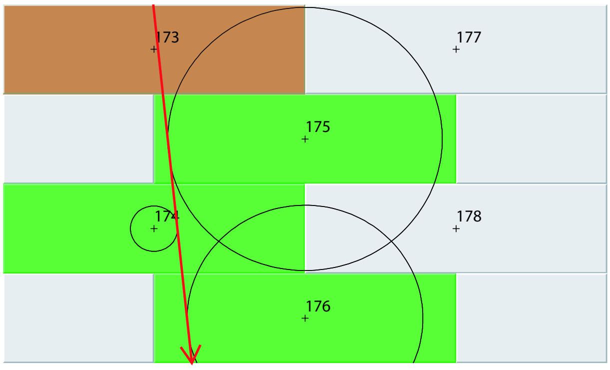

Figure 8.4: The marked cell in the top layer did not recognise the traversing muon which therefore shall be considered as inefficient in this event.

signal is taken as blind just in case a muon passed the drift cell at the height of the anode wire, see figure 8.5. Thus touched corners are not demanded to lead to a signal. On the other side a muon crossing a cell mainly inside its aluminium beam part, hence unable to fire this cell, gives inefficiencies as the whole cell width of 42 mm is respected. This geometrical effect yields inherent inefficiencies in the following examinations.

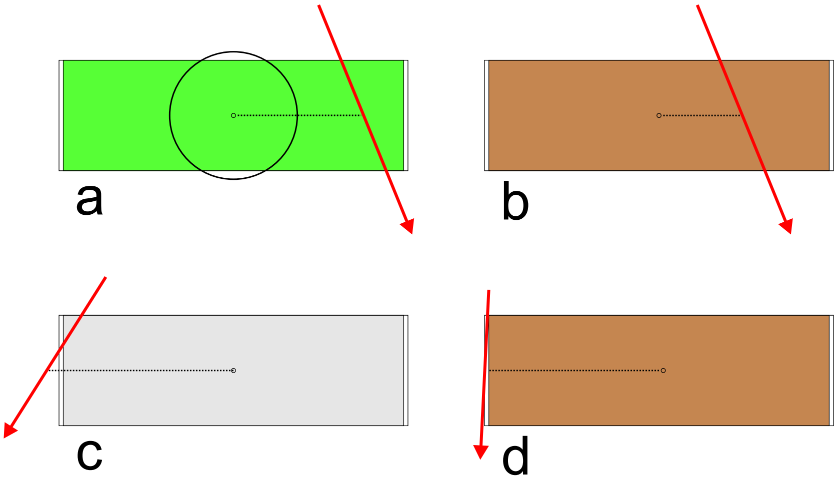

Figure 8.5: Examples for the used efficiency definition: a) Sensitive cell, the track caused a hit. b) Blind cell, the wire did not detect a hit. c) Cell not regarded, as the track lies outside the cell limits at the hight of the wire. d) Cell is considered as blind even though the track lies inside an aluminium beam.

8.3.2 Computation

With this premises the efficiency is defined as the number of seen hits divided by the number of expected hits, i.e. the seen hits plus the missed hits. So during track computation two histograms have to be filled and at the end, when the required information, received from a sufficient number of reconstructed tracks, is complete, the efficiencies can be computed per bin.

Reference Tracks

Another problem is that for the examined cell an external track determination is necessary. That means that the track fit should use the three remaining layers only which unfortunately does not always lead to unambiguous tracks. In general three possibilities plus symmetric ones have to be sorted out since in these cases the reference from three layers is not reliable, see figure 8.6.

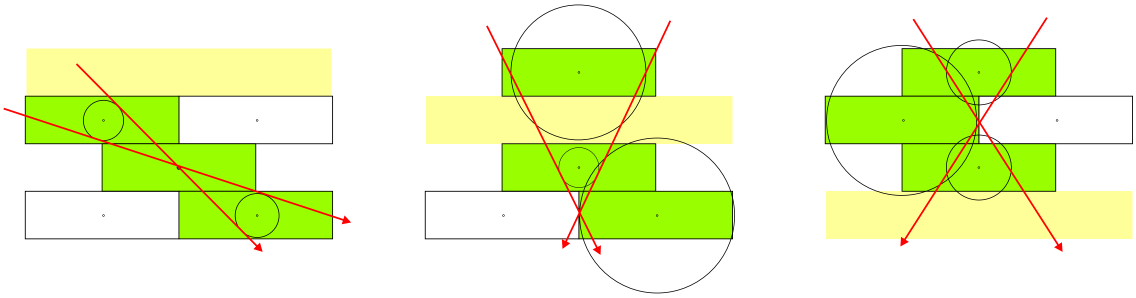

Figure 8.6: In these cases a fit with only three layers, the excluded one is marked in yellow, can not find the real reference track and the algorithm returns one of the two possibilities by random.

Now there are two possibilities. Either to perform a four layer fit if possible and a three layer fit otherwise with the additional cell resolving most of the ambiguities or to cut away the critical cases explicitly. The left event in figure 8.6 is easily sorted out by an angle cut of less than 58° since the stronger inclined track is incompatible with the trigger acceptance due to the test stand geometry. The more perpendicular result can be kept. In the two other cases the problem can be avoided by demanding a minimum track distance, 1.5 mm as the default value, from the aluminium beams for the cells two layers apart from the considered one.

The software still allows both versions since the three layer fits are required four times plus a four layer fit yielding the best track for other examinations. The option with the four layer fit only is about four times faster but contains an intrinsic systematic inaccuracy. But in practice the latter version shows, at superlayer 66 for instance, only about 0.5% to 1% less efficiency. Thus it depends on the required precision for the examination which version to take. One should be careful since the implemented three layer fit prefers to cut events close to the beams of the examined cells as perpendicular muons are the most frequent ones. These are just the events where most of the inefficiencies are expected to occur. Therefore in this thesis the standard is the four layer method.

Computation from Two Basic Histograms

Calculating efficiencies and their uncertaincies requires two fundamental histograms. One contains the number of hits whereas the cell was sensitive and detected the muon and the other histogram includes the number of missed hits. These histograms can hold these information sorted by cell number, track inclination or other parameters on which the efficiency might depend on. Here for example each bin represents a distance from the anode wire inside the drift cells and every track fit gives an entry for each affected cell in one of the two histograms in figure 8.7. It has been integrated over all superlayer cells for a global analysis.

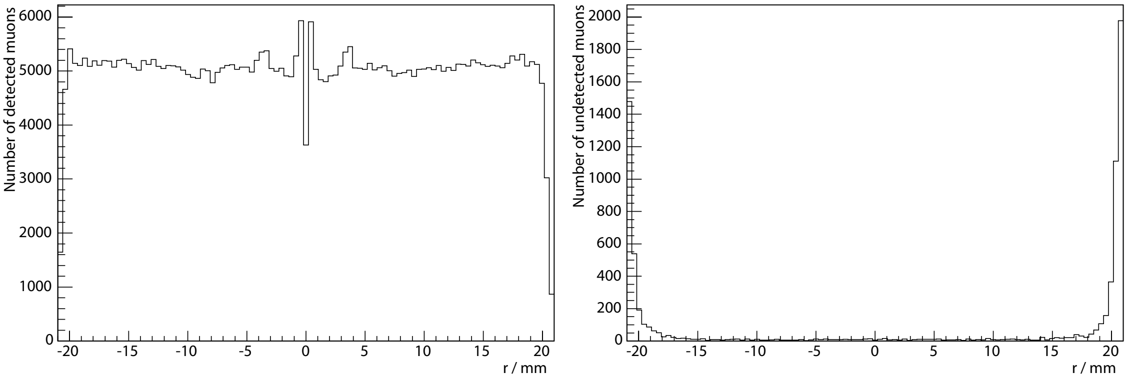

Figure 8.7: These two histograms are used to calculate the efficiency as a function of the horizontal track distance from the anode wires inside the drift cells. The left diagram contains the cell penetrations where a hit was recognised and the right one the distances that should have been detected in case the cell was sensitive.

The efficiency ϵ_i for bin i is calculated according to

$$\epsilon_i = \frac{n_{s,i}}{N_i} \qquad \text{with} \qquad N_i = n_{s,i} + n_{b,i} \tag{8.2}$$

with $n_{s,i}$ being the number of hits where the cell was sensitive and $n_{b,i}$ the number of events where the cell was blind and missed the muon. Since the distribution is binomial the uncertaincy $\Delta\epsilon_i$ is given by, see [35]:

$$\Delta\epsilon_i = \frac{1}{N_i}\sqrt{N_i\epsilon_i(1-\epsilon_i)} \tag{8.3}$$

Computation for every bin yields figure 8.8. Inside the cell the efficiency is typically about 99.8% dropping towards the aluminium beams as some muon tracks leave the cell volume through an I-beam with the distance in gas too short to produce enough charge for detection.

8.3.3 Efficiency Analyses

Calculating the detection efficiency of a cell as a function of different track parameters allows for learning more about the superlayer properties.

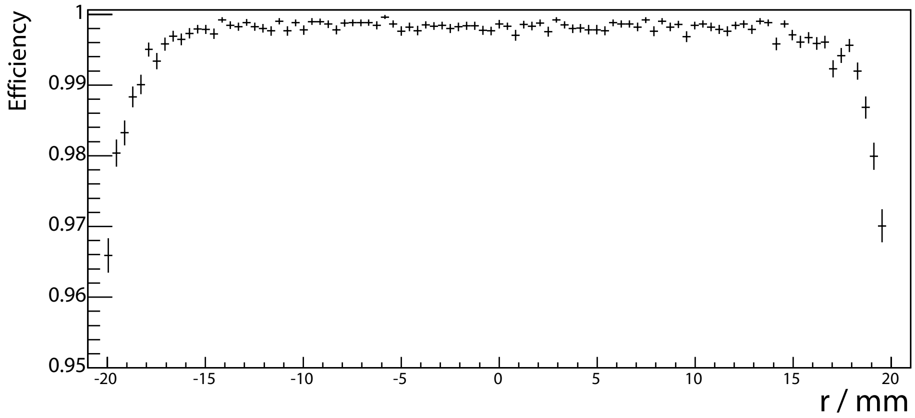

Figure 8.8: The efficiency against the horizontal distance to the anode wires within the drift cells. The drop towards the cell borders is of geometrical nature. Applied cuts: $\chi^2/\mathrm{dof} < 10$, $|\alpha| < 30°$.

Cell Number

It is useful to examine the efficiency cell by cell to identify dead cells e.g. due to anode wire failures or inefficiencies expected as a consequence of cathode or strip malfunctions [24]. Figure 8.9 shows the result of such a computation. The slight drop towards the edges of the superlayer happens because of the geometric acceptance of the trigger. Detected muon tracks in these regions are mainly perpendicular to the superlayer plane and so they traverse a relatively short distance within the gas volume. But for all cells the largest contribution to the inefficiencies is given by the dead area of the aluminium beams.

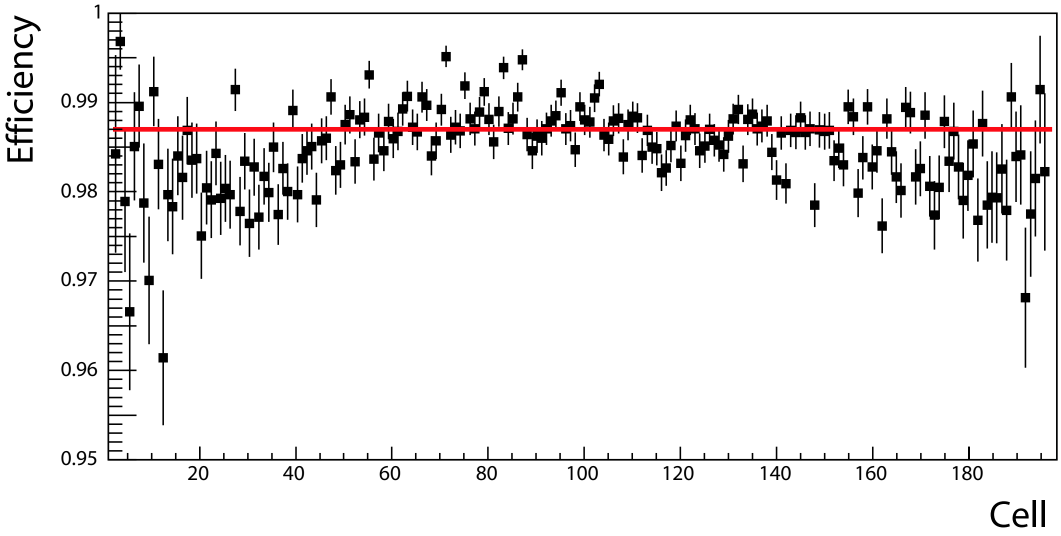

Figure 8.9: The efficiency as a function of the cell number. The cells of the examined superlayer 66 have an average efficiency of 98.7 %.

Track Position Within the Drift Cell

The statement that the main contributions to the inefficiencies are due to the I-beams has already been circumstantiated by the recent example from figure 8.8. The efficiency over most of the cell width is typically about 99.8 % with the exception of cells having an electrode problem. Efficiency computation as a function of the horizontal distance from the anode wire for a single cell with an unconnected cathode gives a distribution like that in figure 8.10. The efficiency close to the affected border decreases observably.

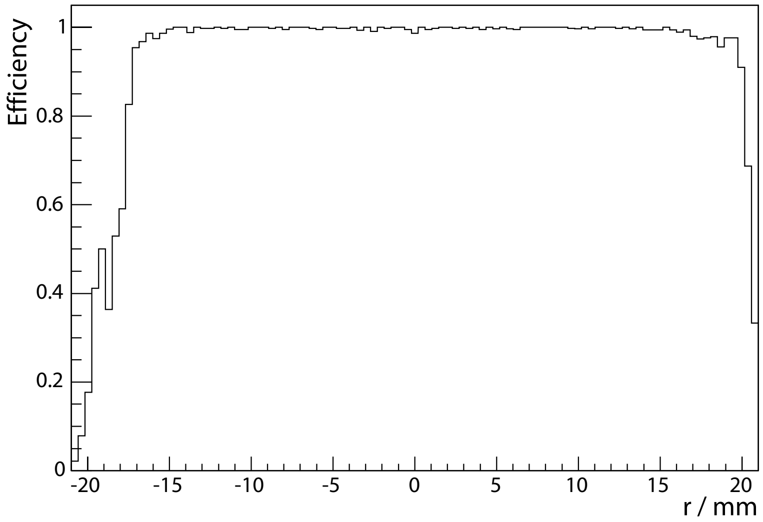

Figure 8.10: Spatial efficiency distribution for a single cell (136 in SL 101) with r being the horizontal distance from the anode wire. Visible is a decline due to an unconnected cathode on the left.

Track Inclination

As it is expected that the efficiency drops for angles close to 0° it is worth to perform an examination regarding that track parameter. Indeed figure 8.11 confirmes the assumed dependency but with a slight rise for almost vertical tracks. This happens as these candidates have a higher probability to cross two of the four layers inside the aluminium beams and hence produce less than the three hits required for track reconstruction. So the larger inefficiencies for these tracks close to the beams are disregarded.

Track Inclination and Position Inside the Drift Cell

To prove that the last observation really occurs due to the aluminium beams the efficiency can be sorted by track angle and distance to the closest anode wire at the same time (figure 8.12). Already the occupancy for the recognised hits and the diagram with the

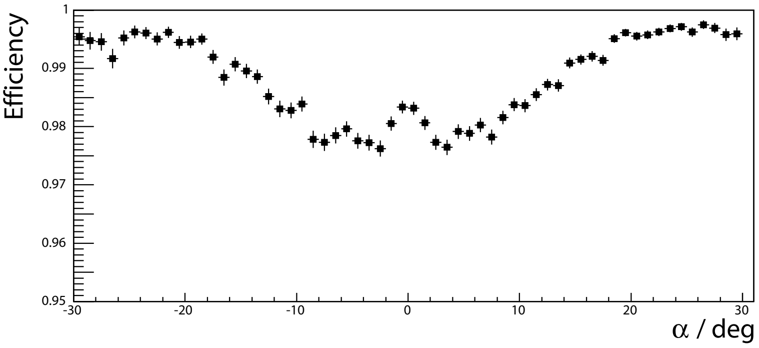

Figure 8.11: The efficiency as a function of the track angle. The efficiency decreases as expected for upright tracks with a small rise in the middle due to aluminium beam shadows.

number of missed hits show structures which correspond to tracks that traverse more than one beam. Visible for vertical muons in the distribution containing the missed hits is the gap at the cell borders responsible for the missed inefficiencies.

Figure 8.13 shows, as a summary, the efficiency decrease towards the cell edges since in these regions muons may escape the cell volume through the aluminium beams. The strongest effect occurs for about upright tracks as their distance in gas is short anyway and in particular as they traverse long distances inside the aluminium if they hit an I-beam.

8.4 Track Residuals and Resolution

In section 7.3 the track residuals have already been defined as the signed distances between the reconstructed muon tracks and the isochrones. The widths of residual distributions are layer dependent since there are no external track references.

Superlayers 10 and 66 are examined exemplarily as their properties are already familiar from the previous sections. As a reminder: the first one contains a block of eight channels with shifted TDC values and the second one possesses noticeable wire position offsets. The following analyses apply all the introduced corretions and the selected events fulfil $\chi^2/\mathrm{dof} < 10$, $|\alpha| < 30°$.

8.4.1 Cell Resolution

Since the number of four layers is too small to neglect the influence of individual cells on the track the resolution of a cell can not be approximated by its track residuals [28]. By assuming an average width of the residual distributions $\langle\sigma_R\rangle$ without distinguishing the layers one would get the following as the ratio between σ_R and the real spatial resolution σ_x: with n measured points $(x_i|y_i)$, $i = 1 \ldots n$ and $x(y) = ay + b$ as the linear smoothing

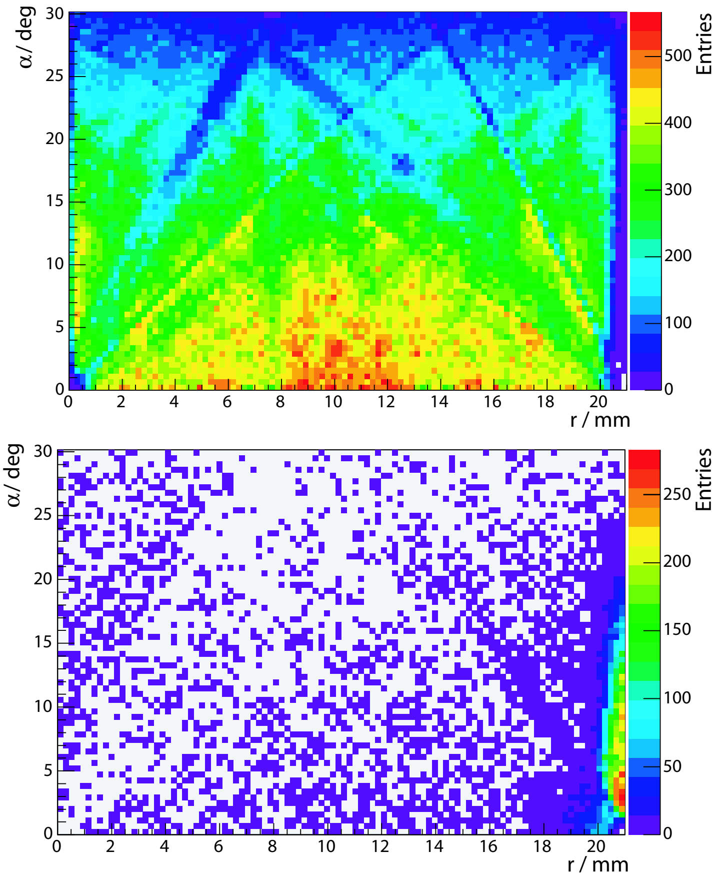

Figure 8.12: The number of seen tracks (top) and missed tracks (bottom) depending on the absolute values of track angle and wire distance. The efficiency distribution in figure 8.13 is computed from these two inputs. The visible structures appear due to aluminium beam shadows as three sensitive layers are required to find a track.

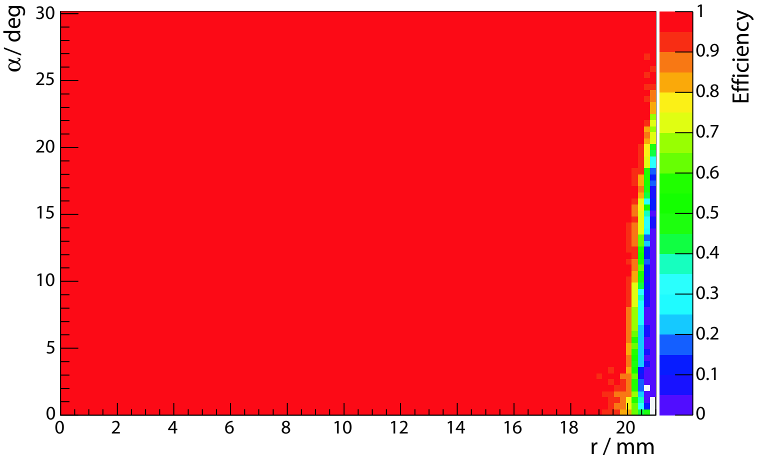

Figure 8.13: The efficiency as a function of the absolute value of both track angle and horizontal wire distance. Upright tracks in the aluminium beam regions yield strong inefficiencies.

function the definition of the χ^2 distribution [35] yields

$$\langle\chi^2\rangle = \left\langle \sum_{i=1}^{n} \left(\frac{ay_i + b - x_i}{\sigma_x} \right)^2 \right\rangle = n \left(\frac{\sigma_R}{\sigma_x} \right) \tag{8.4}$$

And since

$$\langle\chi^2\rangle = N_{dof} = n - 2 \tag{8.5}$$

the spatial resolution is given by

$$\sigma_x = \sigma_R \sqrt{\frac{n}{n-2}} \tag{8.6}$$

Averaging over all four layers of SL 66 (table 7.3) returns $\sigma_R = 249$ μm and in consequence, since only events with $n = 4$ hits each in a separate layer have been taken, the spatial resolution σ_x would be 249 $\mu\text{m} \cdot \sqrt{2} = 352$ μm according to equation (8.6) if the track residual distributions of all layers were the same.

But obviously, remember figure 7.4, the outer layers have narrower distributions than the inner ones and so for an exact computation every layer i gets its individual factor f_i so that

$$\sigma_x = f_i \cdot \sigma_{R,i} \tag{8.7}$$

Now for tracks with four hit cells uniformly distributed over all four layers the factors for the outer layers $i = 1, 4$ are

$$f_{1,4} = \sqrt{\frac{10}{3}} \tag{8.8}$$

and for the inner layers $i = 2, 3$

$$f_{2,3} = \sqrt{\frac{10}{7}} \tag{8.9}$$

must be used. For the derivation of that result, respecting the lever arms of the layers, see [28]. Application of the factors leads to the middle colums in table 8.2. The origin of the remaining resolution differences of the inner and outer layers in spite of their individual correction factors is not understood.

8.4.2 Test Stand Uncertaincy Corrections

The σ_x as the cell resolution for superlayers measured in the test stand at Aachen still contains the trigger common stop uncertaincy of about 2 ns [40] and the unknown propagation time t along the anode wire as a superlayer only allows 2D track reconstructions. This projection contributes a σ_t of estimated[2] 3 ns. In addition there is an unknown influence of factors like the TDC jitter. Correction of the first two effects according to

$$\sigma_x'^2 = \sigma_x^2 - (2\text{ ns} \cdot v_{\text{drift}})^2 - (3\text{ ns} \cdot v_{\text{drift}})^2 \tag{8.10}$$

with $v_{\text{drift}} = 55$ μm/ns yields the right columns for the superlayers in table 8.2. These values are still beyond the required precision of 250 μm.

---

[2] A flat muon distribution along the wire and a propagation velocity of 2/3 c are assumed.

Layer	SL 10			SL 66		
	σ_R	σ_x	σ'_x	σ_R	σ_x	σ'_x
1	170 μm	310 μm	238 μm	186 μm	340 μm	276 μm
2	284 μm	339 μm	275 μm	312 μm	373 μm	316 μm
3	289 μm	345 μm	282 μm	312 μm	373 μm	316 μm
4	168 μm	307 μm	234 μm	187 μm	341 μm	277 μm

Table 8.2: Resolution depending on layer for SLs 10 & 66. The spatial resolution σ_x follows from the width of the track residual σ_R, the resolution σ'_x corrects some estimated uncertaincies of the test stand.

It is possible to estimate the total test stand uncertaincy from the width of the T_0 edges of the TDC spectra. Fitting their flanks returns a σ_{T_0} of about 5 ns, see the error bars in figure 7.11 which correspond to the 1σ interval of a Gauss fit. Quadratic subtraction of that value again with $v_{\text{drift}} = 55$ μm/ns yields σ''_x, see table 8.3. The results can be regarded as the obtainable resolution without the test stand restrictions. The reason for the different values for superlayers 10 and 66 is unknown. But altogether the required cell resolution of ≤ 250 μm at CMS is achieved.

Layer	SL 10		SL 66	
	σ_x	σ''_x	σ_x	σ''_x
1	310 μm	143 μm	340 μm	200 μm
2	339 μm	198 μm	373 μm	252 μm
3	345 μm	208 μm	373 μm	252 μm
4	307 μm	136 μm	341 μm	202 μm

Table 8.3: Resolution for each layer before (σ_x) and after (σ''_x) the total T_0 uncertaincy correction.

8.5 Meantimes

The so called *meantime* is a geometrical size whose calculation allows several conclusions regarding the precision of the tested superlayer.

8.5.1 Meantime Definition

The meantime is defined for three consecutive layers, see figure 8.14, as

$$MT = \frac{1}{2}(a+c)+b \tag{8.11}$$

Simple geometrical arguments show that the meantime values should be half of the cell width. A meantime can be calculated in case the muon track traversed the upper and

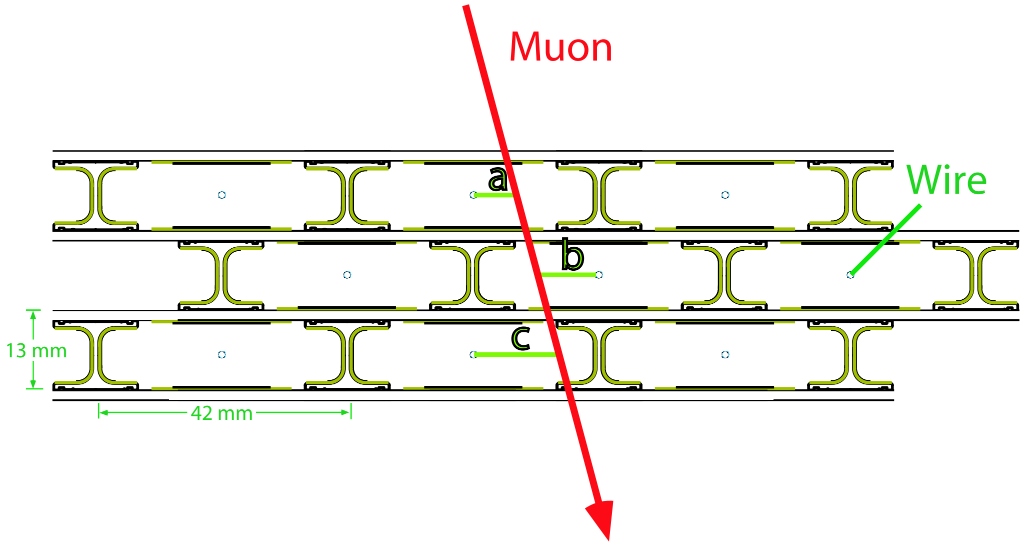

Figure 8.14: Illustration of the meantime definition: MT $= \frac{1}{2}(a + c) + b$. [10]

lower layer on the right of the anode wire and the middle layer on the left or the other way round. The first case is called *right meantime* (MT_R) and the second one *left meantime* (MT_L). In addition one can distinguish the cases where layers 1 – 3 are used ($MT_{R,1}$ and $MT_{L,1}$) or layers 2 – 4 ($MT_{R,2}$ and $MT_{L,2}$) are taken.

Figure 8.15 shows the distributions, separated as described, as measured for superlayer 10. They peak, as expected, around 21 mm.

8.5.2 Cell Resolution

Upon the widths of the distributions it is possible to calculate the resolution of the drift cells again. Since

$$\sigma^2_{\mathrm{MT}} = (\frac{1}{2}\sigma_{x,a})^2 + (\frac{1}{2}\sigma_{x,c})^2 + \sigma^2_{x,b} \tag{8.12}$$

and with the assumption of a layer independent spatial resolution

$$\sigma_x = \sigma_{x,a} = \sigma_{x,b} = \sigma_{x,c} \tag{8.13}$$

the following relation is given:

$$\sigma_x = \frac{\sigma_{\mathrm{MT}}}{\sqrt{1.5}} \tag{8.14}$$

With $\sigma_{MT} = 450$ μm for SL 10 the cell resolution is $\sigma_x = 367$ μm which exceeds the values from the track residuals without any corrections, see table 8.2, but is still satisfactory.

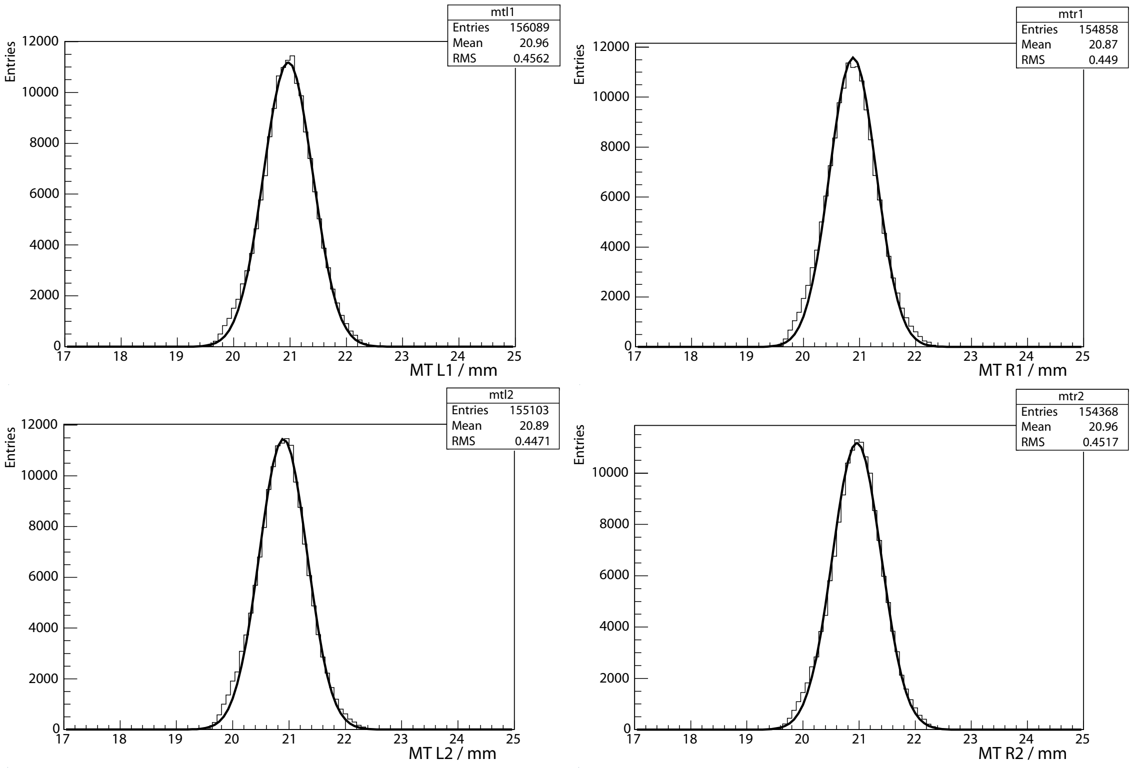

Figure 8.15: Meantime distributions of SL 10. The peaks are around 21 mm and the RMSs approximately 450 μm. Used cuts: $\chi^2/\text{dof} < 10$, $|\alpha| < 30°$.

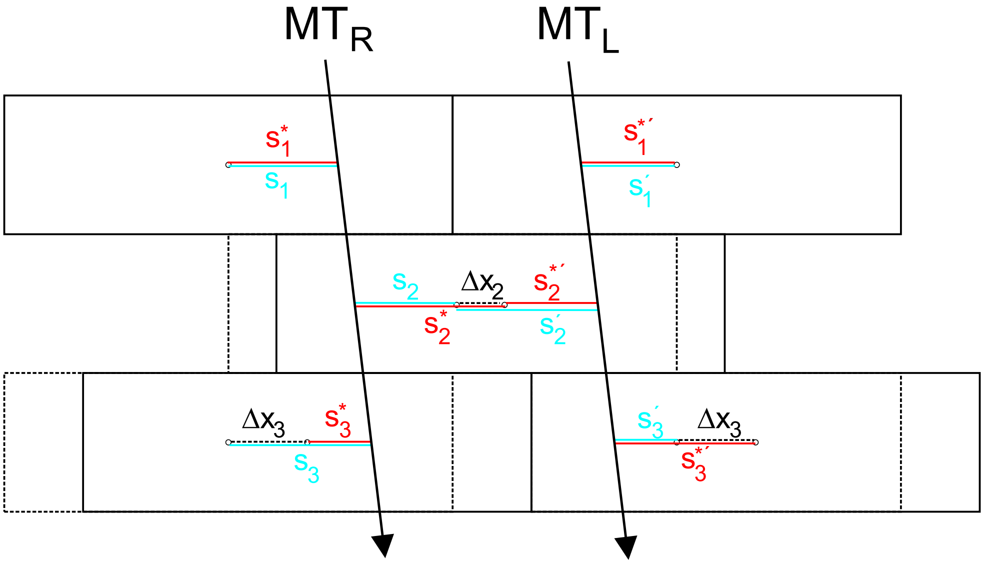

Figure 8.16: Illustration of the used variables for the meantime difference derivation.

8.5.3 Wire Positions

Since meantimes are geometrical attributes of a superlayer that depend on the positions of the wires and the aluminium beams it should be possible to recognise shifted layers through meantime distributions that do not peak at 21 mm. As this may also happen due to a wrong drift velocity or calibration the meantime differences $MT_R - MT_L$ are taken for the measurement.

In the following the top layer shall be regarded as placed at the proper position and the other two layers may have a shift of Δx_2 and Δx_3, see figure 8.16. The real drift distances s^* are given by the ideal ones s according to

$$\begin{aligned} s_1^* &= s_1 && (8.15) \\ s_2^* &= s_2 + \Delta x_2 && (8.16) \\ s_3^* &= s_3 - \Delta x_3 && (8.17) \end{aligned}$$

So the right meantimes are given by

$$MT_R = \frac{1}{2}(s_1^* + s_3^*) + s_2^* = 21 \text{ mm} + \Delta x_2 - \frac{1}{2}\Delta x_3 \tag{8.18}$$

The same goes for the left meantimes with

$$\begin{aligned} s_1^{*\prime} &= s_1' && (8.19) \\ s_2^{*\prime} &= s_2' - \Delta x_2 && (8.20) \\ s_3^{*\prime} &= s_3' + \Delta x_3 && (8.21) \end{aligned}$$

so that

$$MT_L = \frac{1}{2}(s_1^{*\prime} + s_3^{*\prime}) + s_2^{*\prime} = 21 \text{ mm} - \Delta x_2 + \frac{1}{2}\Delta x_3 \tag{8.22}$$

After that the meantime difference reads

$$\Delta MT = MT_R - MT_L = 2\Delta x_2 - \Delta x_3 \tag{8.23}$$

Thus ΔMT can be interpreted as the shift of the bottom layer in case the middle layer is in place or as twice the deviation of the layer in the middle if the bottom layer was in position.

It is possible to predict the meantime differences from the measured wire positions. Since layer 1 is the reference the shifts are given by the average deviations of the wire positions $\langle \Delta x^{\text{wire}} \rangle$:

$$\begin{aligned} \Delta x_2 &= \langle \Delta x_2^{\text{wire}} \rangle - \langle \Delta x_1^{\text{wire}} \rangle && (8.24) \\ \Delta x_3 &= \langle \Delta x_3^{\text{wire}} \rangle - \langle \Delta x_1^{\text{wire}} \rangle && (8.25) \end{aligned}$$

So finally the meantime differences expected from the wire position for three consecutive layers are

$$\Delta MT = 2\langle \Delta x_2^{\text{wire}} \rangle - \langle \Delta x_1^{\text{wire}} \rangle - \langle \Delta x_3^{\text{wire}} \rangle \tag{8.26}$$

Figure 8.17 shows the predicted differences based on the wire positions against the differences of the peak values of the measured meantime distributions. The errors of the latter ones are negligible due to the high statistics. So in general this comparison demonstrates the correlation between the wire measurement and the analysis of cosmic data. The small differences have been expected since an average shift for a complete layer and a uniform illumination with triggered muons had been assumed. A reason for the single outlier (SL 51) in the upper plot could not be found.

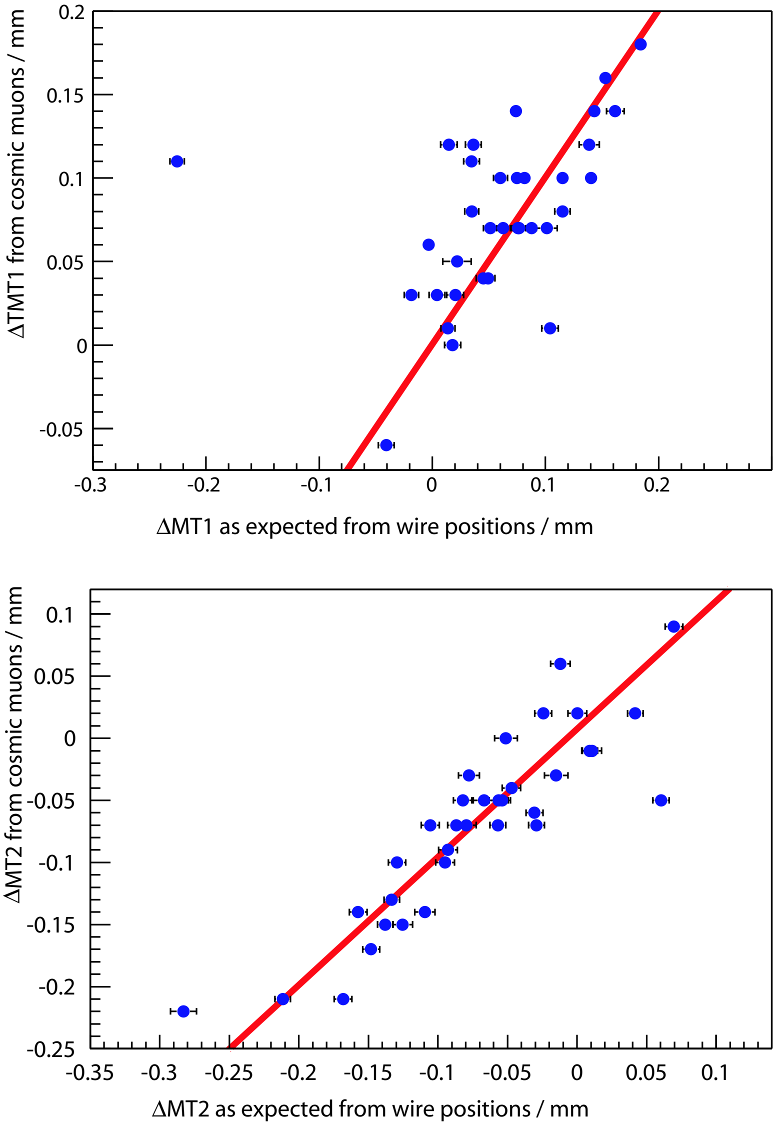

Figure 8.17: Plots of the measured meantime differences against the predictions from wire position measurements for superlayers 51 to 84 [10]. The plots contain the consecutive layers 1 – 3 (MT1) and 2 – 4 (MT2). The red line indicates where both ΔMT values are exactly the same.

Chapter 9

Examination of Cosmic Muons

For the quality control of the MB1 chambers the superlayers are tested with cosmic muons and required chamber parameters are calculated as presented in the last chapter. But it should also be possible to confirm some properties of cosmic muons even though the track finding program has not been designed for that case. Hence in this chapter multiple tracks within one event are examined to see if they fulfil the expectation from cosmic muons.

9.1 Angles Between Multiple Tracks

Since muons of the same atmospheric shower are produced in some kilometres height a pair of them which traverses a superlayer should have parallel tracks in principle. The difference in angles would be too small to be seen. So for the following examinations only events with more than one cell cluster that might contain a track are taken and out of these only the ones with at least two tracks fulfilling $\chi^2/\mathrm{dof} < 10$, $|\alpha| < 30^\circ$ are considered. Typically $4 - 6\%$ of the events survive these cuts.

Between all possible track combinations per event the angle differences are calculated whereas by convention the angle of the left track α_1 is subtracted from the angle α_2 of the right one. On average $\Delta\alpha = \alpha_2 - \alpha_1$ should give zero. But, as figure 9.1 shows, this is not true and more systematic examination proved that this is the same for all superlayers. Only the value of the peak experiences some shifts. Anyway, negative differences are always favoured. Or more descriptive: the nonparallel tracks are more likely to intersect above the superlayer than below.

This effect could not be explained with possible artefacts of the track reconstruction since no element contains the observed left-right or top-down asymmetry. To be on the safe side the track finding programm had been revised carefully without any program errors being found. So the phenomenon should be of a physical nature.

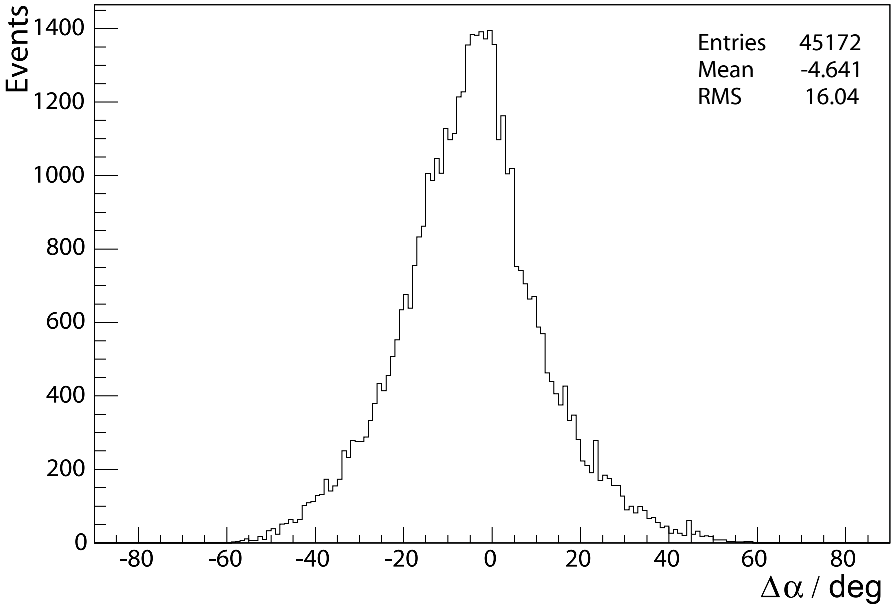

Figure 9.1: The angle differenc $\Delta\alpha$ for all possible pairs of good tracks. The peak is not at 0° as expected but shifted to negative values.

If the reason was an asymmetry effect of the test stand triggers one would expect to find a dependence on the average track inclination $\alpha = 1/2(\alpha_1 + \alpha_2)$ or the average horizontal track position $x = 1/2(x_1 + x_2)$. But figure 9.2 shows, apart from the shifted $\Delta\alpha$ peak, merely differences in the number of entries. Thus the trigger can not be the origin of the observation.

9.2 Track Vertices

The reason for the angle asymmetry could be found by reconstructing track vertices. These are the positions where pairs of calculated tracks intersect and if both detected particles base on a common physical origin, scattering neglected, the position of the original particle reaction is given by

$$h_v = \frac{x_2 - x_1}{\tan\alpha_1 - \tan\alpha_2} \tag{9.1}$$

$$x_v = x_1 + \frac{x_2 - x_1}{\tan\alpha_1 - \tan\alpha_2}\tan\alpha_1 \tag{9.2}$$

with h_v being the height above the superlayer and x_v as the horizontal position of a vertex along the superlayer.

Analysis of many events with several tracks gives a result like that in figure 9.3. The superlayer is placed at the region without any entries since the track finding algorithm requires about one cell width distance beween two track to resolve them. Some vertices

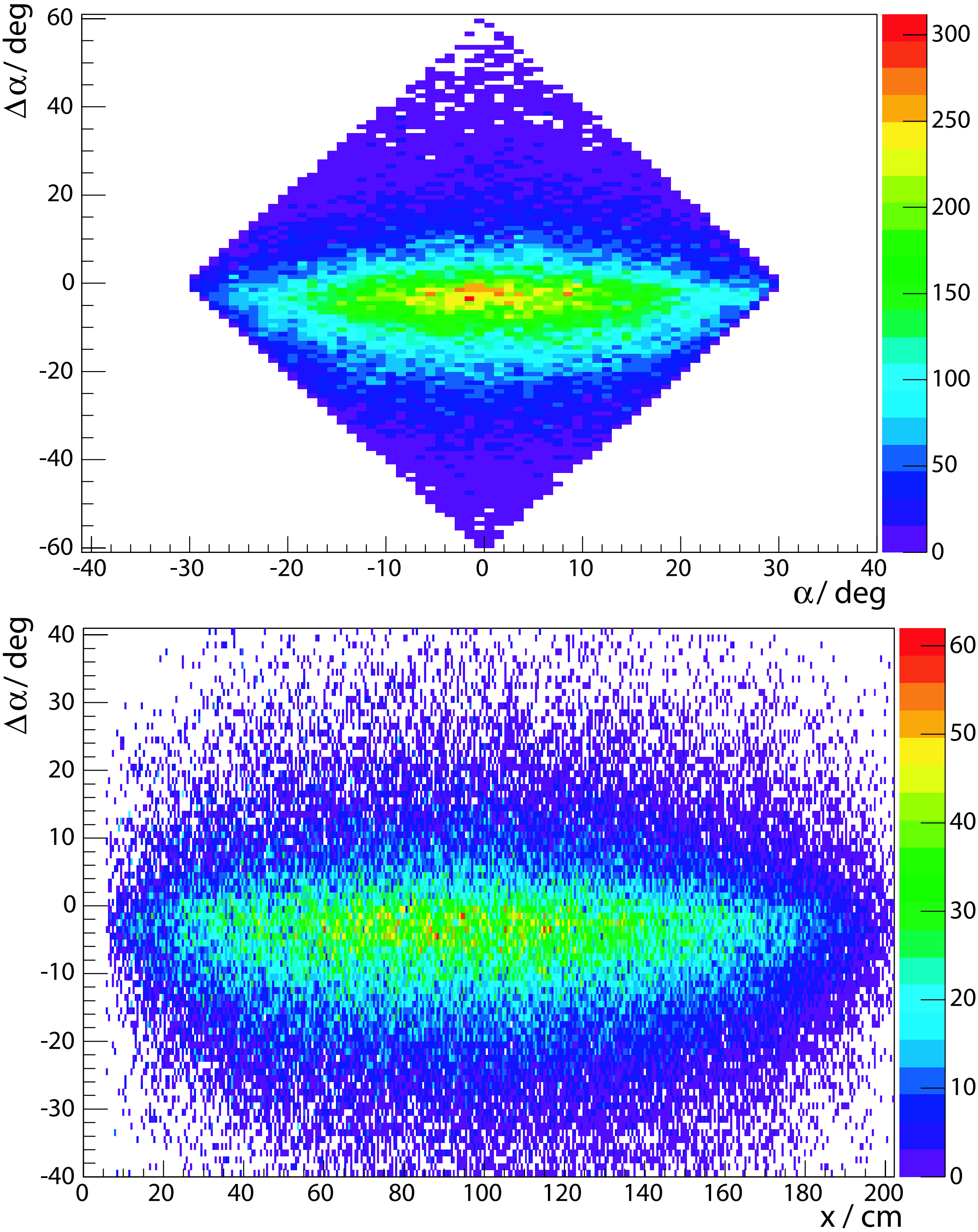

Figure 9.2: Angle differences $\Delta\alpha$ sorted by the average angle α of the double track (top) or by the average horizontal position x (bottom). Apart from the shifted $\Delta\alpha$ peak merely differences in the number of entries are visible.

occur below the superlayer since the tracks are not alway reconstructed as parallel even though they are in reality. But most track intersections are accumulated about one metre above the superlayer.

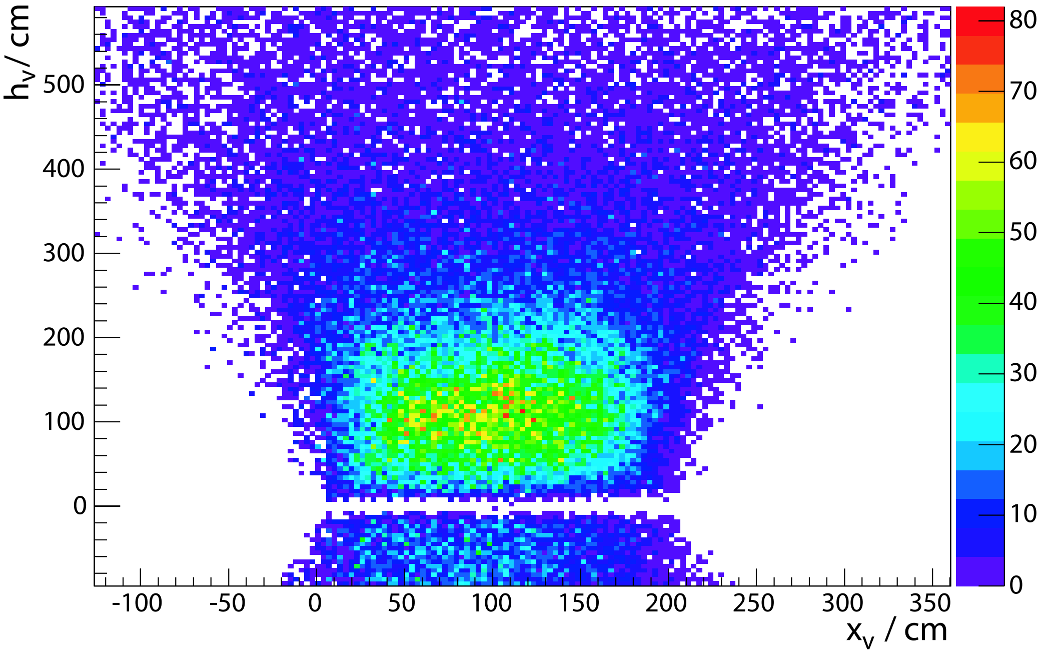

Figure 9.3: Reconstructed vertices of double tracks. The superlayer lies in the horizontal gap at a height h_v of 0 cm. The vertices are accumulated about one metre above the superlayer.

The reconstruction of the vertex heights for several superlayers yields the histograms in figure 9.4. The maxima are obviously at different positions which, as inspections have shown [41], correspond to the distance in air until the next inserted superlayer or the roof construction of the test stand.

9.3 Knock-On Electrons

After all the solution turned out that not only muons have been detected but also the tracks of so called *knock-on* or *δ electrons*. These are secondary particles produced during the particle passage, here of muons, through the massive parts of the test stand. The mechanism is that from time to time a muon may happen to hit a shell electron in such a way that this leaves the atom and passes the subsequent matter until it has lost all its kinetc energy. So the location of such a process is given by the intersection point of the muon and the electron track, see figure 9.5. This would explain the observed vertex distributions.

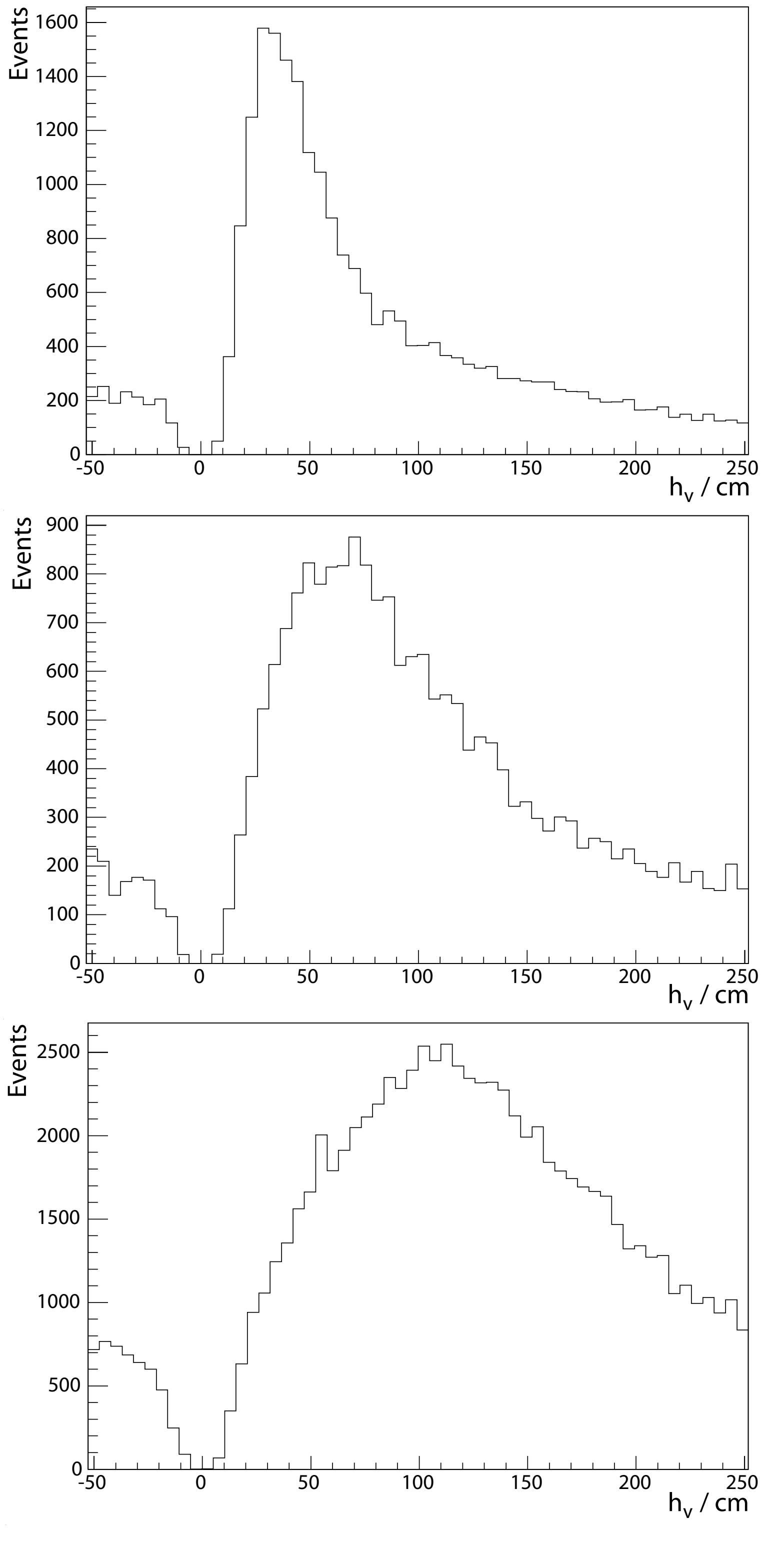

Figure 9.4: Reconstructed vertex heights for several superlayers which have been placed at different positions in the test stand.

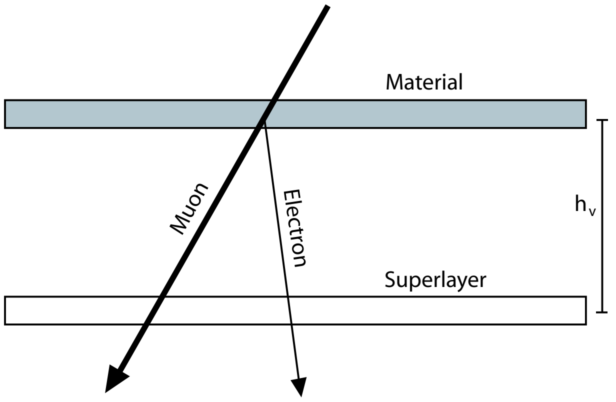

Figure 9.5: Knock-on electrons originate from material above the examined superlayer.

9.3.1 Rough Frequency Estimation

The distribution of δ electrons with kinetc energies T a lot greater than the mean excitation energy I is given by [42]

$$\frac{d^2N}{dTdx} = \frac{1}{2}Kz^2\frac{Z}{A}\frac{1}{\beta^2}\frac{F(T)}{T^2} \qquad \text{for} \qquad I \ll T \leq T_{\max} \tag{9.3}$$

with

K : $4\pi N_A r_e^2 m_e c^2 = 0.307$ MeV cm^2 mol^{-1}
N_A : Avogadro's number
ze : charge of incident particle
Z : atomic number of absorber
A : atomic mass of absorber in g mol^{-1}

and the other variables having their usual meanings. The function $F(T)$ for spin 1/2 particles can be found in [42] but it is about unity for $T \ll T_{\max}$ whereas

$$T_{\max} = 2m_e c^2 \beta^2 \gamma^2 \qquad \text{for} \qquad 2\gamma m_e/M \ll 1 \tag{9.4}$$

with M as the mass of the incident particle. So for cosmic muons with about 4 GeV energy it is possible to approximate $\beta \approx 1$ and, since

$$\beta\gamma = \frac{p}{Mc} \approx \frac{4 \text{ Gev}}{106 \text{ MeV}} \tag{9.5}$$

the maximum kinetic energy $T_{\max}$ of the knock-on electrons according to equation (9.4) is

$$T_{\max} \approx 1450 \text{ MeV} \tag{9.6}$$

In the following it is simplified that for the absorber materials within the test stand, i.e. mainly iron and aluminium, it can be assumed

$$\frac{Z}{A} \approx \frac{1}{2} \text{ g}^{-1} \text{ mol} \tag{9.7}$$

So equation (9.3) yields

$$\frac{d^2N}{dTdx} \approx \frac{1}{4} \cdot 0.3 \text{ MeV cm}^2 \text{ g}^{-1} \frac{1}{T^2} \tag{9.8}$$

For a good reconstructed track an electron must have traversed four aluminium plates of 1.5 mm. Since in linear approximation electrons lose about 0.5 MeV/mm in aluminium the minimum energy of a detectable electron is around 3 MeV. Thus

$$\frac{dN}{dx} = \frac{0.3}{4} \text{ MeV cm}^2 \text{ g}^{-1} \int_{3 \text{ MeV}}^{1450 \text{ MeV}} \frac{dT}{T^2} \approx 0.025 \text{ cm}^2 \text{ g}^{-1} \tag{9.9}$$

So with the assumption that δ electrons are not absorbed within the material they are produced one needs about 0.2 cm of iron with a density $\rho = 7.9 \text{ g cm}^{-3}$ to produce a noticeable electron with a probability of 4% which is about the observed ratio[1]. In case the electrons are knocked out of higher superlayers which consist mainly of aluminium plates they should produced within the last two or three of them.

Only massive structures next to the superlayer are visible as electrons from material behind are absorbed again before they can reach the examined superlayer.

9.3.2 Efficiency of the Bottom Layer

Calculation of the cell efficiency just for events with at least two particle tracks that survived the χ^2 cut shows, see figure 9.6, that cells of the bottom layer are more likely to be inefficient. This can be understood since from time to time the energy of the δ electron only suffices to traverse three aluminium plates and drift cells. The last layer is not reached but the number of hits allows a track reconstruction and so the expected cell in the bottom layer is regarded as inefficient. Of course a knock-on electron may become stuck at a higher position but in this case only one or two cells are hit and hence their responses regarded as noise.

9.4 Distances Between Cosmic Muons

The last outstanding parameter to be measured for events with multiple tracks is the distance Δx between pairs of them at the middle of the superlayer height. Since only cosmic muons are of interest the unwanted δ electrons are tried to be excluded, as their track vertices are located above the superlayer, by demanding $h_v < 0$. The result of such an approach is shown in figure 9.7. The edge for small distances is expected from the limited double track resolution. But the overall shape of the distribution can not be understood with the assumption of a flat muon distribution as one might expect since a superlayer only covers a tiny area compared to the total extension of an air shower. Hence an explanation would require elaborate monte carlo techniques simulating cosmic showers together with the superlayer and test stand geometries.

---

[1] The worst case with all double tracks due to electrons assumed.

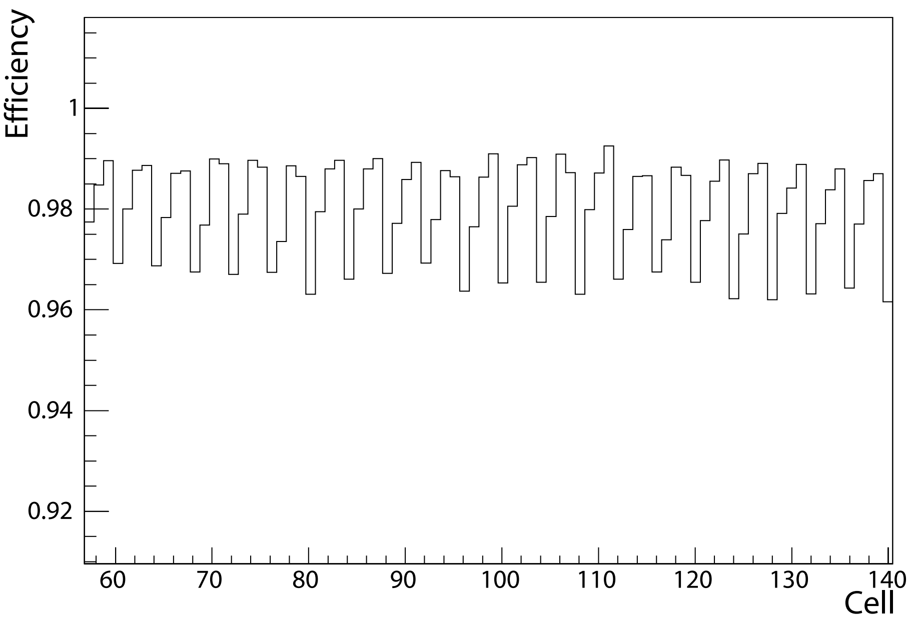

Figure 9.6: Efficiency cell by cell for multiple tracks only. Cells with a number divisible by four are placed in the bottom layer and more frequently considered as inefficient since not all δ electrons traverse the complete superlayer.

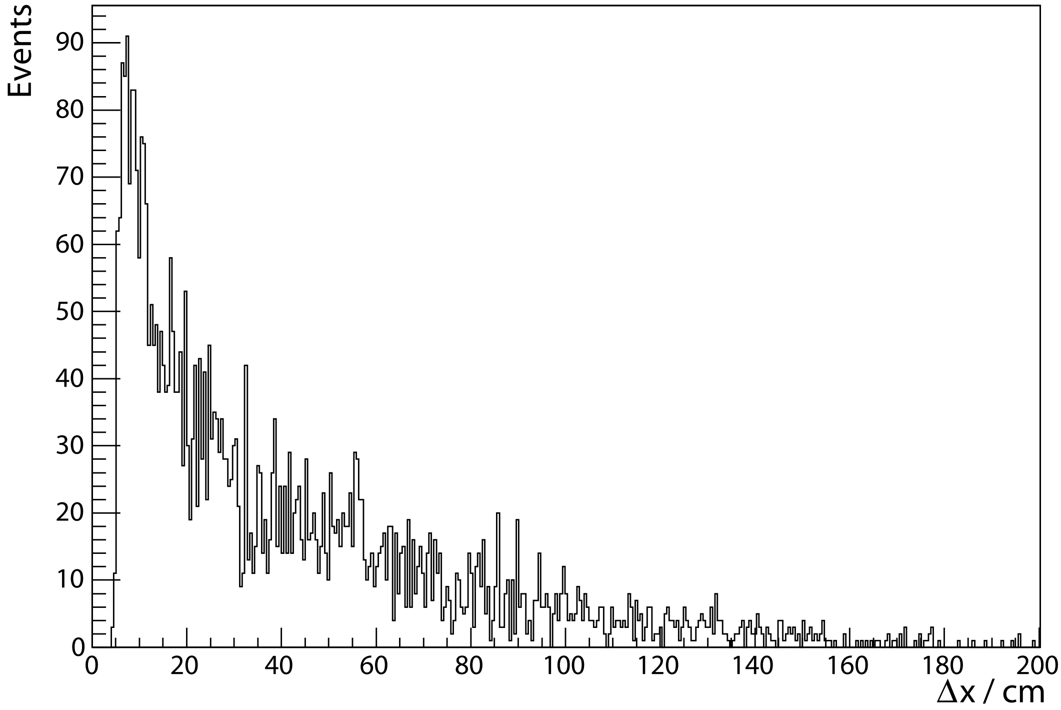

Figure 9.7: Measured distances between pairs of cosmic muons for a ϕ superlayer (SL 37).

Chapter 10

Summary and Outlook

The future CMS detector at the LHC accelerator will contain muon drift chambers of which about 70, the MB1 chambers, are produced at the III. Phys. Inst. A of Aachen University. These chambers are located mainly in the inner layer of the barrel part of the muon system. MB1 chambers consist of three similar superlayers whose examination in a test stand had been one issue of this diploma thesis. The aim was to create a software able to analyse event files from the DAQ at Aachen according to the requirements of the quality control of the CMS muon group.

In a first step it had been necessary to write a software to reconstruct particle tracks from the recorded drift times. Only tracks with a satisfactory quality are chosen for further analysis. To increase the number of usable events, hits probably caused by noise or afterpulses are sorted out. Multiple particle tracks within the same event are distinguished automatically as long as they are not located too close to each other.

Several approaches to increase the track quality have been applied. In particular the compensation of T_0 shifts of individual drift cells yields the strongest improvements. But also correcting the slight non-linearity of the r-t relation with a calibration and the usage of optical wire position measurements enhance the track quality.

After the preparatory software development required superlayer and drift cell data such as noise, efficiency, resolution and meantimes could be computed. Efficiencies inside the gas volume are typically 99.8% and later at CMS a cell resolution of $\sigma \leq 250\mu\text{m}$ is achievable. A correlation of the reconstructed tracks with the wire position measurements via the meantimes could be observed giving confidence to both independent methods.

The performed analyses of cosmic muons, with the superlayers not as objects to be examined but as tools, turned out that a major contribution to events with multiple hits originates from electrons, knocked out from material within the test stand. A trial to suppress these candidates yielded a distribution of projected distances between pairs of cosmic muons in MB1 superlayers.

So altogether a reliable tool for present and future superlayer analyses could be produced in the course of this work. Slight adjustments make the use on CERN testbeam data already possible now. A future extension of the track finding program for complete muon chambers with all three superlayers should be no problem. In principle mainly the assignment of track segments in case of events with more than one particle would have to be worked on.

Analyses documenting the overall performance of the MB1 chambers are ongoing at the Aachen CMS muon group. Still untested is the use of the T_0s according to test pulse measurements instead of using the edges of the TDC spectra. The effects of including the optically measured wire positions could be corroborated by testing more superlayers with and without these corrections.

Appendix A

C++ Implementation of the Track Reconstruction Software

This appendix contains the header files of the MUONTRACKER software that has been created for this thesis. Also the code of the most fundamental methods and algorithms is given.

A.1 Header Files

A.1.1 constants.h

Contains the constants that define the program behaviour. In the following the defaults are given and the function described in short.

`VERSION = 1.00`
Program version. All examinations in this thesis have been done with version 1.00.

`USE_TZERO = kTRUE`
By default the detected T_0 deviations are corrected. Setting this switch to `kFALSE` takes the global value for all cells.

`FASTMODE = kTRUE`
In the fast mode no layers are excluded during efficiency calculations. For the other possibility `kFALSE` has to be used at this point.

`AVOID_AMBIGUITIES = kTRUE`
If the fast mode it not used it is useful to exclude the possibilites for 3 layer fits that lead to ambiguities. If this constant is set to `kFALSE` these cases are taken anyway.

`TAKE_SINGLE_TRACKS = kTRUE`
The default uses events with an arbitrary number of track candidates. The default should be changed to `kFALSE` if only events with multiple tracks are examined. This increases the processing speed as events with single tracks are not fitted.

`LASTCELL = 228`
The largest occuring cell number. The default of 228 suffices for Φ and Θ superlayers.

`FIRSTCELL = 2`
The number of the first cell to be examined.

`HALFWIDTH_EFF_MIN = 25`
`HALFWIDTH_EFF_MAX = 20750`
Minimum and maximum effective drift distances. At the height of the wire some tracks may lie a little inside the I-beam. A change here influences the calibration.

`TDC_UPPER_EDGE = 10500`
`TDC_LOWER_EDGE = 9300`
Region of the TDC window containing the drift time spectrum.

`FIT_QUALITY_EXPONENT = 0.82`
Damping factor used at the fitting algorithm.

`TZERO_CUT = 10`
Maximum allowed T_0 uncertaincy for the individual cells. If exceeded the global value is taken.

`CHI2CUT = 10`
`ALPHACUT = 30`
The cuts a track has to survive to be considered as good.

`MAX_CAL_EVENTS = 50000`
The maximum number of events to use for calibration. Less are only taken in case of not enough events in file.

`MAX_EVENTS = 1000000`
The number of events to fit. Less are taken in case the number of recorded events is smaller.

Other values, such as the drift velocity and the defaults for T_0 and T_{max}, are command line parameters of the MUONTRACKER software.

A.1.2 raw_event.h

Contains a structure to hold drift time data for one event from the `.root` files

```
struct raw_event {
   Int_t event_number;
   Int_t hits_in_event;
   Int_t hits_in_cell[MAX_CELLS];
   Int_t cell_number[4097];
   Int_t tdc_datum[4097];
};
```

A.1.3 event_class.h

Contains the class that divides a complete event into several `SubEvent` clusters which are likely to correspond to a muon track. In case cells of these subevents contain multiple hits there is a number of permutations which must be considered in the following. Each permutation is a `SubEventCandidate`. Noise hits are also sorted out.

```
struct subevent_container {
   raw_event subevent;
   subevent_container *and_pointer;
   subevent_container *or_pointer;
};


class event_class {

   private:
      subevent_container *start_pointer;
      subevent_container *subevent_pointer;
      subevent_container *subevent_candidate_pointer;
      raw_event          event;
      Int_t              number_of_sub_events;

      void               Delete(subevent_container* delete_pointer);
      void               Print(subevent_container* print_pointer,int subevent,
                               int candidate);
      raw_event          RemoveOtherCellHits(raw_event e, int hit_to_remain);
      raw_event          SplitEvent(raw_event e, int firstcell, int lastcell);

   public:
      event_class();
      ~event_class();
      void               AddSubEvent(raw_event e);
      void               AddSubEventCandidate(raw_event e);
```

```
      void              ChangeToNextSubEvent();
      void              Delete();
      raw_event         GetSubEventCandidate();
      void              NewSubEvent();
      void              Print();
      void              Reset();
      void              SetEvent(raw_event e);
      Int_t             SubEventCounter();
};
```

A.1.4 root_file.h

Contains a class that provides an interface to read data from a `.root` file containing DAQ event data.

```
class root_file {

   private:
      TFile     *file_pointer;
      TTree     *tree_pointer;
      raw_event event;
      Int_t     number_of_entries;
      Bool_t    inverted;

   public:
      root_file();
      ~root_file();

      void      CloseFile();
      raw_event GetEntry(Int_t number, Bool_t sort = kTRUE);
      Int_t     GetNumberOfEntries();
      void      InvertDriftTimes();
      Bool_t    IsOpen();
      void      OpenFile(char name[]);
};
```

A.1.5 track_class.h

Contains the class that fits the track upon data in a `raw_event` structure. Drift velocities, wire positions, etc. can be set and after a fit is performed via the `CalculateFit` method the track and quality parameters can be read.

```
class track_class {
```

```
private:
   raw_event event;
   TRandom   *random;
   Int_t     calibration_offset;
   Int_t     cell_zero_time[MAX_CELLS + 1];
   Int_t     cell_max_time[MAX_CELLS + 1];
   Double_t  cell_drift_velocity[MAX_CELLS + 1];
   Float_t   drift_distance_calibration[CAL_LAST - CAL_FIRST + 1][MAX_CELLS + 1];
   Float_t   tdc_timestep;
   Int_t     cell_width;
   Int_t     cell_height;
   Int_t     x_offset;
   Int_t     y_offset;
   Int_t     wire_x_position[MAX_CELLS + 1];
   Int_t     wire_y_position[MAX_CELLS + 1];
   Int_t     first_wire;
   Int_t     last_wire;
   Int_t     drift_distance[4097];
   Int_t     horizontal_distance[4097];
   Int_t     hit_quality[4097];
   Int_t     good_hits_in_event;
   Int_t     meantime_l1, meantime_l2, meantime_r1, meantime_r2;
   Double_t  fit_alpha;
   Int_t     fit_x;
   Double_t  fit_chi2;
   Bool_t    drift_distance_table_is_calculated;
   Bool_t    fit_is_calculated;
   Bool_t    in_calibrated_mode;
   Bool_t    layer_hit[4];

   void      CalculateWirePositionTable();
   void      CalculateDriftDistanceTable();
   void      CalculateQualityTable();
   void      ResetFlags();

public:
   track_class(Int_t width_of_cell, Int_t height_of_cell,Int_t offset_x = 0,
               Int_t offset_y = 0, Int_t first_wire_number = 0,
               Int_t last_wire_number = MAX_CELLS);
   ~track_class();

   Int_t     CalculateDriftDistance(Int_t hitnumber);
   void      CalculateFit(Int_t x_step, Double_t alpha_step, Double_t factor,
                          Int_t excluded_layer = 0);
   Bool_t    CellBlind(Int_t cell);
   Double_t  ChiSquare(Int_t track_x,Int_t track_y,Double_t alpha,
                       Int_t excluded_layer = 0);
   Double_t  GetAlpha();
   Int_t     GetAverageXPosition();
   Int_t     GetCellHeight();
   Int_t     GetCellNumber(Int_t hitnumber);
   Int_t     GetCellWidth();
```

```
      Double_t  GetChi2();
      Int_t     GetFirstWire();
      Int_t     GetGoodHitCell(Int_t hit);
      Int_t     GetGoodHitDriftDistance(Int_t hit);
      Int_t     GetGoodHitsInEvent();
      Int_t     GetGoodHitTDC(Int_t hit);
      Int_t     GetHitsInCell(Int_t cell);
      Int_t     GetHitLayers();
      Int_t     GetHitsInEvent();
      Int_t     GetLastWire();
      Int_t     GetMeanTimeL1();
      Int_t     GetMeanTimeL2();
      Int_t     GetMeanTimeR1();
      Int_t     GetMeanTimeR2();
      Int_t     GetResidual(Int_t hitnumber);
      Int_t     GetTrackHorizontalDistance(Int_t cell);
      Int_t     GetWireXPosition(Int_t wire);
      Int_t     GetWireYPosition(Int_t wire);
      Int_t     GetX();
      Int_t     GetXOffset();
      Int_t     GetYOffset();
      Bool_t    LayerHit(Int_t layer);
      void      Print();
      void      PrintAll();
      void      PrintFit();
      void      PrintMeanTimes();
      void      PrintResiduals();
      void      PrintWirePositionTable();
      void      SetCellHeight(Int_t height);
      void      SetCellSize(Int_t width, Int_t height);
      void      SetCellWidth(Int_t width);
      void      SetDriftVelocity(Int_t velocity);
      void      SetDriftVelocity(Int_t velocity, Int_t cell);
      void      SetDriftVelocity(char filename[]);
      void      SetDriftVelocity(char filename[], Int_t cell, Int_t offset = 0);
      void      SetEvent(raw_event event_data);
      void      SetFirstWire(Int_t wire);
      void      SetLastWire(Int_t wire);
      void      SetOffset(Int_t x, Int_t y);
      void      SetTDCTimeStep(Float_t timestep);
      void      SetTimeMaximum(Int_t time);
      void      SetTimeMaximum(Int_t time, Int_t cell);
      void      SetWireXPosition(Int_t wire, Int_t position);
      void      SetWireYPosition(Int_t wire, Int_t position);
      void      SetXOffset(Int_t offset);
      void      SetYOffset(Int_t offset);
      void      SetZeroTime(Int_t time);
      void      SetZeroTime(Int_t time, Int_t cell);
      Double_t  TrackCircleDistance(Int_t track_x,Int_t track_y,Double_t alpha,
                                    Int_t circle_x,Int_t circle_y,Int_t radius);
};
```

A.2 Fundamental Algorithms

In the following the implementations of the fundamental MUONTRACKER algorithms are given

A.2.1 Fit Calculation

The implementation of the fitting algorithm as described in this thesis. Parameters are the initial x and α steps, the damping factor and a layer that shall be excluded for the track finding. In case all layers shall be taken the last argument has to be set to 0.

```
void  track_class::CalculateFit(Int_t x_step, Double_t alpha_step,
                        Double_t factor, Int_t excluded_layer) {

   Int_t x;
   Int_t min_x;
   Double_t alpha;
   Double_t min_alpha;
   Double_t sign_x;
   Double_t sign_alpha;
   Double_t chi2;
   Double_t temp_chi2;

   if(drift_distance_table_is_calculated == kFALSE)
      CalculateDriftDistanceTable();
   x = GetAverageXPosition();
   alpha = M_PI / 2;

   if (good_hits_in_event > 2) {
      min_x = x;
      min_alpha = alpha;
      chi2 = ChiSquare(x, 0, alpha, excluded_layer);
      while (x_step > 1) {
         for (int a = 0; a < 3; a++)
            for (int b = 0; b < 3; b++) {
               sign_x = (a - 1) * random->Rndm();
               sign_alpha = (b - 1) * random->Rndm();
               temp_chi2 = ChiSquare((int)(x + sign_x * x_step), 0,
                  alpha + sign_alpha *alpha_step, excluded_layer);
               if (chi2 > temp_chi2) {
                   chi2 = temp_chi2;
                   min_x = (int)(x + sign_x * x_step);
                   min_alpha = alpha + sign_alpha * alpha_step;
               }
            }
         x = min_x;
         alpha = min_alpha;
         x_step = (Int_t)(x_step * factor);
```

```
         alpha_step = alpha_step * factor;
      }

      fit_alpha = alpha;
      fit_x = x;
      fit_chi2 = chi2;
      fit_is_calculated = true;
   }
   else {
      fit_alpha = 0;
      fit_x = 0;
      fit_chi2 = 999999999;
   }
}
```

A.2.2 Subevent Division

This class divides the original event data (the hits within the `raw_event` structure must already be sorted starting with the smalles cell number) into subevents. Clusters with less than three cells are thrown away.

```
void event_class::SetEvent(raw_event e) {

   Int_t min_cell = MAX_CELLS;
   Int_t max_cell = 1;
   Int_t start;
   Int_t hitcells =0;
   Int_t spaces = 0;
   Int_t permutations;

   event = e;
   for (int i = 0; i < MAX_CELLS + 1; i++)
      if (e.hits_in_cell[i] > 0) {
         if (i < min_cell)
            min_cell = i;
         if (i > max_cell)
            max_cell = i;
      }
   start = min_cell;
   for (int i = min_cell; i <= max_cell; i++) {
      if (e.hits_in_cell[i] == 0) {
         spaces++;
      }
      else {
         hitcells++;
         spaces = 0;
      }
      if (spaces == 2 && hitcells > 2) {
         permutations = 1;
```

```
         for (int j = start; j <= i; j++)
            if (e.hits_in_cell[j] > 1)
               permutations *= e.hits_in_cell[j];
         if (permutations <= 64 && permutations > 0) {
            NewSubEvent();
            AddSubEvent(SplitEvent(e,start,i));
         }
         start = i + 1;
         spaces = 0;
         hitcells = 0;
      }
      if (spaces == 6 && hitcells <= 2) {
         start = i + 1;
         spaces = 0;
         hitcells = 0;
      }
   }
   if (start < MAX_CELLS + 1 && hitcells > 2) {
      permutations = 1;
      for (int j = start; j <= max_cell; j++)
         if (e.hits_in_cell[j] > 1)
           permutations *= e.hits_in_cell[j];
      if (permutations <= 64 && permutations > 0) {
         NewSubEvent();
         AddSubEvent(SplitEvent(e,start,max_cell));
      }
   }
}
```

A.2.3 The Main Loop

This is a simplified version of the main MUONTRACKER loop that only prints out the reconstruction results instead of filling them into histograms. The use of the classes from above is illustrated that way.

```
#include <iostream.h>
#include "track_class.h"
#include "root_file.h"
#include "event_class.h"

int main(int argc, char **argv) {
   event_class complete_event;
   raw_event event;
   root_file file;

   Double_t temp_chi2;
   raw_event temp_event;

   track.SetZeroTime(10260);
```

```
   track.SetTimeMaximum(9870);
   track.SetTDCTimeStep(1);
   track.SetDriftVelocity(55);

   file.OpenFile("sl_xxx.root");

   for (int i = 0; i < file.GetNumberOfEntries(); i++) {
      complete_event.Delete();
      event = file.GetEntry(i);
      complete_event.SetEvent(event);
      complete_event.Reset();
      event = complete_event.GetSubEventCandidate();
      track.SetEvent(event);
      while (event.hits_in_event > 0) {
         track.CalculateFit(40000, M_PI / 2, 0.85);
         temp_chi2 = track.GetChi2();
         temp_event = event;
         event = complete_event.GetSubEventCandidate();
         if (event.hits_in_event > 0) {
            while (event.hits_in_event > 0) {
               track.SetEvent(event);
               track.CalculateFit(40000, M_PI / 2, 0.85);
               if (track.GetChi2() < temp_chi2) {
                  temp_chi2 = track.GetChi2();
                  temp_event = event;
               }
               event = complete_event.GetSubEventCandidate();
            }
            track.SetEvent(temp_event);
            track.CalculateFit(40000, M_PI / 2, 0.85);
         }

         track.PrintAll();
         if (track.GetChi2() < 10)
            cout << "Good track!";

         complete_event.ChangeToNextSubEvent();
         event = complete_event.GetSubEventCandidate();
         track.SetEvent(event);
      }
   }

   return 0;
}
```

Bibliography

[1] D. Griffiths, Einführung in die Elementarteilchenphysik, Akademie Verlag (1996)

[2] Ch. Berger, Elementarteilchenphysik, Springer-Verlag (2001)

[3] P. Schmüser, Feynman-Graphen und Eichtheorien für Experimentalphysiker, Springer-Verlag (1995)

[4] H.V. Klapdor-Kleingrothaus, K. Zuber, Teilchenastrophysik, Teubner Studienbücher (1997)

[5] Teilchen, Felder und Symmetrien, miscellaneous authors, Spektrum der Wissenschaft (1988)

[6] J. Schnakenberg, Elektrodynamik (2000), `http://bibsrv.physik.rwth-aachen.de/Skripte/Index.html`

[7] S. Kasselmann, Die Higgs-Suche, seminar lecture, RWTH Aachen, `http://accms04.physik.rwth-aachen.de/Vorlesungen/2001-SS/16/`

[8] The LEP Collaborations, A Combination of Preliminary Electroweak Measurements and Constraints on the Standard Model, CERN-EP Note in preperation

[9] E. Accomando et al., Physics Reports 299, 1-78 (1998)

[10] S. Hermann, Präzisionsmessungen an Myondriftkammern für den CMS-Detektor und die Bedeutung des Myonsystems für die Higgs-Suche am LHC, dissertation, III. Phys, Inst., RWTH Aachen (2004)

[11] `http://pcbunn.cithep.caltech.edu/projdesc/CACR_GIOD.html`

[12] `http://cmsinfo.cern.ch/` (modified)

[13] H.E. Haber, G.L. Kane, The Search for Supersymmetry, Phys. Rep. 117, 75 ff. (1985)

[14] K. Hagiwara et al., Phys. Rev. D 66, 010001 (2002) `http://pdg.lbl.gov/pdg.html`

[15] CERN Document Server, `http://cdsweb.cern.ch/` (possibly modified)

[16] Fermi National Accelerator Laboratory `http://www.fnal.gov/`

[17] CMS, The Compact Muon Solenoid, Technical Proposal, CERB/LHCC 94-38 (1994)

[18] CMS, The Muon Project, Technical Design Report, CERN/LHCC 97-32 (1997)

[19] G. Otter, R. Honecker, Atome - Moleküle - Kerne, Band II: Molekül- und Kernphysik, B.G. Teubner (1996)

[20] G. Charpak et al., Nucl. Instr. and Meth. 227 (1984) 277

[21] O.C. Allkofer, Introduction to Cosmic Radiation, Verlag Karl Thiemig (1975)

[22] M.M. Shapiro, R. Silberberg, Ann. Rev. Nucl. Sci. 20 (1970) 323, modified

[23] K. Greisen, Ann. Rev. Nucl. Sci 10, (1960) 63

[24] Ch. Autermann, Funktionstests von CMS-Myon-Kammern, diploma thesis, III. Phys. Inst., RWTH Aachen (2002)

[25] H. Reithler, M. Wegner, private communication

[26] M. Bontenackels, Aufbau einer Messanordnung für Myonkammern, diploma thesis, III. Phys. Inst., RWTH Aachen (2001)

[27] M. Sowa, Aufbau, Kalibration und Anwendung einer Messapparatur zur Überwachung des Gasdrucks in CMS-Myonkammern, diploma thesis, III. Phys. Inst., RWTH Aachen (2003)

[28] M. Wegner, Studien zum Verhalten von Myonkammern unter hohen Untergrundraten, dissertation, PITHA 00/04, III. Phys. Inst., RWTH Aachen (2000)

[29] Drift Tubes Quality Control Manual and Procedures
`http://www.to.infn.it/activities/experiments/cms/QUALITY/QCManual.html`

[30] M. Bontenackels, private communication

[31] LeCroy Research Systems Corp., CAMAC TDC 2277, Technical Information Manual (1993)

[32] M. Bontenackels, Benutzeranleitung, CMS Myonkammern, Superlayertests mit kosmischen Myonen (2002),
`http://www.physik.rwth-aachen.de/~hoepfner/cms_muon.html`

[33] Root Users Guide v3.10, An Object-Oriented Data Analysis Framework, CERN Program Library (2004)

[34] T. Hebbeker, SCAN.C, usable with the ROOT C++ interpreter
`http://www.physik.rwth-aachen.de/~hebbeker/muontest/`

[35] T. Hebbeker, Statistische Methoden der Datenanalyse, HU Berlin (WS 97/98)
`http://www-eep.physik.hu-berlin.de/~hebbeker/lectures/index.htm`

[36] W. Oberschelp et al., Informatik für Naturwissenschaftler (Algorithmen), Lehrstuhl für angewandte Mathematik insb. Informatik, RWTH Aachen (WS 98/99)

[37] M. Cerrada et al., Test Beam Analysis of the First CMS MB2 Drift Tube Muon Chamber, CMS Note 2003/007

[38] J. H. Friedman, Data Analysis Techniques for High Energy Particle Physics. In CERN, editor, Proceedings of the 1974 CERN School of Computing, Godoysund (Norway), 1974. CERN Report 74-23

[39] T. Hebbeker, Scan.C & Preliminary Results Cosmic Tests Superlayer 15 (2002) `http://www.physik.rwth-aachen.de/~hebbeker/muontest/`

[40] T. Stapelberg, private communication

[41] O. Tsigenov, private communication

[42] B. Rossi, High Energy Particles, Prentice-Hall, Inc., Englewood Cliffs, NJ (1952)

List of Figures

List of Tables

Acknowledgement

First of all my thanks go to Mr. Prof. Dr. T. Hebbeker for offering me the analysis of MB 1 muon chambers as a topic for my diploma thesis. Furthermore I am glad I could win Mr. Prof. Dr. A. Böhm to concern himself with this project as co-evaluator.

In many cases I could benefit from the experience in drift tube chambers of Mr. Prof. Dr. T. Hebbeker, Ms. Dr. K. Hoepfner and Mr. Dr. H. Reithler, who disclosed many aspects I initially did not take into account. Most technical help, concerning the data aquisition and the data base, I received from the doctoral candidate Michael Bontenackels, especially during the beginning of my work. He is also the one who contributed the test pulse measurements. In addition I have to thank Dr. Martin Wegner for his hints regarding the calibration method and Oleg Tsigenov for realising some special requests during data taking. I also want to mention Dr. Sven Hermann who accomplished the wire position measurements.

I did not only experience professional but also private support from my colleagues. At this point I want to add Michael Sowa and Pim Rütten to my list of helpful persons and mention Michael Bontenackels and Oleg Tsigenov again. During a drive to CERN because of a CMS week I also became acquainted with Sven Hermann. And to Lotte Wilke, Michael Bontenackels and all the others I want to apologise again for not taking part in the Lousberg run.

Last, but not least, I want to express the gratitude for my parents' support in all respects during my studies and thank my girlfriend just for being there.